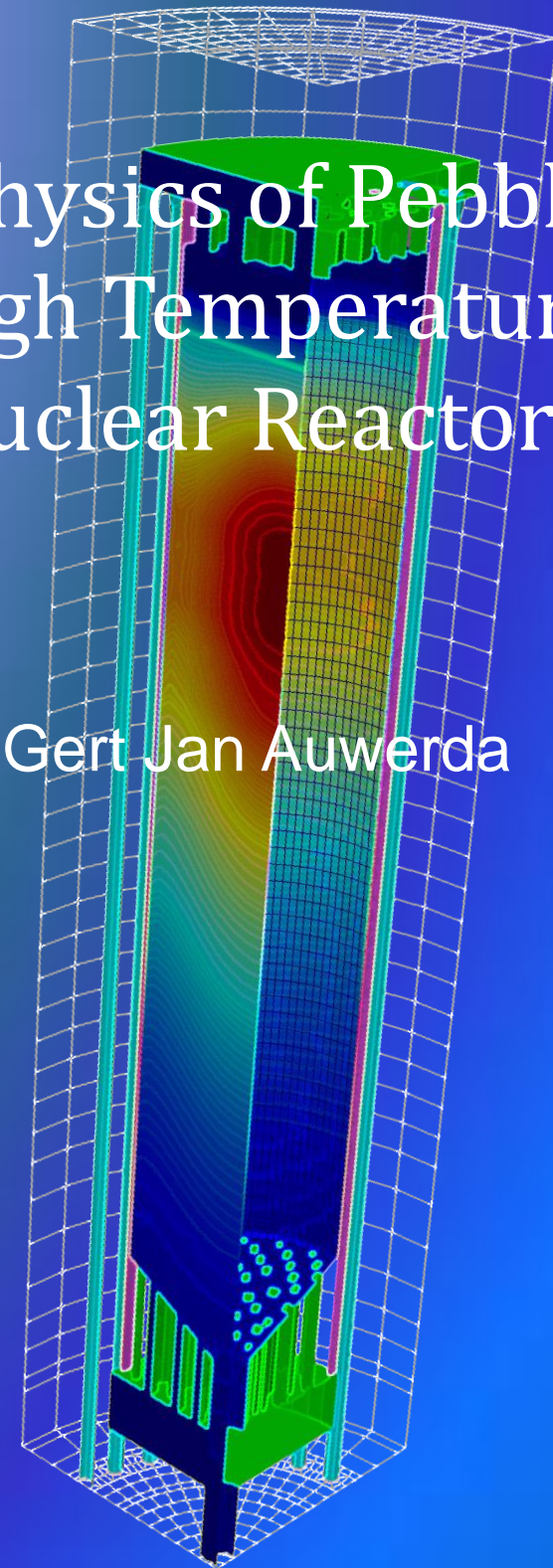


Core Physics of Pebble Bed High Temperature Nuclear Reactors

Gert Jan Auwerda



Core Physics of High Temperature Pebble Bed Nuclear Reactors

Gert Jan Auwerda

Propositions

accompanying the dissertation

CORE PHYSICS OF PEBBLE BED HIGH TEMPERATURE NUCLEAR REACTORS

by **Gert Jan AUWERDA**

1. Non-isotropic models are required to accurately simulate heat and mass transfer next to the wall in a pebble bed reactor. *(This thesis.)*
2. In a pebble bed reactor, the higher porosity near the boundaries than in the centre of the randomly stacked pebble bed can be ignored when calculating the neutron flux distribution, but cannot be ignored when calculating the k_{eff} or the power distribution. *(This thesis.)*
3. In annular pebble bed designs, the wall-channelling effect results in a significantly lower maximum fuel temperature during both normal operation and during a pressurized loss of forced cooling accident. *(This thesis.)*
4. A grid convergence study based on Richardson extrapolation to evaluate the grid convergence index (GCI) should be mandatory to evaluate the mesh quality when solving equations using numerical analysis. *(P.J. Roache. Verification and validation in computational science and engineering, Hermosa Publishers, USA, 1998.)*
5. The use of adjoint calculations with deterministic codes to generate weight windows for Monte Carlo neutron transport calculations increases both the fidelity in and speed of these calculations in comparison to the use of iterative weight-window generation with the Monte Carlo transport code. *(G.J. Auwerda. Assessment of weight windows generated from adjoint flux calculations, K5042/08.92614/E, NRG, The Netherlands, 2008.)*
6. Two-sided messages with refutations are more effective than one-sided messages in the framework of health care communication, provided that the negative arguments in the communication are clearly present. *(T.S. de Brabander, Het inzetten van tweezijdige boodschappen in gezondheidscommunicatie, Master thesis, Universiteit van Amsterdam, 2014.)*
7. Bureaucratization leads to rationalization of human life, limiting individual freedom by excessive rule-based, rational control. *(R. Swedberg and O. Agevall, The Max Weber dictionary: key words and central concepts, Stanford University Press, ISBN 978-0-8047-5095-0, 2005.)*

8. The more than 100 terminations of NRC (a Dutch newspaper) subscriptions and the many critical reactions by readers as a reaction on the granting of a column in NRC to PVV-politician Martin Bosma illustrates that people do not use news media as an objective source of information, but to be confirmed in their own world-view.
(<http://www.nu.nl/media/2745843/ruim-40-opzeggingen-nrc-artikel-friso.html> (20-02-2012).
<http://www.nrc.nl/ombudsman/2010/12/04/kamerleden-hebben-al-het-beste-platform-van-heel-nederland> (04-12-2010).)
9. Active Donor Registration (yes, unless) leads to more donors and gives a better implementation of the right to self-determination than the current 'opt-in' system in the Netherlands. (*Raad voor de Volksgezondheid & Zorg, Afscheid van de vrijblijvendheid. Beslissystemen voor orgaandonatie in ethisch perspectief, Signalering ethiek en gezondheid 2008/1. Centrum voor ethiek en gezondheid, Den Haag, 2008. R.D. Friele en J.D. de Jong, Actieve donorregistratie? Een herhalingsonderzoek naar de mogelijke reactie op de introductie van het actief donorregistratiesysteem, NIVEL, 2007.*)
10. The system-integration costs of renewable energy sources into the current electricity supply system are a far greater barrier for the large-scale implementation of renewable energy sources than their installation costs. (*William D. D'haeseleer, Synthesis on the Economics of Nuclear Energy, Study for the European Commission, DG Energy, Contract Nr ENER/2012/NUCL/SI2.643067, 2013.*)

These propositions are regarded as opposable and defensible, and have been approved as such by the supervisor prof. dr. ir. T.H.J.J. van der Hagen.

Stellingen

behorende bij het proefschrift

CORE PHYSICS OF PEBBLE BED HIGH TEMPERATURE NUCLEAR REACTORS

door

Gert Jan AUWERDA

1. Niet-isotrope modellen zijn noodzakelijk om nauwkeurig warmte- en massatransport vlak naast de wand in een kogelbedreactor te simuleren. *(Dit proefschrift.)*
2. De hogere porositeit bij de randen ten opzichte van het midden van een willekeurig gestapeld kogelbed kan wel worden genegeerd bij het berekenen van de verdeling van de neutronenfluxverdeling in een kogelbedreactor, maar niet bij het berekenen van de k_{eff} of de verdeling van de vermogensdichtheid. *(Dit proefschrift.)*
3. In een reactorontwerp van een annulair kogelbed resulteert de stroomkanalisering langs de wand in een significant lagere maximale splijtstoftemperatuur tijdens zowel normaal bedrijf als tijdens een ongeluk met verlies van koeling onder druk. *(Dit proefschrift.)*
4. Een grid conversie studie gebaseerd op Richardson extrapolatie om de grid conversie index (GCI) te evalueren zou verplicht moeten zijn om de kwaliteit van een rooster te beoordelen bij het oplossen van vergelijkingen met numerieke analyse. *(P.J. Roache. Verification and validation in computational science and engineering, Hermosa Publishers, USA, 1998.)*
5. Het gebruik van geadjungeerde berekeningen met deterministische codes om 'weight windows' te genereren voor Monte Carlo neutron transportberekeningen vergroot zowel het vertrouwen in als de snelheid van deze berekeningen in vergelijking tot het gebruik van iteratieve weight-window generatoren met de Monte Carlo transport code. *(G.J. Auwerda. Assessment of weight windows generated from adjoint flux calculations, K5042/08.92614/E, NRG, The Netherlands, 2008.)*
6. Tweezijdige boodschappen met weerleggingen zijn effectiever dan eenzijdige boodschappen binnen de kaders van de gezondheidscommunicatie, mits de negatieve argumenten in de communicatie duidelijk aanwezig zijn. *(T.S. de Brabander, Het inzetten van tweezijdige boodschappen in gezondheidscommunicatie, Master thesis, Universiteit van Amsterdam, 2014.)*
7. Bureaucratisering leidt tot rationalisatie van het menselijk leven, waarbij individuele vrijheid wordt gelimiteerd door excessieve, op regels gebaseerde rationele controle. *(R. Swedberg and O. Agevall, The Max Weber dictionary: key words and central concepts, Stanford University Press, ISBN 978-0-8047-5095-0, 2005.)*

8. De ruim 100 opzeggingen van NRC abonnementen en de vele kritische reacties door lezers als reactie op het gunnen van een column in NRC aan PVV politicus Martin Bosma illustreert dat mensen nieuwsmedia niet gebruiken om objectief geïnformeerd te worden, maar om hun eigen wereldbeeld bevestigd te zien. (<http://www.nu.nl/media/2745843/ruim-40-opzeggingen-nrc-artikel-friso.html> (20-02-2012). <http://www.nrc.nl/ombudsman/2010/12/04/kamerleden-hebben-al-het-beste-platform-van-heel-nederland/> (04-12-2010).)
9. Actieve Donor Registratie (ja, tenzij) leidt tot meer donoren en geeft een betere invulling op het recht op zelfbeschikking dan het huidige 'opt-in' systeem in Nederland. (*Raad voor de Volksgezondheid & Zorg, Afscheid van de vrijblijvendheid. Beslissystemen voor orgaandonatie in ethisch perspectief, Signalering ethiek en gezondheid 2008/1. Centrum voor ethiek en gezondheid, Den Haag, 2008. R.D. Friele en J.D. de Jong, Actieve donorregistratie? Een herhalingsonderzoek naar de mogelijke reactie op de introductie van het actief donorregistratiesysteem, NIVEL, 2007.*)
10. De kosten voor het integreren van hernieuwbare energiebronnen in het huidige systeem voor elektriciteitsvoorziening zijn een veel grotere barrière voor de grootschalige implementatie van hernieuwbare energiebronnen dan hun installatiekosten. (*William D. D'haeseleer, Synthesis on the Economics of Nuclear Energy, Study for the European Commission, DG Energy, Contract Nr ENER/2012/NUCL/SI2.643067, 2013.*)

Deze stellingen worden oponeerbaar en verdedigbaar geacht en zijn als zodanig goedgekeurd door de promotor prof. dr. ir. T.H.J.J. van der Hagen.

**Core Physics
of
Pebble Bed High Temperature Nuclear Reactors**

Core Physics of Pebble Bed High Temperature Nuclear Reactors

Proefschrift

ter verkrijging van de graad van doctor
aan de Technische Universiteit Delft,
op gezag van de Rector Magnificus Prof. ir. K.C.A.M. Luyben,
voorzitter van het College voor Promoties
in het openbaar te verdedigen
op maandag 22 december 2014 om 12:30 uur
door

Gert Jan AUWERDA

Natuurkundig ingenieur

geboren te Delft

Dit proefschrift is goedgekeurd door de promotor:

Prof. dr. ir. T.H.J.J van der Hagen

Copromotor:

Dr. ir. J.L. Kloosterman

Samenstelling promotiecommissie:

Rector Magnificus,	voorzitter
Prof. dr. ir. T.H.J.J van der Hagen,	Technische Universiteit Delft, promotor
Dr. ir. J.L. Kloosterman,	Technische Universiteit Delft, copromotor
Prof. dr. R.F. Mudde,	Technische Universiteit Delft
Prof. dr. D.J.E.M. Roekaerts,	Technische Universiteit Delft
Dr. ir. J.C. Kuijper,	Nuclear Research and Consultancy Group, Petten
Prof. dr. rer. nat. H.-J. Allelein,	RWTH-Aachen, Germany
Prof. dr. F. Li,	Tsinghua University, Beijing, China

© 2014, Gert Jan Auwerda

All rights reserved. No part of this book may be reproduced, stored in a retrieval system, or transmitted, in any form or by any means, without prior permission from the copyright owner.

ISBN 978-94-6295-047-4

Keywords: Nuclear, HTR-PM, Pebble Bed, High Temperature Reactor

The research described in this thesis was performed in the section Nuclear Energy and Radiation Applications (NERA), of the department Radiation, Science & Technology (RST), of the Delft University of Technology, Delft, The Netherlands.

Printed by: Proefschriftmaken.nl || Uitgeverij BOXPress

Published by: Uitgeverij BOXPress, 's-Hertogenbosch

voor Annemarie

Financial support

Part of the work presented in this thesis was financed by DELTA, Middelburg, the Netherlands.

Contents

1	Introduction	1
1.1	Introduction	1
1.2	High temperature reactor technology	2
1.3	Pebble bed high temperature reactor designs	4
1.4	Thesis objective and outline	7
2	Macroscopic and Microscopic Packing Properties of Experimental and Computational Pebble Beds	9
2.1	Introduction	9
2.2	The PebBEx Facility	11
2.3	Computational Method	13
2.4	Comparison of Computed Bed with PebBEx Measurements	14
2.5	Measuring and Generating the 3D Pebble Bed Data	20
2.6	Pebble Bed Microscopic Stacking Properties	25
2.7	Distribution of Local Packing Fractions	30
2.8	Conclusions	32
3	Neutronics and neutron streaming	35
3.1	Introduction	35
3.2	Geometry Model	37
3.3	Cross Section Processing	40
3.4	Streaming Correction on Cross Sections	43
3.5	Results on the Infinite Cylinder	44
3.6	Application to HTR-PROTEUS Core 4.2	50
3.7	Conclusions	56
4	Turbulence modelling for porous media in pebble bed reactors	59
4.1	Introduction	59
4.2	The flow and heat transfer model	61
4.3	Calculations for SANA experiments	68
4.4	HTR-PM 3D calculations	79
4.5	Discussion and Conclusions	85

5	Effects of non-uniform porosity distributions in coupled steady state and transient analysis	87
5.1	The coupled calculation scheme	88
5.2	The HTR-PM geometry	91
5.3	Coupled steady state calculations	96
5.4	DLOFC and PLOFC transient analysis	102
5.5	Discussion and Conclusions	110
6	Conclusions and recommendations	113
6.1	Conclusions	113
6.2	Recommendations	115
	Bibliography	119
	Summary	129
	Samenvatting	131
	Acknowledgements	133
	List of Publications	135
	Curriculum Vitae	137



INTRODUCTION

1.1 Introduction

The global electricity demand is continuously growing. At the same time, there is a need to reduce the use of fossil fuels to battle problems such as climate change and air pollution. The ideal energy mix for the future is not clear, as all energy sources have their own merits and drawbacks. Wind and solar are emission free and produce no waste, but are still expensive, need a lot of space, can not be used everywhere, and suffer from intermittent electricity production, requiring storage or backup power plants. Nuclear energy is also air-pollution- and greenhouse-gas-free. Additionally, uranium is an abundant and secure resource and the electricity price produced in nuclear power plants is mostly independent of the fuel cost. Drawbacks of nuclear energy are the potential large consequences of severe accidents, and the generation of long-lived radioactive waste.

Currently, nuclear energy is an important part of the energy mix (13% of global electricity consumption in 2011 (World Nuclear Association, 2014)). In many countries, such as China and the UK, nuclear energy will stay an important part of the energy mix in the near future. Like any other technology, nuclear energy evolves in an effort to reduce or remove its drawbacks and increase its benefits. Several generations of nuclear reactors are commonly distinguished. Generation I reactors are no longer in operation. Most reactors currently running in the world are generation II reactors, and were built in the 70s and 80s. Newer reactors built from the late 90s up to the present day are generation III and III+ reactors. They have a much lower possibility of core melt accidents and a higher fuel efficiency, producing less waste per generated unit of electricity.

One of the main candidates for the next generation IV (Generation IV International Forum, 2009) nuclear reactors is the pebble bed (very) high temperature reactor ((V)HTR).

The main benefits of the pebble bed reactor include online refuelling, high coolant outlet temperature, and passive safety, a particularly desirable property in light of the Fukushima accident. Even during a complete loss of coolant and power the reactor will shut itself down and transfer its decay heat to the environment through passive means without any fuel damage. In a pebble bed reactor, the fuel is contained in graphite pebbles of 6 cm diameter. These pebbles form a randomly stacked bed inside a cylindrical or annular cavity surrounded by a graphite reflector. Helium coolant is pumped through the bed and transports heat generated in the pebbles to a heat exchanger. Typical coolant temperatures inside the bed range from a 250 °C inlet temperature to 750 °C and above at the core outlet. To more accurately predict the temperature distribution inside the randomly stacked bed that forms the core of a pebble bed reactor, a better understanding of the stochastic properties of this stacking and of the details of neutron transport and heat and mass transfer throughout the pebble bed is essential.

Below follows an introduction to high temperature reactor technology and pebble bed reactors. Section 1.3 gives an overview of past and present pebble bed reactor designs in the world. The last section states the objective and gives an overview of the contents of this thesis.

1.2 High temperature reactor technology

Already in the early days of nuclear energy, graphite moderated gas cooled reactors were employed. As the coolant is in a gaseous form and cannot vaporise, the reactors can operate at higher coolant outlet temperatures increasing their thermal efficiency. Early gas-cooled reactors used CO₂ as coolant, such as the UK/France MAGNOX reactor with a coolant outlet temperature of 415 °C, and its successor, the British advanced gas-cooled reactor (AGR) with a coolant outlet temperature of 675 °C. To reach even higher outlet temperatures, newer designs use helium as coolant. To withstand the higher core temperatures, the fuel and core are redesigned to be all-ceramic, consisting almost entirely of graphite. These high temperature reactors have coolant outlet temperatures of 750 °C and above.

Core of the helium cooled HTR technology is the TRISO (tristructural-isotropic) fuel particle. It consists of a small spherical UO₂ kernel with a typical diameter of 0.5 mm. Other fuels such as thorium, plutonium or mixed oxides and heavy metal carbide fuels are possible. The fuel is surrounded by several coating layers, see Figure 1.1. The first is a 95 µm porous carbon buffer layer designed to retain gaseous fission products. Next is an inner pyrolytic carbon layer (IPyC) of 40 µm, then a silicon carbide layer (SiC) of 35 µm, and an outer pyrolytic carbon layer (OPyC) of 40 µm. Together these coating layers act as a mini-containment around each fuel kernel, preventing the release of fission products even at very high temperatures of up to 1650 °C.

TRISO particles are used in two types of helium cooled HTRs, the prismatic block and the pebble bed reactor. In a prismatic block reactor, the TRISO particles are packed

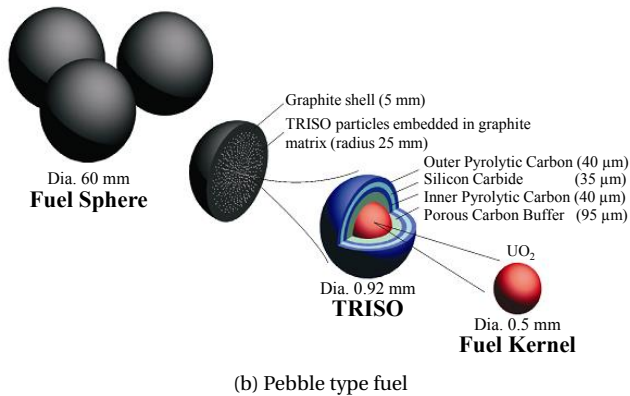
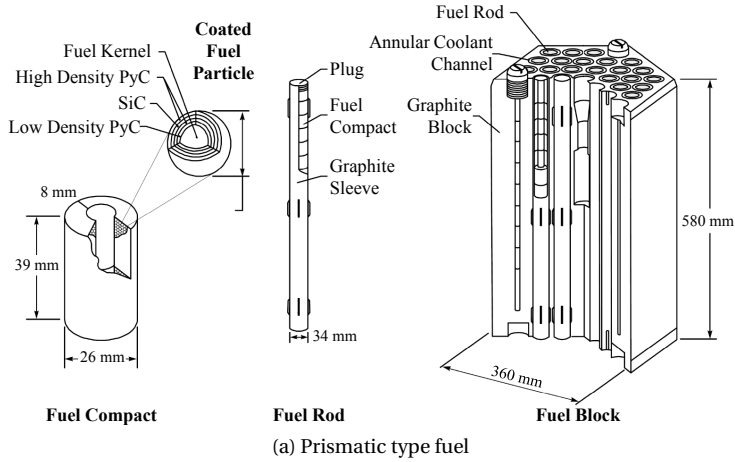


Figure 1.1: Schematic overview of HTR fuel (Boer, 2008).

within small graphite fuel compacts. These compacts have an annular shape, with inner and outer diameters of 10 mm and 26 mm, and a height of 36 mm. The compacts are stacked inside graphite sleeves to form 58 cm long fuel rods. The rods are placed in holes in hexagonal blocks, see Figure 1.1a. The core of a prismatic block reactor consists of many of these hexagonal blocks, stacked to form columns. The outer blocks forming the reflector do not contain any fuel. The reactor is cooled by helium flowing through the holes in the annular fuel compacts. As the fuel is fixed, burnable poison is used for long term reactivity control. Periodically, the reactor has to be stopped to rearrange and replace the fuel.

In a pebble bed reactor the TRISO particles are embedded in 6 cm diameter spherical

fuel pebbles made out of graphite. The central 5 cm of the fuel pebbles contain the TRISO particles in a graphite matrix, surrounded by a 0.5 cm thick graphite shell, see Figure 1.1b. One fuel pebble usually contains around 10,000 TRISO particles. These fuel pebbles form a randomly stacked bed inside a large cylindrical or annular cavity, surrounded by solid graphite reflectors. Helium flows through this randomly packed porous bed, cooling the fuel pebbles and taking away the fission heat. During operation, pebbles are removed from the bottom of the bed. These pebbles are either inserted back at the top of the core, or if their target burnup value is reached, discarded and replaced by fresh fuel pebbles. As a pebble bed reactor can be refuelled online, there is no need for excess reactivity or burnable poisons.

The main benefit of the pebble bed HTR is its passive safety. The design of a pebble bed reactor is such that during any transient it can lose its decay heat through passive means such as conduction, natural convection and radiation, without the need for power or outside intervention. As a result, severe accidents leading to large releases of radioactive materials are not possible. Several factors enable this passive safety. First, a strong negative temperature feedback ensures the swift automatic shut-down of the nuclear chain reaction following a rise in temperature, leaving only the decay power. Second, the fuel design and use of materials is such that even at very high fuel temperatures of up to 1650 °C no fuel damage occurs and all fission products are retained within the TRISO particles. [REF: The behaviour of spherical HTR fuel elements under accident conditions] Third, a relatively low power density together with the large thermal inertia of the large graphite mass of the core means the core heats up slowly after a loss of coolant incident. Finally, the tall and narrow core design enables the heat transfer from the centre of the core to the surroundings by passive means, ensuring that fuel temperatures inside the pebble bed do not rise above their design limits.

Another benefit of the pebble bed HTR is its high coolant outlet temperature. This results in an increased thermal efficiency in electricity production, which means that less fuel is used and less waste is produced per unit of electricity. The high coolant outlet temperature also opens up the possibility to use the reactor to deliver process heat for industry, for example for hydrogen production.

1.3 Pebble bed high temperature reactor designs

Over the years several pebble bed reactors have been designed. Here we give a short description of the designs that are most important for this thesis.

The German Arbeitsgemeinschaft Versuchsreaktor (AVR) was a 46 MW_{th} experimental pebble bed HTR, operated in Jülich from 1967 to 1988 (Krüger, 1989). It contained 110,000 pebbles in a cylindrical pebble bed of 2.8 m high and 3 m diameter. The core of the AVR contained four graphite noses extending from the reflector wall into the pebble bed, containing at their tip a guidance tube for the control rods, see Figure 1.2. These noses significantly affected the neutronics in the AVR, resulting in strong power peaking in the

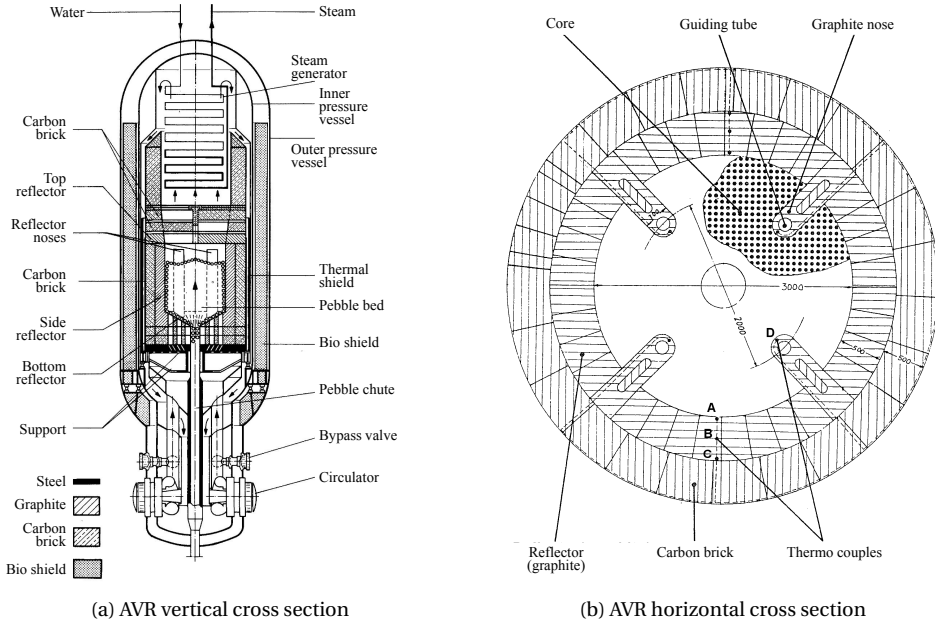


Figure 1.2: Schematic overview of the AVR (Krüger, 1989).

vicinity of the noses. In the AVR many fuel types were tested, among them the older BISO (bistructural-isotropic) fuel particles and particles containing uranium and thorium oxide or carbide fuel. Initially the reactor operated at a helium coolant outlet temperature of 850 °C, but this was later increased to 950 °C. The helium pressure was 11 bar.

The Thorium High Temperature Reactor (THTR-300) was a prototype pebble bed HTR built and operated in Germany from 1983 to 1989, with a thermal power of 750 MW, producing 308 MW of electricity (Oehme and Schoening, 1970). Its 6 m high 5.6 m diameter cylindrical pebble bed consisted of 675,000 fuel pebbles, containing a mixture of thorium and highly enriched uranium oxide fuel. It operated at helium coolant inlet and outlet temperatures of 250 °C and 750 °C with an operating pressure of 40 bar. Due to its large core size, the THTR-300 had a prestressed concrete pressure vessel instead of the usual steel pressure vessel. Besides the 36 control rods in the side reflector, it had 42 shutdown rods which moved through the pebble bed. To drive these rods through the bed considerable force was needed, potentially damaging the fuel pebbles.

In the 1990's South-Africa and China showed renewed interest in the pebble bed technology. In South-Africa this resulted in the design of the 400 MW_{th} Pebble Bed Modular Reactor (PBMR) (Reitsma et al., 2006), see Figure 1.3a. The helium coolant enters the core at 500 °C and exits the core at 900 °C at an operating pressure of 90 bars. To retain its

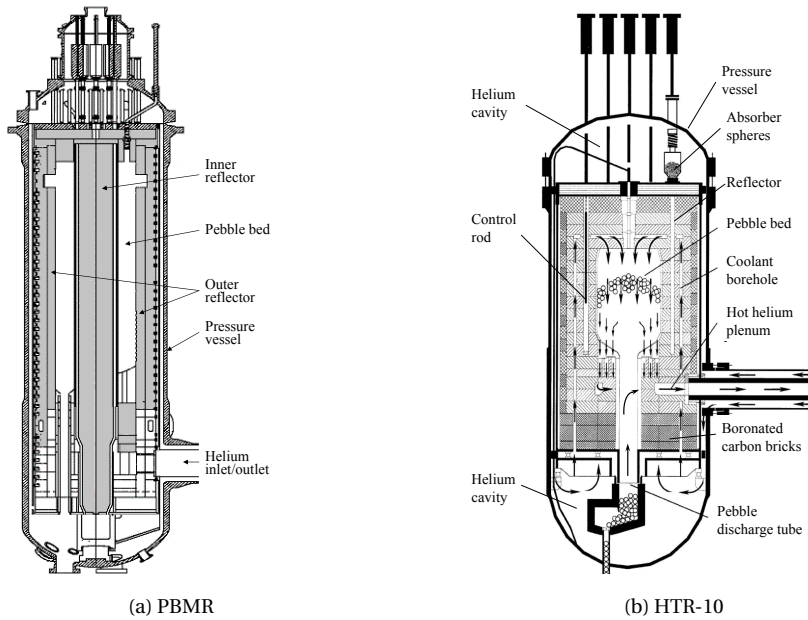


Figure 1.3: Schematic overview of the PBMR and HTR-10 reactors.

passive safety features at the higher reactor power and operating temperature the core consists of an annular pebble bed with a solid graphite inner reflector. The pebble bed has inner and outer diameters of 2.0 and 3.7 m, is 11 m high, and contains 452,000 pebbles. Its design includes a direct Brayton cycle with a helium turbine to generate electricity instead of the Rankine steam cycle. Although a lot of work was performed in designing the PBMR, the project never left its design stage and is currently dormant.

The Chinese pebble bed programme is at present the most advanced in the world. A small experimental high temperature test reactor of 10 MW_{th}, the HTR-10, is in operation since 2000, and the first twin unit pebble bed power plant is currently under construction. The HTR-10 (Wu et al., 2002) was constructed from 1995 to 2000 near Beijing, see Figure 1.3b. It was built to verify and demonstrate the technical and safety features of modular HTRs and to establish an experimental base for HTR related technology. Its cylindrical pebble bed has a diameter of 1.8 m and an effective height of 1.97 m and contains 27,000 pebbles. Each pebble contains approximately 10,000 TRISO particles with 17% enriched uranium oxide. The helium coolant inlet and outlet temperatures are 250 °C and 700 °C at an operating pressure of 30 bar.

Next step in the Chinese pebble bed high temperature reactor programme is the 250 MW_{th} High Temperature Reactor Pebble bed Modular (HTR-PM) design (Zhang et al.,

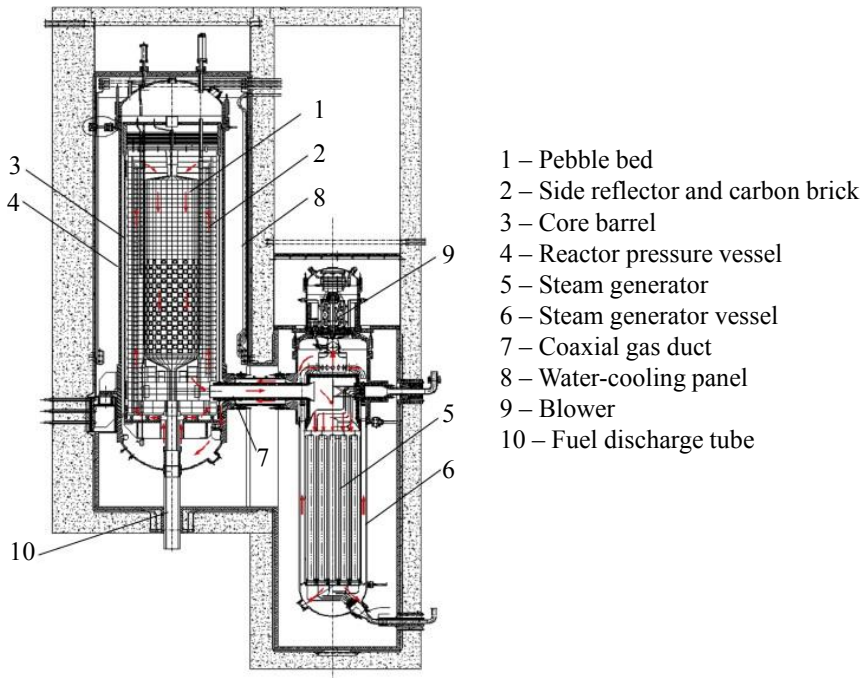


Figure 1.4: Schematic overview of the primary loop of the HTR-PM (Zheng et al., 2009).

2009), see Figure 1.4. A prototype 210 MW_e power plant formed by twin HTR-PM units driving a single steam turbine is currently under construction. Core of the HTR-PM is an 11 m high, 3 m diameter cylindrical pebble bed containing 420,000 pebbles. The reactor uses 8.9% enriched uranium. The helium coolant inlet and outlet temperatures are 250 °C and 750 °C at an operating pressure of 70 bar. Should construction and operation of the first HTR-PM be a success, an additional 18 HTR-PM units are planned at the same site.

1.4 Thesis objective and outline

The stochastic nature of its core geometry makes pebble bed reactors different from most other reactors. Inside the core the pebbles form a randomly stacked bed, and we have no prior knowledge of the exact geometry or location of the pebbles. Additionally, the pebbles are moving as the reactor is refuelled online by taking pebbles out at the bottom and reinserting them at the top. Pebbles pass through the core several times before being discarded, resulting in a mixture of pebbles at various stages of the burnup inside the core. Thus, inside a pebble bed HTR the exact location and burnup of the fuel is unknown. We

only have stochastic knowledge such as averages and probability distributions to describe the core geometry.

The objective of this thesis is to investigate the stochastic properties of the pebble bed core, and investigate the effects of the non-homogeneity of the core on the neutronics and thermal-hydraulics. First, in Chapter 2 the geometric structure of randomly stacked beds is investigated using both experimental and computational techniques. Once the stacking properties and their variations are understood, the effect of the stochastic geometry on the neutronics is investigated in Chapter 3. Topics of investigation include neutron streaming through the void space between the pebbles, the Dancoff factor, and variations in packing fraction near boundaries. In Chapter 4 a new thermal-hydraulics model for pebble beds is derived based on porous turbulence modelling. This chapter includes an investigation of the effect on the temperature and velocity distribution of using a more realistic pebble bed porosity distribution with lower porosities near the wall compared to a homogeneous porosity distribution. In Chapter 5 the knowledge of the previous three chapters is combined in coupled thermal-hydraulics and neutron transport calculations for both steady state and transients using a 3D quarter core model of the HTR-PM. The effect of variations in the porosity distribution in the pebble bed is investigated by comparing results of a uniform porosity distribution with non-uniform porosity distributions. The final chapter contains a discussion of the results together with recommendations for future research.

MACROSCOPIC AND MICROSCOPIC PACKING PROPERTIES OF EXPERIMENTAL AND COMPUTATIONAL PEBBLE BEDS

The content of this chapter was published in Nuclear Technology (Auwerda et al., 2013).

2.1 Introduction

In pebble bed calculations the bed is commonly modelled as a fully homogenised mixture of coolant and pebble materials using a uniform packing fraction. However, it is well known that the packing density of randomly stacked beds is not uniform, but exhibits strong fluctuations near solid boundaries, see for example Benenati and Brosilow (1962). The effect of the non-uniform pebble distribution can be significant for both neutronics, due to neutron streaming for example (Behrens, 1949; Lieberoth and Stojadinović, 1980; Auwerda et al., 2010b), as well as thermodynamics, for example due to the wall-channelling effect of the coolant flow (Schertz and Bischoff, 1969; Auwerda et al., 2011; Bader et al., 2011).

Over the years, several experiments have been performed to measure void fractions in packed beds. Benenati and Brosilow (1962) poured uniformly sized spherical lead shot into a container and then filled up the interstices with a liquid epoxy resin. Upon curing of the resin, the solid cylinder was machined in stages to successively smaller diameters and the weight and diameter of the cylinder was measured after each machining. In this manner the mean density of each removed annular ring could be determined and from its density the void fraction. Goodling et al. (1983) used a similar method, filling a

2. Macroscopic and Microscopic Packing Properties of Experimental and Computational Pebble Beds

cylinder with polystyrene spheres and then epoxy mixed with finely ground iron to fill the void. Lately, computational methods to generate randomly stacked pebble beds got more attention. du Toit (2008) applied a Discrete Elements Method (DEM) to generate void fraction profiles in pebble beds for thermal-hydraulics studies, and both Cogliati and Ougouag (2006) and Rycroft et al. (2006) used DEM to simulate pebble flow in pebble bed reactors. Kloosterman and Ougouag (2007) applied a Monte Carlo rejection method to generate pebble bed stackings for the calculation of spatially-dependent Dancoff factors. We used a method of removing overlaps (Auwerda et al., 2010a) to generate beds to investigate neutron streaming in the PROTEUS experimental facility (Auwerda et al., 2010b).

However, these studies only looked at radial and axial profiles, while a good understanding of the pebble-to-pebble microstructure of randomly packed beds is also important for various subjects. For example, the coordination number, the number of pebbles touching a certain pebble, was used by van Antwerpen et al. (2012) to develop a model to calculate the effective thermal conductivity of a packed bed. Also, detailed CFD analysis of small sections of the bed, with pebbles modelled explicitly such as in Pavlidis and Lathouwers (2011), can be an aid in developing better models and gaining a better understanding of flow and heat transfer effects in pebble beds, but require a realistic configuration of the pebbles. Finally, due to the stochastic nature of the pebble bed, local variations in packing fraction will occur, see for example Auwerda et al. (2012). These variations are a possible cause of hotspots, as a local densification in the packing will result in both a bigger resistance to coolant flow and a higher power density. If we want to analyse these non-uniformities and their effects on fuel temperature, a good description of local variations of the packing fraction is needed. To better investigate the above mentioned subjects, it is desirable to be able to computationally generate packed beds of arbitrary shapes and sizes which accurately capture both the macroscopic properties such as average packing fraction and radial packing fraction distribution, as well as the local microstructure in a randomly stacked bed.

When looking at computer generated beds, various authors have described not only global properties, but also local properties of the stacking microstructure (Mrafko, 1980; Jodrey and Torey, 1981; Wouterse and Philipse, 2006; Gan et al., 2010; Auwerda et al., 2012). However, validation of the results by comparison with experimental data was not always given. Only recently, accurate experimental data of the microscopic packing structure of randomly stacked beds has become available through the use of computer aided X-ray tomography (Reimann et al., 2006, 2008). Especially the work of Aste (2005) stands out because of the large size of the samples (up to 143,000 pebbles). Unfortunately, Aste only looked at the packing structure in the bulk of the bed far away from the walls, while in pebble bed reactors we are also interested in the packing microstructure near the wall.

The goal of this study is twofold. First, validate the packing structure of our computer generated beds both on a macroscopic and on a pebble-to-pebble level, by comparing the radial and axial packing fraction profiles and average packing fraction with measured

profiles, and by comparing various microscopic stacking properties in both the bulk of the bed and near the wall with literature and with experimental results. The second goal is to investigate the local variations in packing fraction in randomly packed beds, by calculating the probability density function of the packing fraction of small clusters of pebbles in both the bulk of the bed and near the wall, for both a computed bed and experimental results.

For validation purposes two sets of experiments were performed. The first experiment used a non-destructive method to measure very accurately the radial and axial void fraction profiles of a randomly stacked pebble bed with the PebBEx facility, see Section 2.2, which results are compared in Section 2.4 with the profiles of a computer generated bed created with a method of removing overlaps described in Section 2.3. Additionally a pebble-by-pebble image of a pebble bed containing almost 9000 pebbles was created using X-ray tomography, as detailed in Section 2.5. Stacking properties of the bed were investigated for both the inner zone away from the wall and the outer zone close to the wall, and compared with those of a computer generated bed. The packing microstructure of the beds is evaluated in Section 2.6 by looking at the probability distributions of various properties of the local packing. First we look at the coordination number, the average number of spheres in contact with a given sphere, followed by the distribution of Voronoï polyhedra, the radial distribution function, and finally the distribution of angles between the contact lines of pebbles with their common neighbour. Next, we investigate in Section 2.7 the variation in local packing fraction in the pebble beds. Here the local packing fraction is the average packing fraction of a small area of four to five pebbles in diameter. Distributions of the local packing fractions were calculated and compared for the inner and outer zone of both the generated and scanned beds. Finally Section 2.8 contains the conclusions on how realistic the computer generated bed is and on the observed variations in local packing fractions.

2.2 The PebBEx Facility

The Pebble Bed Experimental facility (PebBEx) at the Reactor Institute Delft (RID) of the Delft University of Technology has been developed to measure void fraction profiles of packed beds of pebbles using gamma-ray scanning (van Dijk, 2008). See Figure 2.1 for a schematic overview and photograph of the setup. The setup consists of a cylindrical vessel of acrylic plastic, with a height of 235 mm and an inner diameter of $D = 229$ mm. The vessel can be filled with acrylic pebbles of various sizes. For this experiment pebbles of $d = 12.7$ mm were used, resulting in a D/d ratio of 18.0. The void fraction of the pebble bed is measured using the main gamma peak at 59.5 keV of an Am-241 source. The attenuation coefficient of the used acrylic (PMMA) for this energy was experimentally determined to be $0.229 \pm 0.004 \text{ cm}^{-1}$ (Groen, 2009).

During the radial void fraction measurements the source is located above the vessel, followed by a collimator with a diameter of 1 mm, creating a narrow beam downward

2. Macroscopic and Microscopic Packing Properties of Experimental and Computational Pebble Beds

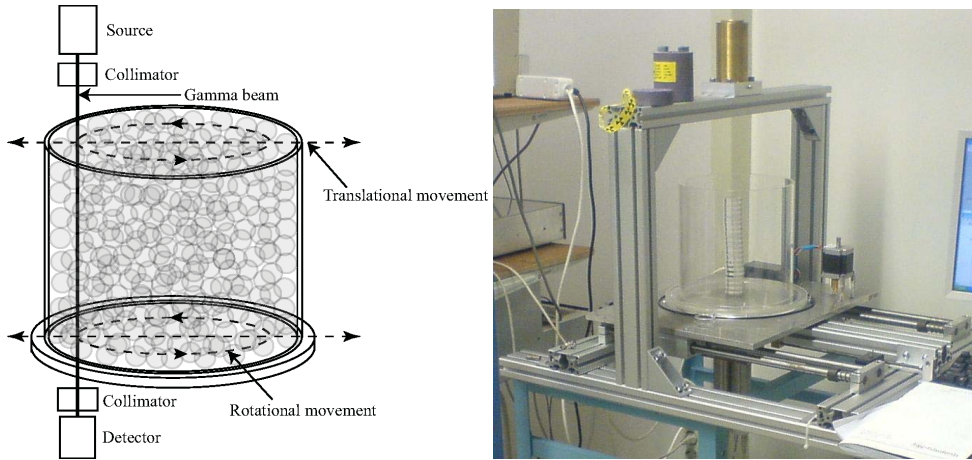


Figure 2.1: Schematic overview and photograph of the PebBEx facility, for measuring the radial void fraction profile.

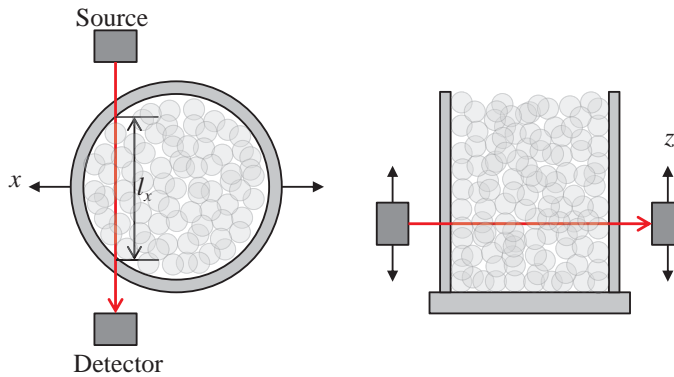


Figure 2.2: Schematic overview of PebBEx for measuring the axial void fraction profile (collimators not shown).

through the pebble bed. Below the pebble bed the intensity of the beam is measured using a NaI(Tl) scintillation detector, topped by a second collimator. From the measured intensity of the beam the amount of acrylic in the path of the gamma beam can be calculated. The vessel itself can be rotated and moved sideways using two electrical stepmotors. By measuring the void fraction while rotating the vessel the (average) radial void fraction at a certain distance from the wall can be measured. Moving the vessel sideways in between the radial void fraction measurements allows measuring the void fraction at various radial positions.

Later, the PebBEx facility was adjusted to allow the measurement of the axial void fraction of a pebble bed. To this end, the source and detector were attached to the sides of the bridge shown in Figure 2.1, with the possibility to move them up and down using a step motor and threaded rod, similar to the mode of shifting the pebble bed in the horizontal direction, see Figure 2.2. At each vertical position from the bottom of the bed, the void fraction was measured at >250 horizontal locations by moving the bed with steps of 1 mm in horizontal direction. The value of the void fraction at the vertical position was then calculated by a weighted sum of these measurements, using the distance the beam travelled through the pebble bed (l_x in Figure 2.2) at each horizontal position as a weight factor, and compensating for the changing distance the beam travelled through the cylindrical wall of the vessel.

2.3 Computational Method

In literature various numerical methods are described to generate randomly packed pebble beds. These include rigorous algorithms that simulate pebble flow as accurately as possible based on physics laws (Spedding and Spencer, 1995; du Toit, 2002), for example the Discrete Elements Method (DEM) (Abreu, 2004; Cogliati and Ougouag, 2006; Li and Ji, 2012), and synthetic techniques (Freund et al., 2003; Soppe, 1990; Julien et al., 1992), such as the Monte Carlo rejection method (Kloosterman and Ougouag, 2007) and the overlap removal method (Mrafko, 1980). Each of these methods has its own advantages and disadvantages. In our research we have developed a method based on the overlap removal method as described by Mrafko (1980), as in this method overlaps of pebbles are easily avoided, it is relatively fast for the generation of small to medium sized beds, and is straightforward to implement (Auwerda et al., 2010a).

The method consists of removing overlaps between the spheres by moving them apart, starting from a randomly generated overly dense packing of overlapping spheres. After removing all overlaps, the pebble radius is increased to its desired radius in N steps, while in each step the algorithm eliminates new overlaps among the spheres.

In the initialization step the pebble coordinates of the N_{peb} pebbles are generated inside the cylinder containing the pebble bed. This is done by generating N_{peb} random points in a volume at the bottom of the cylinder, disregarding possible overlaps. To make sure the initial distribution of pebbles is dense, the volume in which the pebbles are generated is equal to that of the N_{peb} pebbles at their initial radius R_{ini} .

The pebble radius is increased in N steps from its initial value R_{ini} to the desired final pebble radius R_{peb} . The initial radius R_{ini} is typically chosen to be $2/3$ of R_{peb} . The pebble radius is increased in ever smaller steps to increase the sensitivity of the method in each step, following a logarithmic interpolation between initial and final radius

$$R_i = R_{ini} + (R_{peb} - R_{ini}) \log\left(1 + 9 \frac{i-1}{N-1}\right) \quad (2.1)$$

with R_i the pebble radius in step i .

In each step overlaps between pebbles are removed by moving the pebbles apart. A loop is run over all pebbles, and for each pebble it is checked if it overlaps with a wall or the closest neighbouring pebble. If the pebble intersects with a wall it is moved perpendicular to the wall until it touches the wall. If the pebble intersects with its nearest neighbour, both pebbles are moved an equal distance apart along their line of intersection, until they are touching. When moving the pebbles it is allowed to create new overlaps. The program keeps checking all pebbles for overlaps until all overlaps are removed. When there are no more overlaps, the loop is exited and the pebble radius can be increased again, starting the next iteration.

As the removing overlaps model contains no gravitational force, pebbles at the top of the bed can end up in unrealistic positions, balancing on only one other pebble. To make sure the upper part of the pebble bed is still well packed and does not contain any 'floating' pebbles balancing on only one or two other pebbles, a significant amount of extra pebbles have to be simulated to interact downward. In the removing overlaps model 8500 pebbles were simulated for $N = 5$ number of steps. After the calculations were finished all pebbles not completely below 235 mm were removed.

2.4 Comparison of Computed Bed with PebBEx Measurements

This section contains the results of the experimental packing fraction measurements with the PebBEx facility compared with results from a computer generated bed using the method of removing overlaps described above. As the computational method to generate the pebble bed is also a stochastic method depending on the random initial locations of the pebbles, an arbitrary seed was taken to generate the computational bed. All results are for a 235 mm high pebble bed in a cylinder of 229 mm diameter, with a pebble diameter of 12.7 mm.

2.4.1 Average Packing Fraction ϵ_0

To fill the vessel, pebbles were quickly poured in until it was filled almost to the top, after which the remained of the vessel was filled by carefully adding pebbles at the top. To make sure the pebble bed height was as uniform as possible a plate was slowly pushed over the top of the pebble bed. The surplus of spheres which could not find a place were removed from the pebble bed. Care was taken to keep the pressure at a minimum to maintain a pebble bed stacking with a free upper surface. The number of pebbles required to fill the cylinder in this way was 5457 ± 10 pebbles (Groen, 2009), and was determined from the total weight of all pebbles. The same bed was used for the radial packing fraction profile measurement in Section 2.4.2.

The number of pebbles inside the pebble bed for both the experiment and the computed bed are shown in Table 2.1 together with the resulting average packing fraction ϵ_0 and

Table 2.1: Average packing fractions ϵ_0 and inner packing fraction ϵ_∞ , measured with PebBEx and for the computer generated bed.

Method of generation	Number of pebbles	Average packing fraction ϵ_0	Inner packing fraction ϵ_∞
Experiment	5457	0.6047	—
Computed bed	5440	0.6028	0.6315

the inner packing fraction ϵ_∞ of the computed bed, representing the packing fraction of an infinite packing without wall effects. This inner packing fraction was determined by calculating the average packing fraction in a cylinder with diameter $4/9D$ and height between $0.3H$ and $0.8H$ of the height of the larger cylinder containing the bed. These values were chosen such that the borders of the volume were at least five pebble diameters away from the wall and bottom of the bed, far enough to no longer contain any influence from the wall on the packing. As the method to generate the computed bed is also stochastic, using different random seeds will result in different realisations with slightly different packing fractions. In a previous study (Auwerda et al., 2010b) the removing overlaps method was used to generate 25 beds containing on average 6802 pebbles, with an average packing fraction of 0.6227 and a maximum deviation of this average of 0.0012.

The average packing fraction of the computed bed $\epsilon_0 = 0.6028$ was in excellent agreement with the experimental packing fraction of the PebBEx setup of $\epsilon_0 = 0.6047 \pm 0.0011$. Both are also in good agreement with other experimental results. Benenati and Brosilow (1962) found for a bed with $D/d = 14.1$ an average packing fraction of $\epsilon_0 = 0.605$, and for the HTR-10 pebble bed reactor with a D/d ratio of 30 an average packing fraction of $\epsilon_0 = 0.609$ is reported (Wu et al., 2002). The inner packing fraction is a representation of the packing fraction for an infinite randomly stacked pebble bed without boundary effects. Scott and Kilgour (1969) found for the packing fraction of an infinite randomly stacked pebble bed a value of 0.6366 ± 0.0005 by extrapolating experimental results for beds of increasing size. Comparing this value with the value in Table 2.1 for the inner packing fraction of the computed bed, we again see excellent agreement.

2.4.2 Radial Packing Fraction ϵ_r

The radial packing fraction $\epsilon_r(r)$ of the PebBEx setup was measured by Groen (2009) at radial positions 0.5 mm apart. At each position the count rate was measured for two to four full rotations of the vessel. The number of rotations depended on the count rate at the detector, with count rates ranging from 3.1 counts per second half a pebble diameter from the wall to 8 cps near the wall. At low count rates, measurement times were longer to keep the uncertainty low, resulting in more rotations of the vessel. Measurements were corrected for background, with a background of 2.51 ± 0.02 cps. As calibration measurements for the empty and full cylinder, measurements outside the cylinder for a packing fraction of $\epsilon_r = 0$ and through the wall of the vessel for a packing fraction of $\epsilon_r = 1$

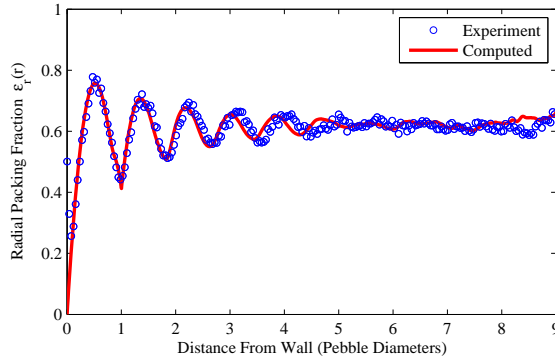


Figure 2.3: Radial packing fraction profile $\epsilon_r(r)$ measured with PebBEx and for the computer generated bed.

were used. The final uncertainty in the measurements of the packing fraction at each point was between 0.5% and 5%, depending on the local count rate, with higher uncertainty at positions with a higher packing fraction. The uncertainty in the radial position is negligible due to the high precision of the step motor used to move the cylinder. The radial packing fractions of the computer generated bed was calculated from the pebble coordinates and is, together with the experimental results, shown in Figure 2.3.

From previous experiments we know the radial packing fraction profile is zero at the wall and reaches a maximum half a pebble diameter away from the wall (Benenati and Brosilow, 1962; Goodling et al., 1983; Mueller, 1992). The profile keeps showing these oscillations in PF (packing fraction) further away from the wall, damping out at about 5 pebble diameters from the wall. Cause of these oscillations is the solid wall, imposing a local ordering on the pebbles, with a preferred position touching the wall. At the wall the radial packing fraction has to be zero, and due to the preferred position touching the wall, many pebbles will have their centre half a pebble diameter away from the wall, resulting in a maximum in the radial packing fraction at this location. The many pebbles touching the wall will also result in the next layer of pebbles having a high probability to be a certain distance away from this first layer, resulting in the next peak in packing fraction slightly before $r = 1.5d_{peb}$. These oscillations in radial PF dampen out further away from the wall, as the ordering of layers parallel to the wall becomes less and less, with no preferred ordering observable $>5d_{peb}$ away from the wall.

Although the uncertainty per point is significant for the experimental $\epsilon_r(r)$ measured with PebBEx, the oscillating behavior is very clear in Figure 2.3 due to the large number of measuring points. The oscillations are large near the wall, with a maximum packing fraction of 0.78 half a pebble diameter from the wall. The oscillations dampen out further away from the wall and disappear at about 5 pebble diameters from the wall, just as

observed in previous experiments. At the wall one would expect the packing fraction to go to zero, instead a slight increase is observed in the measurements less than 0.5 mm away from the wall. This is caused by the finite width of the gamma ray used to measure the packing fraction, created by the 1 mm wide collimator. Near the wall, part of the beam will go through the wall itself, causing additional attenuation and a higher measured packing fraction. At the other end of the measured range, at the centre of the bed, a rise in the experimental packing fraction can be observed. This is caused by the stochastic nature of the experiment itself. Near the centre of the pebble bed, the rotational path length over which the packing fraction is measured becomes very small, and thus ϵ_r is measured over a small surface. The measurements approach that of a local point, causing larger fluctuations due to local variations in packing fraction in the pebble bed. Averaging the packing fraction near the centre over multiple experiments using different realisations of the pebble bed would result in a smooth behavior of ϵ_r .

The radial PF profile of the computer generated bed is very similar to the measured profile. The oscillations dampen out just as fast as those in the experiment. However, the distance between the peaks of the oscillations is slightly shorter than that of the experiment. Although for the first two oscillations, up to two pebble diameters from the wall, the difference is hardly observable, after about five pebble diameters the shift in the radial position of the peaks is significant. The absence of gravity in the removing overlaps method could be the cause of this effect. As the pebbles form a close packing, they are pressed together and against the walls with no bias to direction. In reality, pebbles also experience a downward force by gravity. Since the wall is solid, pebbles can only move down by moving away from the wall, 'rolling' over the pebble below, thus slightly increasing the distance between the peaks in ϵ_r in the radial direction.

2.4.3 Axial Packing Fraction ϵ_z

As mentioned in Section 2.2, after measuring the radial packing fraction profile $\epsilon_r(r)$, the PebBEx facility was modified to measure the axial packing fraction profile $\epsilon_z(z)$ of packed beds. The axial measurements were performed by Baronner (2012), and he filled the pebble bed in a different way than was done for the radial packing fraction measurement. Instead of quickly pouring the pebbles in the cylinder, the cylinder was slowly filled by first taking a handful of pebbles (approximately 20 each time) and carefully putting them at the bottom of the bed, repeating this process several times. After covering the bottom of the bed, the rest of the bed was filled by slowly and carefully pouring pebbles along the wall of the slightly tilted cylindrical container into the bed. As the axial packing fraction near the top of the bed was not measured, the bed was not completely filled to the top, and no measures were taken to get a flat top of the pebble bed. Unfortunately, this filling procedure meant the average packing fraction of the bed could not be calculated from the number of pebbles in the bed.

To get a lower uncertainty per measurement point, a 2 mm wide collimator was used instead of the 1 mm wide collimator for the radial packing fraction measurements, result-

2. Macroscopic and Microscopic Packing Properties of Experimental and Computational Pebble Beds

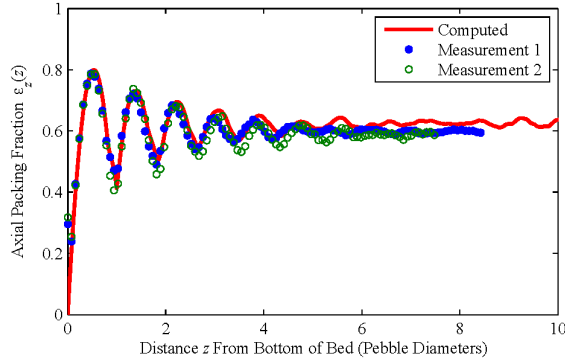


Figure 2.4: Axial packing fraction profile $\epsilon_z(z)$ measured with PebBEx and for the computer generated bed.

ing in a higher count rate and a much lower uncertainty in the measured packing fraction, less than 1% for all points. Measurements were performed at axial positions 1 mm apart. A drawback of using the relatively wide collimator (2 mm equals $0.08d_{peb}$) is that the resulting measured void fraction at each point is actually a local average and sharp peaks are smeared out, resulting in a smoother measured profile than the true profile.

After measuring the axial PF profile (measurement 1 in Figure 2.4), the cylinder was emptied and filled anew, and a second axial PF profile was measured (measurement 2). To save time, the second measurement was performed faster, resulting in a higher uncertainty per measurement point of approximately 2%. For a more detailed description of the measurements see Baronner (2012). The axial packing fraction profile was also calculated for the computed bed, using the same bed as for the radial packing fraction in the previous section. The resulting measured and computed axial packing fraction profiles are given in Figure 2.4. To save time, ϵ_z was measured up to a distance of $z = 8.5d_{peb}$ from the bottom of the bed, as the axial packing fraction more than 5 pebble diameters away from the bottom of the bed shows only statistical variations due to the stochastic nature of the bed.

For both measurements, the axial packing fraction in the bulk of the bed, $> 5d_{peb}$ above the bottom of the bed, is significantly lower than that of the computed bed, and also lower than the measured radial packing fraction away from the wall in Figure 2.3. As there was a good match between the computed bed and the radially measured packing fraction, we conclude that the average packing fraction of the beds for the axial measurement was lower than that of the bed used for the radial measurement. This lower average PF is most likely caused by the more gentle method in filling the beds for the axial measurements, resulting in less movement of the pebbles during filling.

As expected, the axial PF profiles close to the bottom of the bed are very similar to

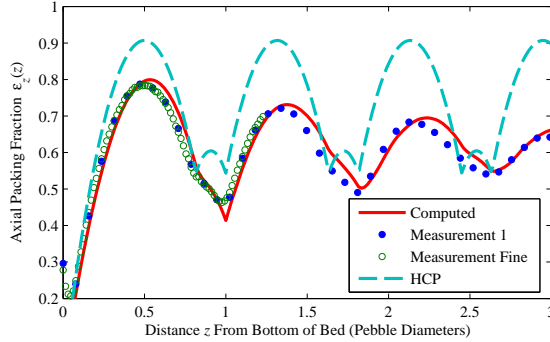


Figure 2.5: Coarse and fine measurement of the Axial packing fraction profile $\epsilon_z(z)$ measured with PebBEx compared with that of the computer generated bed and a perfect hexagonal close packing (HCP).

the radial PF profile, with similar minima and maxima, again damping out after about 5 pebble diameters away from the bottom. The match of the measurements with the computed bed is very good, especially for the second measurement. More than two pebbled diameters from the bottom, the peaks of the first measurement are slightly closer together and as a result lie at a lower axial position. As mentioned in the previous section, this could be due to gravity, as this will force pebbles more strongly downward, causing the partly ordered layers parallel to the wall to lie closer together than for the radial PF profile. However, the second measurement shows extrema locations matching those of the computed bed, indicating that the stochastic nature of packed beds can result in significant variations in the packing fraction profiles, especially for a relatively small bed as in this experiment. For larger beds one would expect less variations between packing fraction profiles of different beds, although it should be noticed that locally variations will still exist.

To get a more accurate description of the shape of the axial packing fraction profile near the wall, the PF of the first bed was measured in steps of 0.2 mm in the z -direction. Results are in Figure 2.5, together with the original, coarser measurement and the computed profile. Also added for comparison is the axial packing fraction profile of a perfect hexagonal close packing (HCP) of spheres. The first thing to notice is the exact match between measurement 1 and the fine measurement, proof of the reproducibility and accuracy of the measurement method. There is also a very good match with the shape of the PF profile of the computed bed. Although the minimum at $z = 1d_{peb}$ does not show the same sharp peak for the measurement as for the computed bed, it would be hard to reproduce with the measurement method, due to the width of the collimator.

In literature the PF profile near a wall has sometimes been described using a sine or other periodic functions (Mueller, 1992), however, we can see from Figure 2.5 that this

is not correct. First, the profile decreasing to a minimum is not smooth, but starts to decrease more slowly close to a minimum. Second, the distance from a maximum to a minimum is around $0.5d_{peb}$, but the distance from a minimum to a maximum in positive z -direction is smaller, around $0.35d_{peb}$. The reason is the semi-ordered sheets of pebbles parallel to the bottom of the bed. The first maximum in PF at $z = 0.5d_{peb}$ is at the location of many pebble centres touching the bottom. The first minimum is at $z = 1d_{peb}$, $0.5d_{peb}$ from the location of the pebble centres of the first layer. Above this layer, a next layer of pebbles has a preferred position, slightly embedded in between the first layer. This layer has a preferred pebble centre at the location of the second maximum, which is less than $0.5d_{peb}$ from the minimum at $z = 1d_{peb}$, as the pebbles of this second layer lie in between the pebbles of the first. This is also the reason of the change in shape of the profile, just before the minimum at $z = 1d_{peb}$, but exactly $0.5d_{peb}$ before the second maximum. Here the second layer of pebbles starts to contribute to the PF, resulting in a lower decrease of the PF. This pattern keeps repeating itself further away from the wall, damping out as the layers become less ordered due to the stochastic nature of the bed. When comparing the profiles with the HCP profile, we can see the locations where the profile starts to decrease more slowly exactly matches the locations where the HCP profile starts to increase toward its smaller maximum. We also see an almost perfect match between the locations of the maxima and minima of the HCP profile with the other profiles. Both are indicators randomly stacked beds form hexagonal-like sheets parallel to walls, increasing in disorder further away from the wall.

2.5 Measuring and Generating the 3D Pebble Bed Data

As mentioned in the introduction, after evaluating our computer generated beds using macroscopic stacking properties, we will look at the microscopic stacking properties on a pebble-to-pebble scale. For comparison, the locations of all pebbles in a pebble bed were experimentally determined using computer aided X-ray tomography, see Section 2.5.1. In Section 2.6 various microscopic stacking properties are compared with those of a computed bed, generated using the expanding system method described in Section 2.3, and with literature.

2.5.1 Measuring the 3D Pebble Bed Data

Computer aided X-ray tomography was used by van Dijk (2011) to create an image of a randomly packed pebble bed 42 mm high and with a diameter of 40.0 mm, containing 8920 pebbles. The pebbles were made of glass and had an average diameter of 1.93 mm, resulting in a D_{bed}/d_{peb} ratio of 20.7. The average particle diameter of 1.93 mm was determined with an accuracy of 0.01 mm by first determining the average particle volume by measuring the volume of all particles and dividing it by the number of particles, and from that calculating the average particle diameter assuming perfectly spherical particles. Unfortunately the pebbles were neither perfectly spherical, nor very uniform in diameter. The distribution of the particle sizes is not known, as it was difficult to determine due

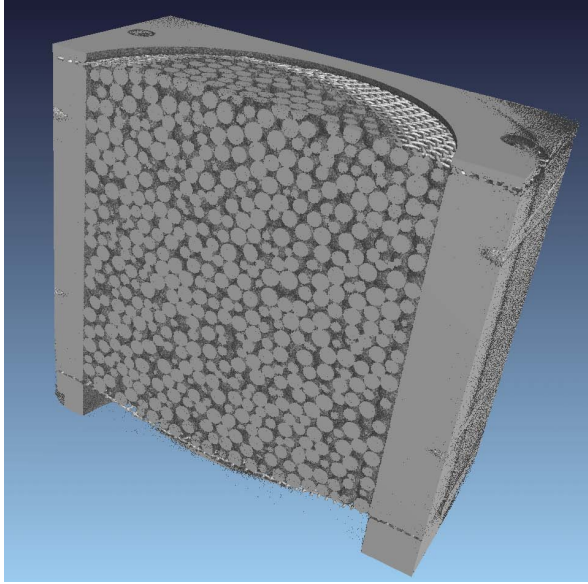


Figure 2.6: Image of the scanned bed with diameter 40 mm inside the placeholder, reconstructed using the voxels data (van Dijk, 2011).

to the particles not being perfectly spherical. Variations between the minimum and maximum diameter of a single particle depending on its orientation could easily vary 0.1 mm or more, with diameters for all particles ranging from 1.66 to 2.00 mm. To scan the bed it was encased in a cylinder made of PVC, and the top and bottom of the bed were constrained by steel wire-meshes, tightly fitted over the particles. Because of this tight fit, the top and bottom of the bed are slightly convex. Care was taken not to disturb the stacking while immobilising the bed with the steel wire-meshes, so that the pebble bed would remain uncompressed, albeit secured. See Figure 2.6 for an image of the bed reconstructed from the measured data.

The spatial resolution of the scan was $100\text{ }\mu\text{m}$, about 20 times smaller than the pebble diameter. The output of the CT scanner is a greyvalue for each cell in the measuring domain, a 3D grid representing the spatial location of each cell. Each of these cells represents a volume pixel (voxel) of $100\text{ by }100\text{ by }100\text{ }\mu\text{m}$. The greyvalue is a measure for the attenuation of the X-ray at the voxel location, and thus of the amount of solid material at the voxel. To translate the greyvalues to pebble-air data, a threshold value was chosen to translate them to either 0 (void) or 1 (pebble). In the rest of this paper we will refer to this data as the voxels data. To analyse the characteristics of the bed the positions of the centres of each sphere was needed. First, the amount of solid within a sphere of radius $R_{peb} = 0.965\text{ mm}$ was calculated at every voxel location. Next, this data was searched for

2. Macroscopic and Microscopic Packing Properties of Experimental and Computational Pebble Beds

maxima to obtain the pebble centre locations, which from now on we will refer to as the pebbles data. It should be noted that for constructing the pebbles data we assumed that all pebbles have the same radius $R_{peb} = 0.965$ mm.

Various factors contribute to the uncertainty in the pebble locations of the resulting pebbles data set constructed from the X-ray scan. First, although the spatial resolution of the X-ray scanner was reported to be $10\text{ }\mu\text{m}$ (van Dijk, 2011), the actual voxel size in the experiment was $100\text{ }\mu\text{m}$, resulting in a spatial uncertainty of 0.1 mm. Second, the resulting data from the scan was a grayvalue, which has an intrinsic uncertainty due to the stochastic process of X-ray scanning, and also includes uncertainties due to the algorithm used to construct the data for each voxel in the software of the scanning machine. From the greyvalue distribution reported by van Dijk (2011) we can assume this effect is small for most voxels as the solid and void peaks in greyvalue lie far apart. However, near solid/void interfaces it is harder to determine whether a voxel is solid or void, and especially around interfaces of contacting pebbles this can result in a much larger solid area around the contact area of the two pebbles. This is even more problematic near the wall of the vessel, as there the contact between the convex pebble and the concave wall results in a relatively large space where the void gap is very small. We estimate that this effect adds another 0.1 mm uncertainty to the algorithm that finds the pebble centre locations, and possibly more just next to the wall. Finally, we estimate the pebble size and shape distribution results in an uncertainty of up to 0.3 mm in determining the pebble centre locations, depending on the magnitude of the deviation in size and shape of the pebble under consideration from the average. Together this results in an estimated 0.1 - 0.3 mm uncertainty in the pebble locations. Additionally, there is also an uncertainty in where exactly the centre of the bed lies, and thus where the wall is, resulting in an uncertainty in the radial distance of a pebble from the wall, estimated to be 0.1 mm.

2.5.2 Computer Generated Bed

The computed bed was generated using the removing overlaps method detailed in Section 2.3. In the previous section, we showed that the computer generated beds accurately capture the macroscopic behavior of real pebble beds. To investigate the microscopic properties a large bed was generated to ensure sufficient empirical data to construct accurate probability density functions of the various properties of the packing microstructure. The bed is cylindrical with a bed over pebble diameter factor of $D_{bed}/d_{peb} = 50$, has a flat bottom, and contains 67,500 pebbles. When analysing the bed, only the section between 5 and 25 pebble diameters from the bottom is used to make sure there are no effects from the bottom or top of the bed inside the domain under consideration.

2.5.3 Radial and Average Packing Fraction

To investigate differences in packing structures in the bulk of the bed and near the wall, we investigated the properties of the beds in two separate regions, an inner and an outer zone.

Table 2.2: Packing fraction for inner ($>2.5d_{peb}$ from wall), outer ($\leq 2.5d_{peb}$ from wall), and total volume for the three data sets.

Data set	Inner PF	Outer PF	Total PF
Computed	0.634	0.624	0.632
Scan - spheres	0.633	0.608	0.622
Scan - voxels	0.646	0.620	0.635

The inner zone is the part of the bed more than $2.5d_{peb}$ away from the wall, and the outer zone the part within $2.5d_{peb}$ from the wall, where fluctuations in the porosity profiles and thus wall effects are large. Although between 2.5 and $5d_{peb}$ from the wall fluctuations exists, these are strongly dampened, and stacking properties are expected to be similar to those in the centre of the bed. Also, the stacking properties analysed do not consider just a single pebble location, but also at the pebbles surrounding it, sometimes up to several pebble diameters away. Thus we decided to look for the outer zone at pebbles less than $2.5d_{peb}$ from the wall, to get a clear picture of stacking properties close to the wall, where wall effects on the packing are strong. When choosing a boundary between outer and inner zone further away from the wall, stacking properties for the two zones became similar, making it harder to distinguish between properties close to the wall and in the bulk of the bed. For both zones, we only consider the part of the bed at least 5 pebble diameters away from the top and bottom of the bed.

The packing fractions of the inner and outer zones of the computed bed and the spheres and voxels data sets of the measured bed are given in Table 2.2 together with their total packing fraction. The radial packing fraction profile of the three data sets was also calculated, see Figure 2.7. The computed bed has a D_{bed}/d_{peb} ratio of 50, so only the first part of its packing fraction profile is shown to better fit the figure. We have seen in Section 2.4 that the computational method generates beds with realistic average packing fractions and packing fraction profiles, so this comparison can tell us something of the quality of our measured spheres and voxels data sets.

First we see a significantly higher inner zone PF for the voxels data set than for the computed bed in Table 2.2 and in Figure 2.7 where the radial packing fraction for the voxels data is higher than the other two for $r > 5d_{peb}$. A possible cause could be the non-uniform pebble size and not perfectly spherical pebbles, resulting in a higher packing fraction, but it could also be a result of noise in the measurement data causing erroneous solid voxels in the void space between pebbles. The packing fraction of the outer zone of the voxels data and computed bed compare reasonably well, but that of the spheres data is lower. This is also visible in the radial packing fraction profile in Figure 2.7, where the spheres packing fraction is slightly lower than that of the voxels data. More importantly, there is also a mismatch between the spheres data and the voxels set in the shape of the profile $<1d_{peb}$ to the wall. This suggests that near the wall our algorithm has trouble finding the correct location of the pebble centres from the voxels data, and for some

2. Macroscopic and Microscopic Packing Properties of Experimental and Computational Pebble Beds

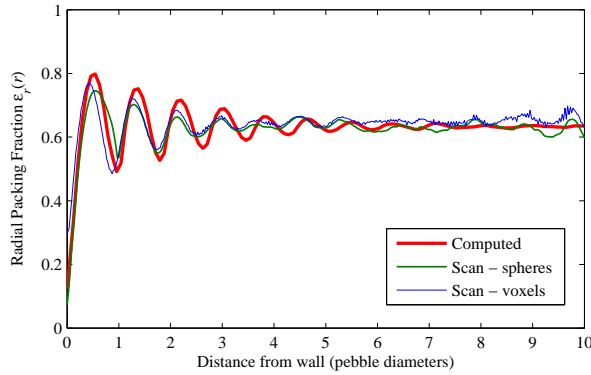


Figure 2.7: Radial packing fraction profile for the computed bed, for the voxels measurement data from the tomography scan, and for the pebble centre locations (spheres) derived from the voxels data.

pebbles it either cannot find the correct location or does not find the pebble at all, causing the lower packing fraction. A possible reason is the interference of the wall with the algorithm, where the solid voxels of the wall make it difficult to find the correct locations of the spheres. As was explained before, the large number of solid voxels making up the wall and surrounding the interfaces between the wall and pebbles in contact with it, makes it harder for the algorithm to correctly identify the border between the pebble and the wall, resulting in a higher uncertainty as to the determined pebble centre locations in this region.

At a distance $>1d_{peb}$ away from the wall the match between the three profiles is better. The scanned profiles are more dampened than the computed profile, but that is expected due to variations in pebble size, uncertainties in pebble locations, and measurement errors. The larger variations in packing fraction for the voxels and spheres data near the centre of the bed at $r = 10d_{peb}$ are also expected, as here the volume over which the profile is calculated becomes very small, causing statistical variations. In all three profiles the variations in packing fraction dampen out around $5d_{peb}$ from the wall as expected (Benenati and Brosilow, 1962; Auwerda et al., 2010a), and all three profiles show the same distance between the maxima and minima of the packing fraction profile. Summing up, the results give us a fair amount of confidence in the correctness of the spheres data set for most of the domain. Close to the wall more doubt on the accuracy of the spheres data set exists.

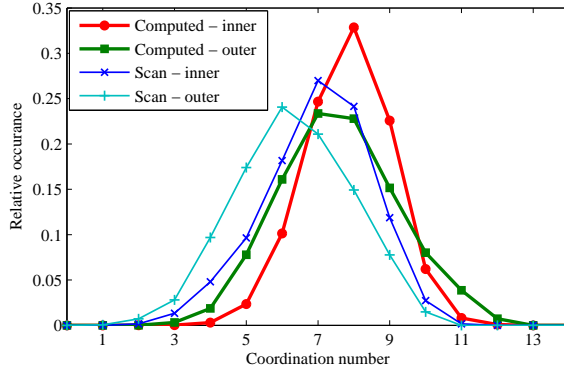


Figure 2.8: Distribution of the coordination number for the inner (bulk) and outer (near-wall) zones of the computed and measured beds. Pebbles within $1.05 d_{peb}$ were counted as neighbours.

2.6 Pebble Bed Microscopic Stacking Properties

In this section various properties of the stacking microstructure of the computer generated and measured pebble beds are calculated and compared. From this point onward, when we talk about the scanned bed, we talk about the spheres data set of the measured bed, see Section 2.5.1, as the pebble centres are needed to determine the various stacking properties. As mentioned in Section 2.5.3, we have calculated the stacking properties of the outer zone near the wall and the inner zone separately to investigate possible spatial differences in the stacking properties.

2.6.1 Coordination Number

The coordination number of a sphere in a packing is the number of surrounding spheres in contact with that given sphere, and is a commonly investigated parameter in the literature on packed beds (Jodrey and Toney, 1981; Wouterse and Philipse, 2006; du Toit et al., 2009). Besides being an important property of the local packing structure, it is also an important parameter for the effective thermal conductivity of a packed bed, as the pebble-to-pebble contact conduction is an important part of this (van Antwerpen et al., 2009, 2012). One of the inherent problems of the coordination number is how to define spheres in contact, especially when dealing with experimental data containing uncertainty. Here we follow a common approach to count all pebble centres within a certain distance $d_{peb} + \delta$ of the reference pebble. In our case we use $\delta = 0.05 d_{peb}$ so that we get the number of pebbles within $1.05 d_{peb}$, identical to the approach followed by Aste (2005). The resulting probability density distribution of the coordination number for the inner and outer zones of the computed and scanned beds are depicted in Figure 2.8.

2. Macroscopic and Microscopic Packing Properties of Experimental and Computational Pebble Beds

The theoretical maximum number of spheres touching a central sphere is 12, and indeed all four probability density functions of the coordination number have zero probability for 13 and up. To be stable, a pebble needs at least three contacts for support, which leads to a minimum value of the coordination number of three in the bulk of the bed, and two at the wall, where the wall can be one of the support contacts. Again, the probability density functions abide by this rule, although for the scanned bed in the outer zone there is a very small probability of one contact and in the inner zone of two contacts, which we contribute to uncertainties in the pebble locations and sizes.

The distributions of the coordination number of the inner zone of the computed bed shows a clear maximum at 8, with a probability around 0.33. Although the agreement with our scanned bed is not so good, agreement with the experimental results reported by Aste (2005) is excellent, showing an almost identical shape of the distribution function. The lower coordination number of the scanned bed can be explained if we look at the radial distribution function discussed in Section 2.6.3, see Figure 2.10. Here the peak around $1d_{peb}$, relating to pebbles in (near) contact, shows a clear widening as a result of measurement and pebble size uncertainties, resulting in part of the peak falling outside the range $r < 1.05d_{peb}$.

Comparing the results for the inner zones with those of the outer zones near the wall, both the scanned and the computed bed show peak values at a lower contact number for the outer zone, and in general a higher probability on lower contact numbers. This seems logical, as near the wall there is a lower packing fraction, see Table 2.2, and at the wall pebbles will have a lower contact number due to the wall itself. However, the computed bed shows in the outer zone also a higher probability for pebbles with a very high contact number of 10-12. These high contact numbers indicate a high level of ordering around some spheres, and correspond to the coordination number of hexagonal close packing.

2.6.2 Distribution of Packing Fraction of Voronoï Polyhedra

One way to look at the local distribution of space of spherical packings is by dividing the space into Voronoï polyhedra (Voronoi, 1908). The Voronoï polyhedron around each pebble is formed by the space closest to the pebble center with respect to any other pebble center in the packing. To construct the polyhedra we used an algorithm detailed by Finney (1979). To calculate the Voronoï polyhedra for the pebbles close to the wall, imaginary pebbles were constructed such that the plane through the middle of their connection lines with the real pebble was tangent to the cylinder enclosing the pebble bed. Because several imaginary pebbles were used for each pebble, this method is fairly accurate, and will result in only a very small over-estimation of the volume of the Voronoï polyhedra at the wall.

The packing fraction of each individual Voronoï volume was calculated with $PF_i = V_{peb}/V_{Voronoi}$, and the results were used to construct the distribution of Voronoï packing fractions in Figure 2.9. Again the results were separated in an inner zone, with pebbles

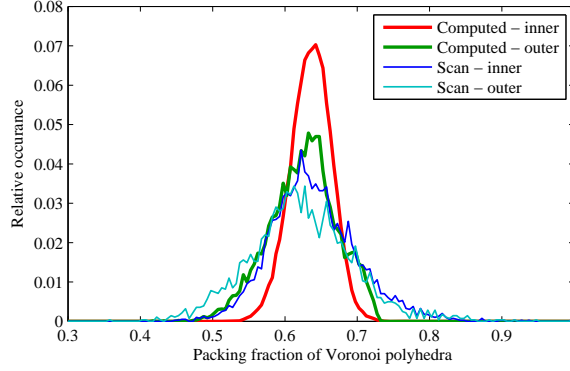


Figure 2.9: Distribution of the packing fraction of the Voronoi polyhedra for the inner (bulk) and outer zones (near-wall) of the computed and measured beds.

$> 2.5d_{peb}$ away from the wall, and an outer zone with pebbles within $2.5d_{peb}$ of the wall. Results are depicted for both the computed and the scanned bed, where the spheres data was used for the scanned bed. Due to the limited number of pebbles in the scanned bed, the data of the histograms contains significant stochastic variations. The same applies, although to a lesser degree, to the number of pebbles in the outer zone of the computed bed.

The distribution for the inner zone of the computed bed is non-symmetric with a longer tail at low PFs, a maximum occurring PF value of 0.736, and a minimum of 0.505, again similar to results found by Aste (2005). The outer zone of the computed bed has a lower peak value than the inner zone at the same PF, with a much broader and longer tail at low PF. This big tail at low PF, with a minimum PF of 0.415, is caused by the pebbles next to the wall. The maximum PF is the same as for the inner zone, corresponding to the maximum attainable packing fraction of 0.7405 for a hexagonal close packing. Finally we observe a higher probability of high PFs, suggesting a high ordering in the near-wall region of the stacking with pebbles forming closely packed layers parallel to the wall.

The packing fraction distributions for the scanned bed shows a broader distribution than the computed distributions due to the variations in pebble size and uncertainties in measured pebble position. As we assume a uniform sphere diameter in the algorithm to find the sphere centres from the scan results, if the spheres in reality are smaller or larger, this will cause either gaps between spheres or overlapping spheres in the derived pebble centres data set. Also, errors in the derived sphere locations will result in sphere centres being either too far apart, resulting in gaps, or too close together, again resulting in overlapping spheres. This results in distorted polyhedra, where the packing fractions above 0.74 are caused by overlapping spheres. The significant number of polyhedra with these larger packing fractions indicate there are many overlapping pebbles in the spheres

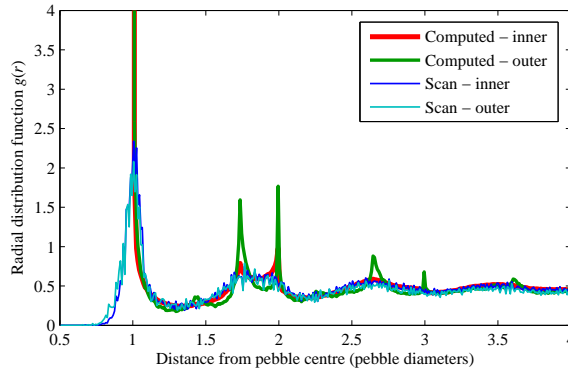


Figure 2.10: Radial distribution functions of the inner (bulk) and outer zones (near-wall) of the computed and measured beds.

data set derived from the scan, and the fact some polyhedra have packing fractions of up to 1 for the inner zone show these overlaps can be large in this region. Still visible for the distribution of the outer zone is a lower peak and a larger probability of low packing fractions, but an increased probability of polyhedra with high packing fraction cannot be observed.

2.6.3 Radial Distribution Function

The radial distribution function $g(r)$ is often used in geometrical characterisation of packing structures to determine the correlation between particles within a system (Jodrey and Torey, 1981; Aste, 2005; Wouterse and Philipse, 2006). It is defined as the probability of finding the centre of a particle at distance r from a reference one. We calculated $g(r)$ by counting the number of sphere centres N in a shell with width $dr = 0.01d_{peb}$ around r and using $g(r) = N/(V_{shell}/V_{peb})$ with V_{shell} the volume of the shell around dr , so that for large r $g(r)$ will tend to the average packing fraction. Results for the inner and outer zone of the computed and scanned bed are shown in Figure 2.10.

For the computed bed $g(r)$ has a sharp peak at $1d_{peb}$, associated with spheres in direct contact. Next there are two smaller peaks at $\sqrt{3}d_{peb}$ and $2d_{peb}$, which were also observed in previous experiments (Aste, 2005) and simulations (Jodrey and Torey, 1981). The peak at $\sqrt{3}d_{peb}$ corresponds to four spheres forming a diamond of two equilateral triangles in the same plane, whereas the peak at $2d_{peb}$ is due to three spheres lying along a (rather) straight line. Although these smaller peaks indicate some ordering in the bed, the absence of further peaks for the inner zone and the small height of the peaks indicate this ordering is minor and on a very local scale only. In the outer zone however these peaks are much more pronounced, and $g(r)$ shows more peaks. These extra peaks correspond to typical distances in a hexagonal close packing, indicating that pebbles near the wall form planes

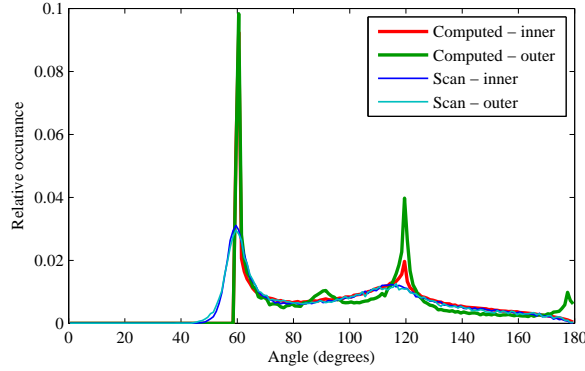


Figure 2.11: Distribution of the angles between the contact lines of two pebbles and their common neighbour for the inner (bulk) and outer zones (near-wall) of the computed and measured beds.

parallel to the wall ordered in a roughly hexagonal pattern.

The results for the scanned bed show similar behavior, although the peaks at $\sqrt{3}d_{peb}$ and $2d_{peb}$ are much less resolved due to errors in position and variations in pebble size. For the outer zone no increase in ordering can be observed as there are no extra peaks. Question is if our computational bed is inaccurate in the near wall region, or if the absence of more peaks in the outer zone is due to errors in the measurement and data manipulation, or if the added randomness in the stacking due to variations in pebble size and sphericity result in less ordering in the scanned packing itself.

In light of this it is useful to look at $g(r)$ for $r < 1d_{peb}$, which gives a measure of the amount and size of overlaps in the spheres data reconstructed from the scan. Some overlap is acceptable, however, pebble centre distances as small as $0.65d_{peb}$ where observed, visible as non-zero values of $g(r)$ in Figure 2.10, indicating large overlaps exists in the spheres data. Also, the number of larger overlaps ($r < 0.9d_{peb}$) is significant, especially for the outer zone, with $g(r)$ values showing these large overlaps occur there more than twice as often as in the inner zone.

2.6.4 Distribution of Angles Between Spheres Touching a Common Neighbour

Another way to look at the level of ordering in the system is by looking at the angle between the contact lines of two pebbles with their common neighbour (Jodrey and Torey, 1981). For the purpose of calculating these angles, we defined neighbours as being within $1.1d_{peb}$ of each other to account for uncertainties in pebble locations and size. For every pebble the angles of the contact lines with every pair of neighbours was calculated,

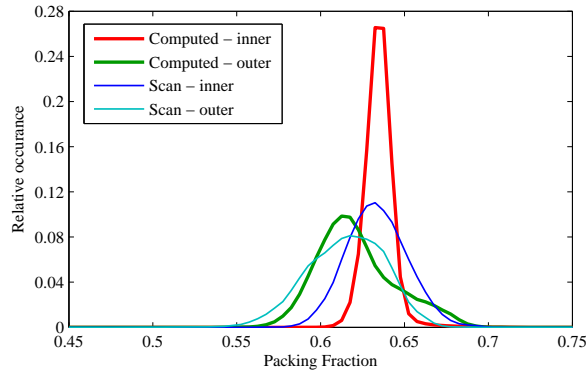


Figure 2.12: Probability density distribution of packing fractions of local pebble clusters in the inner (bulk) and outer zones (near-wall) of the computed and measured beds.

resulting in the probability distributions in Figure 2.11. Again the results were split up into an outer zone with pebbles $< 2.5d_{peb}$ from the wall and an inner zone with pebbles further away.

All four distributions show a large peak at 60 degrees representing three pebbles touching each other, with the scanned beds showing a wider peak due to uncertainties. As with the radial distribution function, a significant amount of angles < 60 degrees are observed for the scanned results, indicating overlaps, with the outer zone showing a larger number of smaller angles (< 55 degrees) than in the inner zone. The four distributions also show a smaller peak at 120 degrees corresponding to four pebbles lying in the same plane forming a diamond, in line with the peak in the radial distribution function at $\sqrt{3}d_{peb}$ in Figure 2.10. Again this peak is much wider and flatter for the scanned results. As before, there is hardly any difference between the inner and outer zone for the scanned bed, and they correspond well to the inner zone of the computed bed. However, the distribution of angles for the outer zone of the computed bed has significantly higher and sharper peaks, and also shows extra peaks at 90 and 180 degrees. These peaks correspond to a hexagonal closed packing, supporting our previous observations that near the wall the pebbles form more ordered planes of pebbles.

2.7 Distribution of Local Packing Fractions

In the previous section we looked at the microstructure in a pebble bed, investigating pebble-to-pebble ordering. In this section we investigate the probability distribution of packing fractions of small clusters of pebbles, as spatial variations in packing fraction might influence coolant flow and power density, and can be of importance for hotspot analysis. One could calculate the local packing fraction in a pebble bed by choosing a

point, drawing a sphere around that point and computing the packing fraction within this sphere. However, the calculated packing fraction will then greatly depend on how well the surface of the sphere would coincide with pebble material or void space, meaning that small shifts in the location of the central point or in the chosen size of the sphere can result in large differences in resulting packing fraction. As a result, in a pebble bed with an ordered stacking and a uniform packing fraction, this method would result in a non-uniform distribution of the local packing fraction. To avoid this, in our eyes, arbitrary effect on the calculated packing fraction, we used the Voronoï polyhedra from section 2.6.2.

To calculate the local packing fraction around a point in space, all pebbles with their centres closer than $2d_{peb}$ were selected, and the volumes of their Voronoï polyhedra were summed, which represents the volume occupied by the cluster of pebbles around the central point. From this the packing fraction was calculated by dividing the volumes occupied by the pebbles by the total volume of the Voronoï polyhedra. The size of these clusters was chosen to be big enough to influence flow and heat transfer, and small enough to capture local changes in packing density, with clusters containing around 45 pebbles. Using this method the local packing fraction was calculated at > 60 million points throughout the computed bed and at > 20 million points for the scanned bed. The resulting probability density distributions of the calculated cluster packing fractions are shown in Figure 2.12, where the results are split in cluster with centres $> 2.5d_{peb}$ away from the wall (inner zone), and an outer zone for cluster centres $\leq 2.5d_{peb}$ to the wall.

The distribution of packing fractions for the inner zone of the computed bed shows a very sharp peak around its average packing fraction of 0.634. However, not visible in the figure due to the low probability, is the occurrence of clusters with packing fractions of up to 0.7125, close to the maximum theoretical packing fraction of 0.740 for hexagonal close packing. The packing fractions for the inner zone of the scanned bed show a similar distribution, although broader due to the various uncertainties.

The outer zone of the computed bed, however, has a distinctly different distribution. The peak is much lower and at lower packing fraction, with lower packing fractions occurring due to the large void space around pebbles next to the wall. There is also a higher probability for areas with packing fractions above 0.65 than for the inner zone, which can be explained by an increased ordering close to the wall, resulting in an increase in areas with high local packing fraction, similar to the effect seen in Figure 2.9. The maximum packing fraction was slightly lower than for the inner zone, 0.7025, limited by the larger void space around pebbles next to the wall.

As before, agreement with results for the outer zone of the scanned bed is poor. Although that distribution also shows an increase of areas with lower packing fractions and a broader distribution, there is no increase but a decrease of areas with a high packing fraction. This could be caused by errors in the data acquisition and processing, or non-uniformity's in the pebbles causing more disorder in the near wall zone. Finally, there is the possibility that the larger curvature of the wall for the scanned bed, due to the smaller diameter,

makes it harder for the pebbles to form ordered sheets parallel to the wall.

2.8 Conclusions

In pebble bed reactors the fuel pebbles form a randomly stacked bed through which the coolant flows. To investigate in detail flow, heat transfer and neutronics and find possible causes for hotspots, a good understanding of the nature of randomly stacked beds is necessary and tools to computationally generate realistic pebble beds are needed, of which macroscopic and microscopic pebble-to-pebble stacking properties are validated with experimental data.

To this end the average packing fraction and radial and axial packing fraction profiles of randomly stacked beds containing 5400 acrylic pebbles with a uniform diameter of 12.7 mm were accurately measured with the PebBEx facility. In a second experiment computer aided 3D X-ray tomography was used to determine the pebble locations of a randomly stacked bed of 8900 glass pebbles with diameters ranging from 1.66 to 2.00 mm, from which various properties of the packing microstructure were evaluated and local variations in packing fraction inside the bed were determined. Results from both experiments were compared with those of computed beds, generated using a numerical method we developed based on removing overlaps.

The macroscopic properties of the computed bed matched those of the PebBEx measurements very well, having an almost identical average packing fraction, and radial and axial packing profiles similar to those of the experiment both in shape and in size of the fluctuations. The evaluated microscopic stacking properties from the 3D X-ray scan were the coordination number, distribution of Voronoï polyhedron packing fraction, radial distribution function, and the distribution of the angle between the contact lines of two spheres with a common neighbour. Properties were evaluated for both the bulk of the bed away from the wall, and the near wall region. For the bulk of the bed, there was a reasonably good match between the computed bed and experimental results from the 3D X-ray tomography, and an very good match with computational and experimental results from literature (Aste, 2005; Jodrey and Torey, 1981). In the near wall zone, the match was not so good. However, various properties of the experimentally determined pebble centre locations indicate the quality of the data is poor in the near wall region. First, the pebbles used for the scan were not very uniform in size. Also, significant overlap was observed between pebbles for the determined pebble centres, and the shape of the radial porosity profile near the wall matched poorly with accurate experimental results, both indications we were not successful in accurately determining the pebble locations near the wall.

Taken together, the results show the computational method generates randomly stacked beds with realistic macroscopic and microscopic stacking properties. Although there is no gravity in the computational method and it can not simulate pebble flow, the method creates beds without any overlaps with exactly touching pebbles, and is especially suitable to investigate in detail flow and heat transfer in small sections of a pebble bed. However,

to be more confident of the microscopic stacking properties near the wall better experimental 3D stacking data is needed. Preferably using a larger bed for more statistical data, but more importantly one with uniform pebble size, and an improved algorithm to better determine the pebble centre locations from the scan results, especially near the wall.

Results for both the radial and axial packing fraction profiles and the microscopic packing properties indicate the stacking structure of a randomly packed bed is different near the wall than in the bulk of the bed. Near the wall, the pebbles form semi-ordered layers with hexagonal-like stacking properties. As the layers lie parallel to the wall, the stacking near the wall is not isotropic. This indicates that to accurately describe flow and heat transfer, different models could be needed near the wall than in the bulk, and that flow and heat transfer might be anisotropic near a solid boundary.

Finally the experimental and computational results emphasise variations in the pebble stacking are inherent in randomly stacked beds. The location and size of peaks in the axial packing fraction profiles varied for two different beds, differences in filling procedures resulted in differences in average packing fraction, and the microscopic packing properties showed distributions of values over a wide range. The probability distributions of packing fractions of small clusters of around 45 pebbles showed strong variations in packing fractions exist inside a bed, both in the bulk and near the wall, which might significantly affect flow rates and could result in hotspots.

NEUTRONICS AND NEUTRON STREAMING

The content of this chapter was published in *Annals of Nuclear Energy* (Auwerda et al., 2010b).

3.1 Introduction

The pebble bed nuclear reactor is one of the main candidates for the next generation nuclear power plants. In pebble bed type HTRs, the fuel is contained within graphite pebbles, which form a randomly packed bed inside a graphite-walled cylindrical cavity. Due to the stochastic nature of this bed, the location of the individual pebbles is not well defined.

The pebble bed in such a reactor is commonly modelled as a homogeneous mixture of the pebble and coolant materials, with a uniform density throughout the core. Unfortunately, such a model does not include all effects due to the heterogeneity of the pebble bed, resulting in possible errors. Three of these effects are the density fluctuations in the pebble bed near the wall, neutron streaming through the void space between the pebbles, and variations in the Dancoff factor near the edge of the pebble bed.

Benenati and Brosilow (1962) showed that the radial void fraction profile of a pebble bed shows large fluctuations near the cylinder wall that dampen out at about 5 ball diameters from the wall. See Figure 2.3 for an example of the radial packing fraction profile in randomly stacked beds. These density fluctuations in the pebble bed can have a significant effect on the thermodynamics, for example due to wall-channelling of the coolant flow (Schertz and Bischoff, 1969) or peaks in the power distribution. Assuming a radial density profile from Benenati and Brosilow (1962), Terry and Ougouag (2003) found

that including the radial density fluctuations leads to a small increase in k_{eff} .

Another effect neglected when homogenising the pebble bed is neutron streaming. In a pebble bed, the space in between the pebbles is filled by helium. Neutrons can stream through this void space, increasing their migration length. The neglect of this in the homogenised model leads to an underestimation of neutron transport, resulting in less neutron leakage out of the pebble bed to the reflector and a lower k_{eff} of the system (Behrens, 1949).

To take into account the streaming effect in diffusion calculations, Lieberoth and Stojadinović (1980) proposed a streaming correction factor, increasing the diffusion coefficient to take into account the increased transport of neutrons. Wallerbos (1998) investigated the streaming effect for various core layouts of the LEU-HTR PROTEUS experimental facility at PSI, Switzerland (Williams et al., 2001). By comparing calculations using homogenised core models with calculations in which all pebbles were modelled individually, Wallerbos found significant reductions (1.5% - 3.3%) in k_{eff} due to neutron streaming. By similar means, Koberl and Seiler (2004) found reductions of 0.5% - 1.5% for various PROTEUS core loadings. Both investigated deterministic core loadings, with hexagonal close packed or columnar hexagonal (point-on-point) pebble stackings, in which the pebble locations were well defined. To our knowledge, the streaming effect in randomly packed pebble beds has not been quantified yet.

A third effect neglected in a homogenised pebble bed is related to the Dancoff factor. The Dancoff factor describes the probability of a neutron exiting a fuel kernel to enter another fuel kernel before interacting with other media and is an important parameter to calculate self-shielding parameters in the fuel. Near the edge of the pebble bed, pebbles are not completely surrounded by other pebbles, and a neutron exiting a fuel pebble will have a lower probability of entering a fuel kernel in another fuel pebble before scattering than in the centre of the bed. This results in a lower Dancoff factor near the edge of the pebble bed, leading to lower resonance self-shielding and higher absorption cross sections for the fuel. However, the magnitude of this effect on k_{eff} is yet unknown.

To quantify the errors arising in homogenised pebble bed models, this article investigates the effect of three phenomena in random pebble distributions on k_{eff} : Density fluctuations in the pebble bed, the neutron streaming effect, and a non-uniform Dancoff factor. The magnitude of the three effects was calculated for a simple model of an infinite cylinder, and for a model of the PROTEUS experimental facility (Mathews and Williams, 1995). For the cylindrical model 25 different pebble bed stackings were generated to investigate statistical effects of the random stacking.

For each pebble bed generated, three different core models were constructed: A homogeneous model, a zones model including the non-uniform packing fraction profile using homogenised zones, and a pebbles model with all pebbles modelled individually. For each core model, the k_{eff} was calculated using a Monte Carlo transport code. Additionally, the k_{eff} of the homogenised and zones models was calculated with a diffusion

code and a finite element based neutron transport code.

The effect of the density fluctuations on k_{eff} was calculated by comparing results for the homogeneous model with the zones model. The streaming effect was calculated from the difference between the zones model and the pebbles model. The calculated streaming effect was compared with the change in k_{eff} when applying the streaming correction factor to the diffusion calculations. The effect of changes in the Dancoff factor was investigated by calculating the change in k_{eff} when using a lower Dancoff factor in the outer layer of the pebble bed.

Section 3.2 describes the geometry models, as well as the code developed to generate the randomly stacked pebble beds. Section 3.3 explains the methods used to calculate the Dancoff factor and to generate the cross sections. The calculation of the streaming correction factor on the diffusion coefficient is detailed in Section 3.4. Results for the calculations on the infinite cylinder model are in Section 3.5. Section 3.6 gives the geometry model for the PROTEUS facility as well as the results of the calculations. The last section contains the conclusions on the importance to k_{eff} calculations of the density fluctuations, the streaming effect and changes in the Dancoff factor in randomly stacked pebble beds.

3.2 Geometry Model

A simple model of an infinite cylinder was used to study the effects of the pebble distribution on the multiplication factor in a controlled fashion. The model consisted of a cylindrical cavity with a radius of 62.71 cm containing the pebble bed, surrounded by a radial graphite reflector with an outer radius of 163.1 cm. The model was 100 cm high, and the top and bottom had reflective boundaries.

The pebble bed consisted of a 1:1 mixture of fuel and moderator pebbles with a diameter of 6 cm. The parameters of the model were taken from the LEU-HTR PROTEUS experiment (Williams, 1995). The moderator pebbles were made of pure graphite, while the fuel pebbles consisted of a central fuel zone of 2.35 cm radius in which the TRISO particles were dispersed in a graphite matrix, surrounded by a 0.65 cm thick outer graphite shell. Each fuel pebble contained 9394 TRISO particles. The TRISO particles consisted of a UO_2 fuel kernel (16.7% enriched) of 0.02510 cm radius, surrounded by a graphite buffer layer of 0.00915 cm thick, an inner pyrocarbon layer of 0.00399 cm, a silicium-carbon layer of 0.00353 cm, and an outer pyrocarbon layer of 0.00400 cm.

3.2.1 Generating the Pebble Bed

To generate the pebble coordinates, a numerical tool was developed based on the method described in (Mrafko, 1980). First N_{sph} points are chosen randomly within a reference space, representing the initial centers of the spheres, disregarding overlap. Next the sphere radius is set to its initial value $R_{sph,init}$ and this radius is increased in N steps to

the desired final radius. In each step, a numerical loop is run over all spheres. If a sphere intersects with a wall the overlap is removed by moving the sphere a distance equal to the overlap away in a direction perpendicular to the wall. If the sphere intersects with its nearest neighbour, both spheres are moved an equal distance apart along their line of intersection until they are touching. When moving the spheres, the creation of new overlaps is allowed. This is repeated until no overlaps remain. Then the pebble radius is increased, after which the overlaps are removed again in another cycle.

The code was validated by comparing average and radial packing fractions of pebble beds generated by the code with experimental measurements performed on a perspex pebble bed model. Characteristics of the generated pebble bed compared well with measurements (Auwerda et al., 2010a).

By using different random seeds to initialize the code, 25 different pebble beds were generated. Pebble beds were generated using 10,000 pebbles in a cylinder with a radius of 62.71 cm and a solid bottom, resulting in pebble beds approximately 155 cm high. To remove any influence in the pebble bed due to the bottom of the cylinder, the bottom 40 cm of the bed was discarded. The section of the generated beds between 40 and 140 cm high was used for the 100 cm high pebble bed in the infinite cylinder. At the top and bottom boundaries, partial pebbles were included if pebbles did not fit entirely within the boundaries, resulting in a uniform axial packing fraction profile for the 100 cm high pebble bed sections.

3.2.2 The Core Models

To investigate the different effects of a pebble bed stacking on the multiplication factor, three different core models were made for each of the 25 generated pebble beds.

1. The first model was a homogeneous core model in which the core region consisted of uniform homogenised pebble bed material, with a uniform density, using the average packing fraction of the pebble bed.
2. To investigate the effect of the density fluctuations in a pebble bed on k_{eff} , in the zones model the core was split up in 1 cm wide radial zones, except for the outermost zone, which was 0.71 cm wide. For each zone the average packing fraction of the pebble bed was calculated, and used to make appropriate homogenised cross sections. Thus, an axially homogenised core was constructed, including the density fluctuations in the pebble bed.
3. In the pebbles model, all pebbles were modelled individually, forming an exact model of a 100 cm high pebble bed.

See Figure 3.1 for a side view of the three geometry models. In Figure 3.2 the axially averaged packing fraction distribution as a function of radial position is plotted for the three

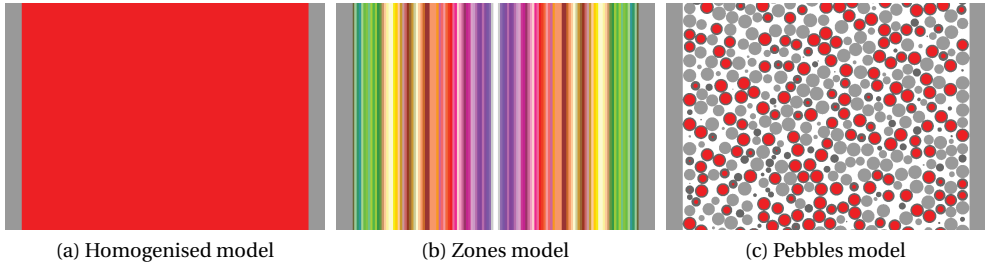


Figure 3.1: Side view of the core regions in the three core models. Left: homogenised model with one uniform fuel zone in the core (red), surrounded by the graphite reflector (grey). Middle: zones model consisting of 1 cm wide homogenised radial zones. Right: pebbles model, with all pebbles modelled separately; the red pebbles with dark grey border are the fuel pebbles with graphite shell, the light grey pebbles are the moderator pebbles. All three models used reflective upper and lower boundaries.

models. Clearly visible are the fluctuations in packing fraction near the wall, damping out at approximately 30 cm, or 5 pebble diameters from the wall, as was also observed by Benenati and Brosilow (1962). The rise in packing fraction near the centre of the cylinder is due to the random nature of the pebble bed and its finite height. Here the surface over which the packing fraction is calculated becomes small, crossing only a limited number of pebbles.

3.2.3 Implementing the Core Models in the Codes

Three different codes were used to perform k_{eff} calculations on the core models described above: the diffusion code DALTON, the finite element transport code PHANTOM, and the Monte Carlo transport code KENO-VI.

DALTON is a 3D diffusion code (Boer et al., 2009), which is able to perform calculations for steady state and transient modes. PHANTOM is a 3D finite element transport code, which solves the Boltzmann equations on an unstructured mesh using spherical harmonics for the angular discretisation. In DALTON and PHANTOM the k_{eff} for the homogeneous and zones model were calculated using a 1D cylindrical model with reflective upper and lower boundaries and a vacuum radial boundary condition.

The Monte Carlo transport code KENO-VI is part of the SCALE 5.1 code package (SCALE-5.1, 2006). In KENO a 100 cm high 3D cylindrical model with reflective upper and lower boundaries was used to represent the infinite cylinder. The homogeneous model was the simplest model and consists of only two zones: an inner cylinder of 62.71 cm radius containing the homogenised pebble bed material, surrounded by a zone from 62.71 cm to 163.1 cm containing the reflector graphite. In the zones model the core region was

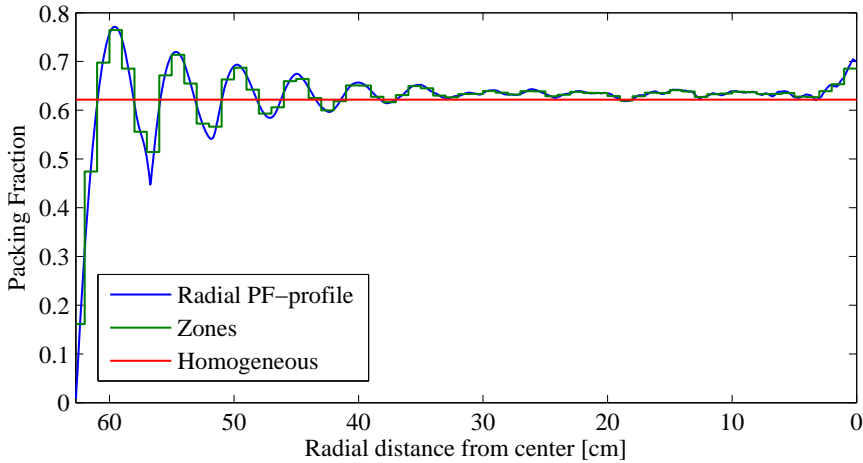


Figure 3.2: Radial packing fraction profile of a numerically generated pebble bed (continuous line) together with the corresponding PF-profile for the zones model (stairs plot) and the homogeneous model (straight line).

split up into 63 annular zones. The material in each zone was a homogeneous mixture of fuel and moderator pebbles and coolant, according to the average pebble bed packing fraction in that zone, see Figure 3.2.

For the pebbles model, each individual pebble was included separately in the KENO model. This could not be done by making separate geometric UNITS for the fuel and moderator pebbles and then inserting them at their appropriate coordinates in the pebble bed region using HOLES. This would result in an extremely complex material region containing the coolant surrounding the pebbles, with a large number of bounding surfaces (one for each pebble). To keep the material regions of manageable size and complexity, the cylinder was divided into 10 by 10 by 10 cm cells, using a cubic lattice. For the current cylindrical model, this resulted in a lattice of 13 by 13 by 10 cells, for a total of 1690 array cells. For each array cell, a separate geometry UNIT was defined in KENO. In this UNIT all pebbles, or parts of pebbles, that were inside this $10 \times 10 \times 10$ cm block of the pebble bed were modelled. See Figure 3.3 for a sample UNIT geometry. All UNITS put together filled up the array, forming the complete pebble bed. Finally, the array was inserted in the core cavity, bounded by the reflector wall.

3.3 Cross Section Processing

Resonance corrected macroscopic cross sections were generated with the SCALE 5.1 code package (SCALE-5.1, 2006) based on methods detailed by Wallerbos et al. (1998), using



Figure 3.3: Sample UNIT geometry consisting of a 10 by 10 by 10 cm cutout of the actual pebble bed, representing one array cell in the KENO model. Light blue: moderator pebbles; grey: fuel region; dark blue: graphite shell of fuel pebble.

the 238-group ENDF/B-VI library. The library contained Bondarenko factors for use with the BONAMI module to perform resonance self-shielding in the unresolved resonance range, according to the Bondarenko method. To perform resonance self-shielding in the resolved range continuous-energy cross-section data was available for use with the CENTRM and PMC modules.

Atom densities for the various materials were taken from the system component description (Mathews and Williams, 1995) of the PROTEUS benchmark. The boron concentration in the reflector graphite, representing the various impurities in the graphite, was enlarged to increase the 2200 m/s effective absorption cross section of the reflector graphite from 4.09 mbarn to 4.47 mbarn, as was recommended in recent studies (Chawla et al., 2002).

3.3.1 Dancoff Factor Calculation

The double heterogeneity in the pebble bed was taken into account by using a Dancoff factor C . The Dancoff factor describes the probability of a neutron exiting a fuel lump to enter another fuel lump before interacting with other media and is an important

parameter to calculate self-shielded cross-sections of the fuel. For pebble beds, the Dancoff factor consists of two parts. The first part, the intra-pebble Dancoff factor C_{intra} , is the probability of a neutron leaving a fuel kernel to reach another fuel kernel in the same fuel pebble without collision. The second part, the inter-pebble Dancoff factor C_{inter} , is the probability that a neutron leaves the first pebble without collision, and reaches a fuel kernel in another fuel pebble.

The Dancoff factor was calculated according to the method of Bende et al. (1999). For a 1:1 mixture of fuel and moderator pebbles this resulted in $C_{intra} = 0.2832$ and $C_{inter} = 0.0253$, giving a total Dancoff factor of $C = C_{intra} + C_{inter} = 0.3085$.

3.3.2 Homogenisation and Collapsing

Macroscopic homogenised cross sections were created for the pebble fuel zone by processing a TRISO unit cell with the SCALE 5.1 CSASI driver, using the LATTICECELL geometry option with spherical triangular pitch and white boundary conditions. The unit cell consisted of the fuel kernel and its boundary layers, surrounded by a graphite matrix, as defined in Mathews and Williams (1995). The double heterogeneity of the fuel kernels was taken into account by supplying a Dancoff factor. Resonance treatment for the unresolved resonances was performed by BONAMI, and for the resolved resonances by CENTRM and PMC.

To generate macroscopic resonance corrected cross sections for the outer pebble shell, moderator pebble and coolant materials, in a similar way an infinite pebble lattice was processed with CSASI. The pebble unit cell consisted of a homogenised fuel zone of 2.35 cm radius, surrounded by the graphite shell of 0.65 cm thick. The third layer contained the moderator pebble material and the final layer the coolant. The radius of the last two layers were chosen such that the volume fractions of the pebble bed were preserved, and depended on the moderator to fuel pebble ratio and the packing fraction.

Graphite reflector macroscopic cross sections were generated using the MULTIREGION cylindrical geometry option with two zones. The first zone with a radius of 62.71 cm was filled with homogenised pebble bed material, and was surrounded by the graphite reflector material with an outer radius of 163.1 cm.

To generate homogenised pebble bed cross sections for the homogenised and zones core calculations these steps were followed by a 1D transport calculation of a pebble geometry using the XSDRNPM routine. The geometry was similar to that used in the pebble cell CSASI run, using the macroscopic resonance corrected cross sections generated in the CSASI runs.

Finally the 238 group libraries thus created were collapsed to 50- and 20-group libraries using XSDRNPM for use in the DALTON and PHANTOM calculations. A fine mesh of regions was used over which collapsed cross sections were created, with regions in the core being 1 cm wide, corresponding to the zones model. The reflector was split up into

12 material regions, with regions having a width of 5 to 10 cm, with smaller regions closer to the core.

3.4 Streaming Correction on Cross Sections

In pebble beds, neutrons can stream through the void space in between the pebbles, resulting in an increase of neutron transport. When homogenising the pebble bed, the neutron mean-free-path \bar{l} is calculated correctly, but neutron streaming is neglected. As a result, the neutron mean-square-free-path \bar{l}^2 is underestimated.

To take into account the increased transport of neutrons due to neutron streaming in diffusion calculations, Lieberoth and Stojadinović (1980) proposed a correction factor $C_{str,g}$ on the diffusion constant D_g , increasing the diffusion constant according to

$$C_{str,g} = \frac{D_{corr,g}}{D_g} = \frac{\bar{l}_g^2}{\bar{l}_{Hg}^2} \quad (3.1)$$

where $D_{corr,g}$ is the corrected diffusion coefficient of the pebble bed for energy group g .

Using measurements of the coordinates of an experimental stacking of 3024 metal spheres, Lieberoth and Stojadinović (1980) determined the first two mean moments \bar{h} and \bar{h}^2 of the passage lengths in the holes of a pebble bed. With this data and under the assumption that no correlation exists between the passage lengths in the holes and in the balls, a formula for the mean-square-free-path \bar{l}^2 in a pebble bed was derived. Assuming near-isotropic scattering they derived $D_{corr,g}/D_g = \bar{l}_g^2/\bar{l}_{Hg}^2$, where \bar{l}_H^2 is the neutron mean-square-free-path for the uncorrected homogenized case. From this the streaming correction factor $C_{str,g}$ on the diffusion coefficient D_g was derived as a function of the total cross section Σ_t of the solid material in the pebble bed, the pebble radius R , and the packing fraction PF through $\phi = \frac{1}{PF} - 1$:

$$C_{str} = 1 + \frac{\phi \Sigma_t R}{(1 + \phi)^2} \left[\frac{2}{3} Q - 1 + \frac{4}{3} \Sigma_t R \left(\frac{2 \Sigma_t^2 R^2}{2 \Sigma_t^2 R^2 - 1 + (1 + 2 \Sigma_t R) e^{-2 \Sigma_t R}} - 1 \right) \right] \quad (3.2)$$

where $Q = \bar{h}^2/(\bar{h})^2$ was determined as a function of ϕ using the coordinates of the experimental stacking and a cubic and tetrahedral stacking:

$$Q = 1.956 + \frac{1}{260\phi^2} \quad (3.3)$$

As explained in Williams et al. (2001) this correction factor can also be applied to transport theory by using the following relation for the diffusion coefficient

$$D_g = \frac{1}{3(\Sigma_{t,g} - (\bar{\mu}\Sigma_s)_g)} \quad (3.4)$$

where

$$\bar{\mu}\Sigma_{s,g} = \frac{1}{3} \sum_{g'} \Sigma_{l=1,g \rightarrow g'} \quad (3.5)$$

is the sum over all outgoing groups of the P_1 scattering matrix for energy group g . By inserting equation 3.4 in 3.1 and rearranging one can get a correction factor for $\bar{\mu}\Sigma_{s,g}$

$$\frac{(\bar{\mu}\Sigma_{s,g})_{corr}}{\bar{\mu}\Sigma_{s,g}} = \frac{\Sigma_{t,g}}{\bar{\mu}\Sigma_{s,g}} - \frac{\Sigma_{t,g}}{\bar{\mu}\Sigma_{s,g} C_{str,g}} + \frac{1}{C_{str,g}} \quad (3.6)$$

3.5 Results on the Infinite Cylinder

25 different randomly stacked pebble beds were generated, each using a different random seed. Each bed has a slightly different average packing fraction, with an average over all beds of 0.6227 and a maximum deviation from this average of 0.20%. For each of these pebble beds, homogenised cross sections were generated, as well as cross sections per density zones.

Calculations were performed with the KENO-VI MC code, the diffusion code DALTON, and the finite element transport code PHANTOM. KENO used 200 active cycles with 20000 neutrons per cycle and 238 energy groups in all calculations, resulting in a standard deviation in the calculated k_{eff} of ~ 40 pcm for the individual KENO calculations. Additionally, 50-group KENO calculations using the homogeneous and zones model were performed. The DALTON and PHANTOM calculations used a 1D cylindrical geometry with 50- and 20-group libraries. In DALTON a spatial mesh of 3000 nodes was used and in PHANTOM the geometry was split up into 435 triangular elements with P_7 expansion of the flux moments and a P_5 scattering expansion.

3.5.1 Homogenised Core

The k_{eff} of the infinite cylinder was calculated for each of the 25 pebble beds, using the homogenised core cross section. Results of k_{eff} versus the average packing fraction are plotted in Figure 3.4. Table 3.1 lists the average k_{eff} over the 25 pebble beds for each code and the average difference Δ_{KENO} between the KENO 238-group results and the deterministic codes. The standard deviation σ of Δ_{KENO} was also calculated, and was found to be 46 pcm for the deterministic codes, corresponding to the standard deviation of the individual KENO calculations. The uncertainty of the reported Δ_{KENO} values was found to be 9 pcm. For the KENO 50-group calculations, $\sigma = 63$ and $\sigma_{\bar{x}} = 13$.

As can be seen in Figure 3.4 and Table 3.1, the k_{eff} for the deterministic calculations show a slight overestimation when compared to the 238-group Monte Carlo calculations. The 50-group calculations show good agreement with the KENO results, especially for the transport (PHANTOM) calculations. The difference between the KENO and PHANTOM 50-group calculations is negligible, and their difference with the KENO 238-group calculations is within two $\sigma_{\bar{x}}$. From the 20-group results it can be concluded that diffusion

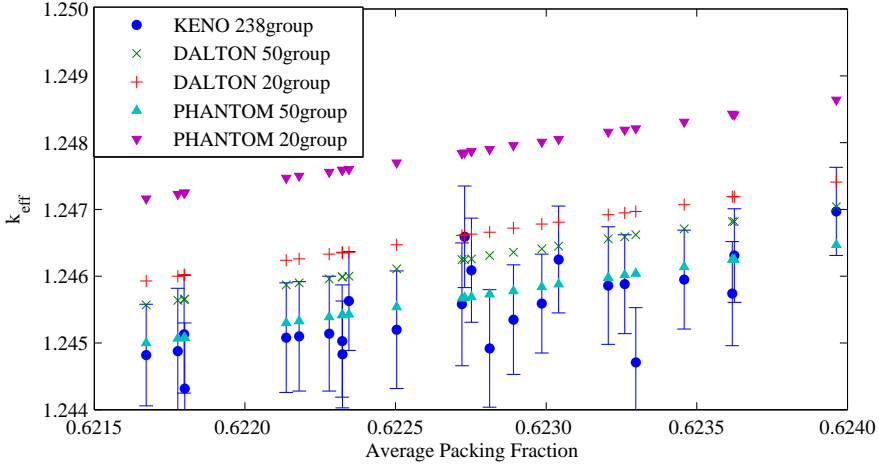


Figure 3.4: Calculated k_{eff} values of the homogenised core model versus average packing fraction for all 25 pebble bed realization. KENO results include 2σ error bars.

Table 3.1: Average k_{eff} of the homogenised calculations and the difference Δ_{KENO} between the deterministic results and KENO-238gr. For the listed Δ_{KENO} values, the standard deviation $\sigma = 46$ pcm and the uncertainty $\sigma_{\bar{x}} = 9$ pcm for all cases, except for KENO 50gr. Here $\sigma = 63$ pcm and $\sigma_{\bar{x}} = 13$

Calculation	k_{eff}	Δ_{KENO}
KENO 238gr	1.24548	-
KENO 50gr	1.24571	23
DALTON 50gr	1.24623	75
DALTON 20gr	1.24659	112
PHANTOM 50gr	1.24566	18
PHANTOM 20gr	1.24783	235

calculations are more forgiving concerning the number of groups than transport calculations. The standard deviation of 46 pcm for the KENO result of the average k_{eff} agrees well with the standard deviation of the individual KENO calculations of ~ 40 pcm, showing that the difference between KENO and the deterministic codes is independent of the small deviations in the pebble bed packing fraction.

3.5.2 Non-Uniform Density Distribution

To investigate the effect of the packing fraction fluctuations in the pebble beds on k_{eff} , a zones model of the core was created for each of the 25 pebble beds, and the k_{eff} of each

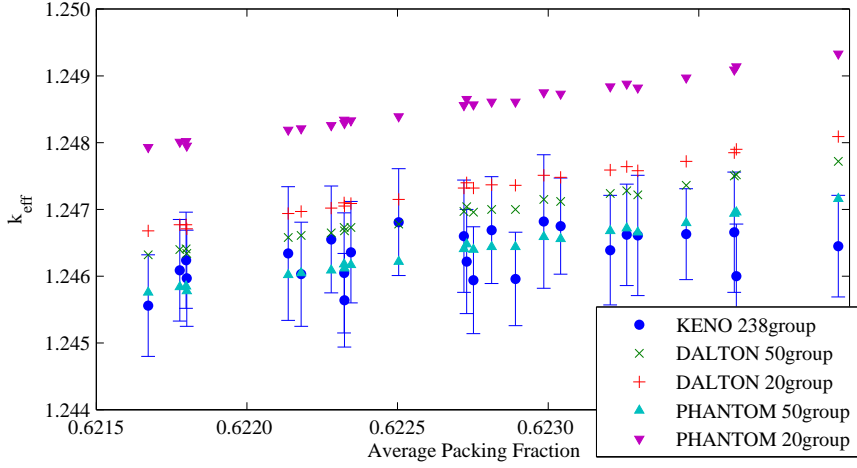


Figure 3.5: Calculated k_{eff} values versus the average packing fraction for each of the 25 pebble beds, using the zones core model. KENO results include 2σ error bars.

Table 3.2: Average difference $\Delta_{dens} = k_{eff,zones} - k_{eff,homo}$ [in pcm] in k_{eff} due to density variation in the pebble bed, calculated from results for the homogeneous and zones model. Also given is the standard deviation σ and uncertainty $\sigma_{\bar{x}}$ in the calculated Δ_{dens} values.

Calculation	Δ_{dens}	σ	$\sigma_{\bar{x}}$
KENO 238gr	84	65	13
KENO 50gr	66	62	12
DALTON 50gr	70	4	1
DALTON 20gr	70	4	1
PHANTOM 50gr	71	4	1
PHANTOM 20gr	71	4	1

bed was calculated using KENO, DALTON and PHANTOM, as before. The calculated k_{eff} values are plotted versus the pebble bed packing fractions in Figure 3.5.

Results for the zones model were compared with results for the homogeneous core for each bed and code. The average difference Δ_{dens} over all pebble beds between the k_{eff} using the zones model and the homogeneous core model is given in Table 3.2 for each code. Also given is the standard deviation σ and the uncertainty $\sigma_{\bar{x}}$ in the Δ_{dens} value.

Figures 3.4 and 3.5 show very similar results for the KENO and deterministic results. For the zones model, differences between KENO 238-group and the deterministic codes are for each code on average 13 pcm smaller than reported in Table 3.1, with similar σ and $\sigma_{\bar{x}}$ values. For the zones model, the average k_{eff} for the KENO and PHANTOM 50-group

calculations are exactly the same, and their difference with the KENO 238-group results is 5 pcm. Together with the excellent agreement for the homogeneous model, this shows the negligible difference between KENO 238-group and KENO 50-group calculations. In the rest of this paper, no further KENO 50-group calculations are done.

Taking into account the fluctuations in packing fraction in the zones model causes a small increase $\Delta_{dens} = 70$ pcm in k_{eff} compared to the homogeneous model. This increase comes from the low packing fraction close to the wall, resulting in a slightly more compact core in the zones case, with a higher PF in the central part of the core. Thus we get a more compact core and less leakage. The low value of Δ_{dens} agrees well with results from Terry and Ougouag (2003), supporting their conclusion that the fluctuations in the radial packing fraction due to the reflector wall are not important in neutronics calculations of pebble bed reactors.

From the standard deviations and uncertainties in the Δ_{dens} it can be concluded that the positive effect on k_{eff} does not depend on the pebble bed realization, even in a small bed such as this. The comparatively large standard deviation of 65 pcm in the KENO results for Δ_{dens} can be attributed to the uncertainty in the individual KENO calculations.

3.5.3 Neutron Streaming Effect

The effect of neutron streaming in between the pebbles on k_{eff} was investigated using calculations of the 25 pebble beds on exact core models of the pebble bed, in which each pebble was modelled individually. As the pebbles model also included the non-uniform density profile in the pebble bed, the results were compared with the zones model to get the pure streaming effect on k_{eff} , such that $\Delta_{streaming} = k_{eff,pebbles} - k_{eff,zones}$.

DALTON calculations were performed with corrected diffusion coefficients according to equation 3.2, using the zones core model. In the same manner, corrected cross sections were prepared with equation 3.6 and used with KENO and PHANTOM. Results were compared with the uncorrected calculations from the previous section to get the streaming correction on k_{eff} , $\Delta_{streaming} = k_{eff,corr} - k_{eff,zones}$, according to the correction factor.

Results for the KENO pebbles model and KENO $(\bar{\mu}\Sigma)_{corr}$ using the zones model are plotted in Figure 3.6 together with the uncorrected results for comparison. Also plotted are the DALTON results for the uncorrected and corrected diffusion coefficient. Table 3.3 lists the streaming effect $\Delta_{streaming}$ on k_{eff} according to the various methods, and its standard deviation σ and uncertainty $\sigma_{\bar{x}}$.

The correction factor to the P_1 scattering matrix given in equation 3.6 can result in very large values for the correction factor, especially for regions with a low packing fraction. This results in the values of the first moment in the scattering matrix to be larger than the zero moment, and can lead to inconsistent cross section sets. As a result PHANTOM calculations using the zones model together with the corrected cross sections did not converge, so $\Delta_{streaming}$ in PHANTOM was calculated using the homogeneous core model. KENO

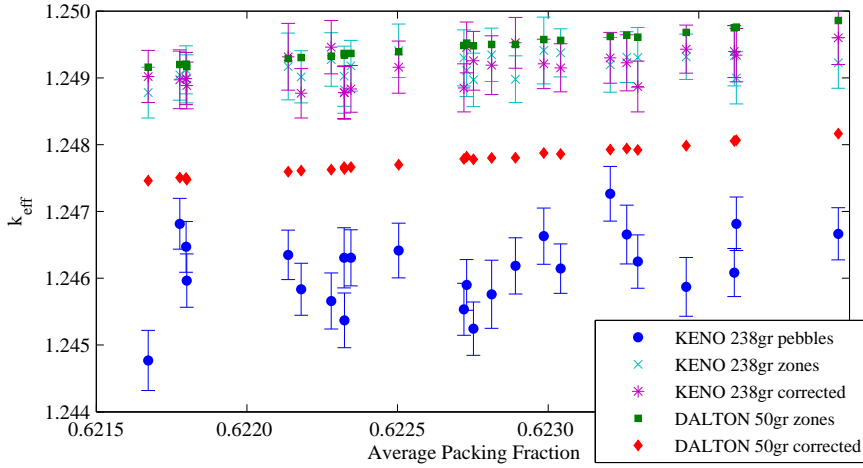


Figure 3.6: Results for k_{eff} calculations using the pebbles model and the zones model in KENO and the zones model in DALTON. Also given are results for calculations using the corrected cross sections (according to Equations 3.2 and 3.6) together with the zones model for KENO and DALTON. KENO results include 2σ error bars.

Table 3.3: Streaming effect $\Delta_{streaming}$ [in pcm] on k_{eff} averaged over the 25 pebble beds. The pebbles entry gives the streaming effect $\Delta_{streaming} = k_{eff,pebbles} - k_{eff,zones}$ calculated from the difference of the exact pebbles model and the zones model. The $\Delta_{streaming}$ for the $corr$ entries give the change in k_{eff} when using the correction factors on the cross sections given in section 3.4 with the zones model compared to using the uncorrected cross sections, resulting in $\Delta_{streaming} = k_{eff,corr} - k_{eff,uncorr}$.

Calculation	$\Delta_{streaming}$	σ	$\sigma_{\bar{x}}$
KENO 238gr pebbles	-606	104	21
KENO 238gr $(\bar{\mu}\Sigma)_{corr}$	-2	54	11
DALTON 50gr D_{corr}	-340	1	0
DALTON 20gr D_{corr}	-347	1	0
PHANTOM 50gr $(\bar{\mu}\Sigma)_{corr}$	-346	1	0
PHANTOM 20gr $(\bar{\mu}\Sigma)_{corr}$	-360	1	0

internally removes inconsistencies in the moments of the scattering matrix. Thus, KENO had no problems using the corrected cross section set, but it made large adjustments to the scattering matrix.

As can be seen in Figure 3.6, modelling the pebbles exactly causes a significant drop in k_{eff} compared to the zones core model. For the 25 pebble beds the average difference

$\Delta_{streaming} = -606$ pcm, caused by the added leakage of neutrons out of the pebble bed to the graphite reflector due to streaming through the void spaces in between the pebbles. Comparing the plots of the KENO pebbles and KENO zones model in Figure 3.6 one can notice the large fluctuation in k_{eff} for the pebbles model, which result in a large standard deviation $\sigma = 104$ in $\Delta_{streaming}$. This shows that local variations between one randomly stacked pebble bed and another due to the random nature of the pebble bed can influence the magnitude of the streaming effects in a pebble bed, even though the beds have similar average packing fraction.

Looking at the plots for the DALTON diffusion calculations in Figure 3.6 and the $\Delta_{streaming}$ results for the deterministic codes in Table 3.3, it is clear that the correction factor on the diffusion equation underestimates the streaming effect for this geometry. As can be seen from the results for KENO $(\bar{\mu}\Sigma)_{corr}$, the correction factor as defined in equation 3.6 is not applicable to KENO calculations due to the adjustments KENO makes on the cross sections. Applying equation 3.6 to PHANTOM gives a similar correction on k_{eff} as D_{corr} for DALTON.

3.5.4 Effect of Non-Uniform Dancoff Factor

In a pebble bed reactor, the Dancoff factor is an important parameter to generate correct self-shielded cross sections for the fuel pebbles. Near the boundaries of the pebble bed, neutrons exiting a fuel pebble will have a lower probability of reentering a different fuel pebble before interacting with other media, due to the fact that there are less fuel pebbles around. The pebbles are no longer surrounded on all sides by other fuel pebbles. To estimate the magnitude of this effect, it was assumed that the probability of a neutron to enter a different fuel pebble was zero in the outer layer of the pebble bed for the purpose of calculating the Dancoff factor. Here the inter-pebble Dancoff factor C_{inter} was set to be zero. Thus, only the intra-pebble Dancoff factor C_{intra} of the pebble was used, and in the outer zone of the pebble bed the Dancoff factor $C = C_{intra} = 0.2832$.

In the pebbles model, cross sections generated with the lower Dancoff factor were used for pebbles with their centre within one pebble diameter from the wall. In the homogeneous and zones core models, cross sections generated with the lower Dancoff factor were used for the part of the bed within 6 cm of the reflector wall. Calculations were performed for each of the 25 pebble beds using KENO, DALTON and PHANTOM and using all three core models (homogeneous, zones, and pebbles). The change Δ_{Dan} in k_{eff} compared to using a uniform Dancoff was calculated and given in Table 3.4 in pcm, together with its standard deviation σ and uncertainty $\sigma_{\bar{x}}$.

As can be seen from the values of Δ_{Dan} , the effect of possible variations of the Dancoff factor in pebble bed reactors is negligible. For the deterministic codes, the resulting difference in k_{eff} was less than 1 pcm in all cases. For the KENO calculations Δ_{Dan} is larger, but is not significant compared to the reported uncertainty, and can be attributed to the uncertainty of on average 40 pcm in the KENO calculations themselves.

Table 3.4: Average difference Δ_{Dan} [in pcm] for all 25 pebble beds between k_{eff} calculations using $C_{inter} = 0$ in the outer 6 cm of the core and when using a uniform Dancoff factor. Also given is the standard deviation σ and uncertainty $\sigma_{\bar{x}}$ in the Δ_{dens} values.

Calculation	Δ_{Dan}	σ	$\sigma_{\bar{x}}$
KENO homogeneous	-15	68	14
KENO zones	-3	50	10
KENO pebbles	-25	74	15
DALTON all	<1	<1	<1
PHANTOM all	<1	<1	<1

The major contribution to the Dancoff factor is from the intra-pebble contribution, thus the change in Dancoff factor is only small when setting $C_{inter} = 0$. Since the effect of the Dancoff factor on k_{eff} is only secondary through the self-shielding calculations, small changes in the Dancoff factor in a small portion of the volume of the core have no significant effect on k_{eff} and can be neglected.

3.6 Application to HTR-PROTEUS Core 4.2

The PROTEUS facility at the Paul Scherrer Institute in Villigen, Switzerland is a zero power critical facility. From July 1992 to July 1996 it was used to investigate properties of pebble bed LEU-HTR systems (Low Enriched Uranium - High Temperature Reactor). The PROTEUS facility consisted of a cylinder of graphite, 330.4 cm in height and 326.2 cm in diameter. A 22-sided irregular polygonal central cavity, with base 78.0 cm above the bottom of the graphite reflector, having a flat-to-flat diameter of 125.0 cm, contained the fuel and moderator pebbles. The removable upper axial reflector assembly consisted of a graphite cylinder of height 78.0 cm contained within an aluminium encasing. A detailed description of the layout of the PROTEUS facility is given in Mathews and Williams (1995).

During the LEU-HTR PROTEUS experiment, for several pebble stackings (hexagonal close packed, columnar hexagonal, and stochastic) critical cores were loaded and measurements were performed (Williams, 1995). In this paper core layout 4.2 is studied, which had a stochastic pebble stacking 152 cm high containing 9880 pebbles with a fuel to moderator pebble ratio of 1:1. 21 filler pieces were put at the bottom of the core, creating a funnel with an inner radius of 25 cm and a 10-degrees-slope upwards towards the wall. The reported criticality for this core layout is 1.0129 ± 0.001 , including reactivity corrections for simplifications in the core model (Williams, 1995).

3.6.1 PROTEUS Core Model

As detailed reactivity corrections to the critical loading are given in the HTR-PROTEUS technical documentation (Williams, 1995) for control rods, air gaps, instrumentation,

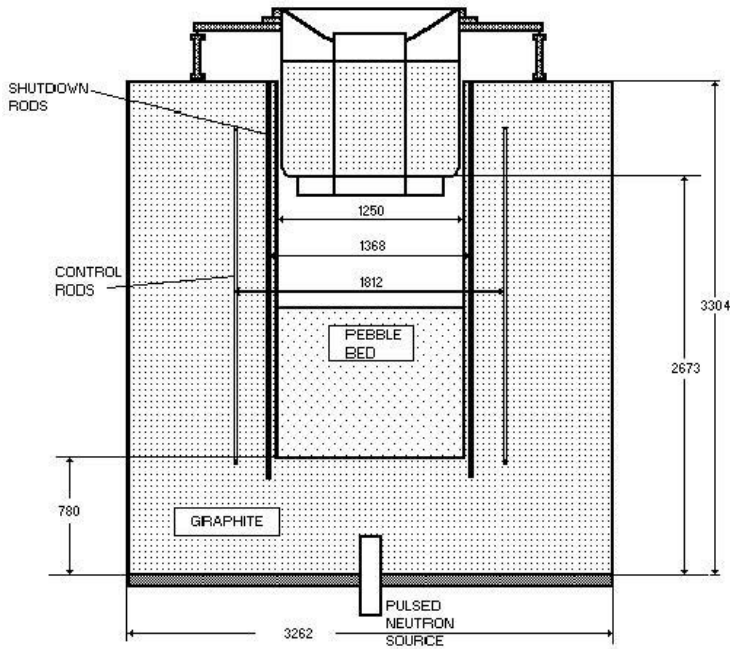


Figure 3.7: Schematic side view of the HTR-PROTEUS facility.

etc., a simple model for the graphite reflector of a solid graphite cylinder with a diameter of 326.2 cm and a height of 330.4 cm was used. The inner cavity bottom is located 78 cm above the base of the reflector and the 22-sided inner polygonal walls were approximated by a cylinder of radius 62.71 cm, keeping the core volume constant. The removable upper reflector and aluminium structure supporting were modelled as suggested in the system component description (Mathews and Williams, 1995). Coolant channels in the upper and lower reflector were ignored as their reactivity corrections were given.

Using the code described in section 3.2.1, a pebble bed was generated consisting of 9880 pebbles with a flat upper surface, taking into account the cone shape at the bottom. The top of the pebble bed, defined as the top of the highest pebble, was at 151.94 cm, corresponding remarkably well with the reported 152 cm in the Proteus experiment. Similar as for the infinite cylinder, three core models were made using the pebble bed data. The first is the homogeneous core with a uniform packing fraction of 0.6078. In the zones model the pebble bed was split up into 44 axial and 31 radial zones, and for each zone the packing fraction was calculated. For a distribution of the zones see the right side of Figure 3.8. The pebbles model is an exact core model in which each pebble was modelled individually.

The packing fraction in each axial zone is plotted in Figure 3.9 together with the pack-

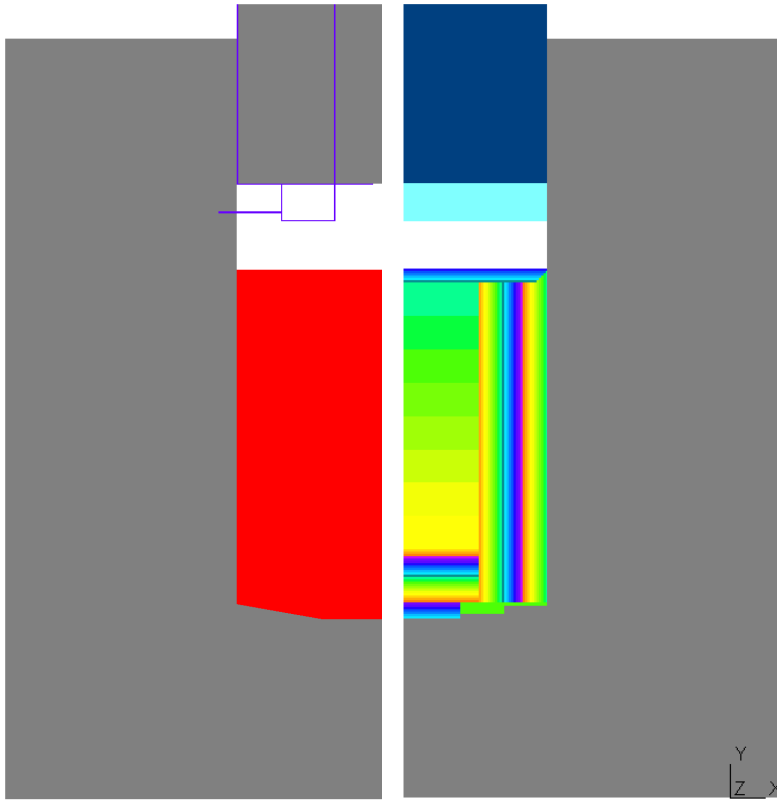


Figure 3.8: PROTEUS model as implemented in KENO with a homogenised core (left) and in DALTON and PHANTOM (right) with the core divided into zones.

ing fraction profile in those zones for the pebbles model and the homogeneous packing fraction. The influence of the bottom is clearly visible in the fluctuations in the packing fraction near the bottom. In the middle part the PF profile shows relatively large fluctuations due to the small cylinder over which is sampled (the axial zones are only 33 cm wide). As the top of the pebble bed is not bounded by a wall, there are no fluctuations in PF near the top, and the PF drops to zero over a distance of 6 cm, corresponding to one pebble diameter.

In DALTON and PHANTOM a slightly simpler geometric model was used than in KENO. Although PHANTOM is capable of modelling the more complex geometry used in KENO, for consistency the same model as for DALTON was used. The aluminium structure in and below the upper reflector was split up into two parts. The aluminium below the top

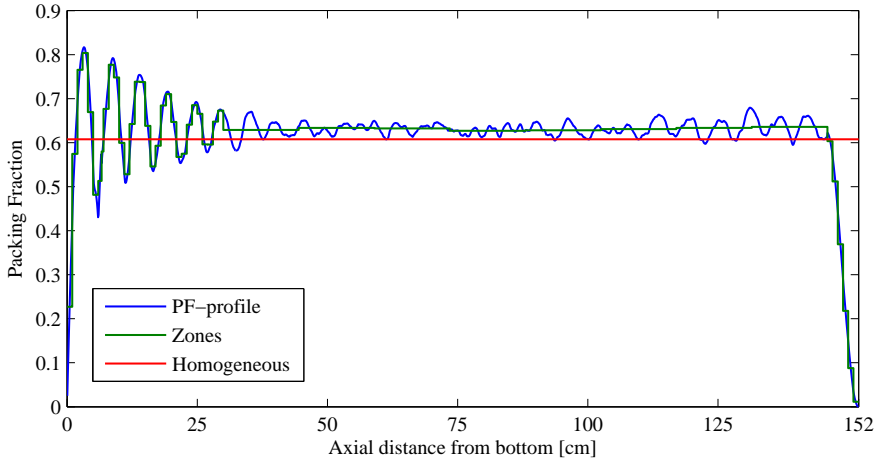


Figure 3.9: Axial packing fraction in the axial zones for the PROTEUS core model. The axial packing fraction is given as modelled in each of the three different core models. Continuous line: PF profile in the pebbles model; stairs function: zones model; horizontal line: homogeneous model.

reflector was volume averaged with the top part of the air in the upper cavity, and the aluminium inside the top reflector was mixed with the top reflector graphite, creating two homogenised material zones. The cone shape at the bottom could not be implemented in DALTON because of the slanted surface, so it was approximated by a stair-like geometry. See Figure 3.8 for a comparison of the models used in KENO and in DALTON.

3.6.2 PROTEUS Results

The k_{eff} for the homogeneous, zones and pebbles models was calculated with the KENO-VI Monte Carlo code using 238 energy groups. As before, each calculations consists of 240 cycles of 20000 particles each, of which the first 40 cycles were discarded. The k_{eff} of the homogeneous and zones models were also calculated with the DALTON diffusion code and the PHANTOM transport code, both using 50 energy groups and an r-z geometry. PHANTOM used a grid of 16491 triangular elements with P_7 expansion of the flux and a P_5 scattering expansion, and DALTON used a geometry model of 341 by 582 cells.

The diffusion coefficient of the coolant cavity above the pebble bed was calculated as recommended by Gerwin and Scherer (1987). The diffusion calculations did not include directional dependence of the diffusion coefficient, so could not include both the radial and axial diffusion coefficient. The Gerwin and Scherer diffusion coefficient value for the axial direction was used for the cavity in order to model the neutron streaming between core and upper axial reflector properly. As the cavities height is smaller than its diameter,

Table 3.5: PROTEUS core 4.2 k_{eff} for a homogenized core with uniform density (Homo) and when including the density variations in axial and radial zones (Zones), and their difference Δ_{dens} [in pcm]. Also given is the experimental result from Williams (1995).

Code	Homo	Zones	Δ_{dens}
Experiment	1.0129		
KENO 238gr	1.02197	1.02846	649
DALTON 50gr	1.02190	1.02577	387
PHANTOM 50gr	1.02247	1.02790	543

leakage in the axial direction is expected to be more important than in the radial direction.

Effect of Density Fluctuations on k_{eff}

The k_{eff} calculated for both the homogeneous and the zones core model are given in Table 3.5 together with their difference Δ_{dens} . Also given is the experimental result reported in Williams (1995). The standard deviation in the KENO calculations for the homogeneous and zones models are $\sigma_{homo} = 36$ and $\sigma_{zones} = 43$ pcm respectively, resulting in an uncertainty in Δ_{dens} of $\sigma_{\Delta} = 56$ pcm.

Remarkable is the large value of Δ_{dens} , especially when compared to the value for the infinite cylinder (Table 3.2). This is due to the low packing fraction near the top of the pebble bed. Here the packing fraction gradually drops to zero over a distance of 6 cm, without being compensated by a large peak in packing fraction close by as is the case for the radial profile, see Figures 3.2 and 3.9. To compensate for the low packing fraction near the top, the bulk of the pebble bed has a significantly lower packing fraction in the homogeneous case than in the zones case, resulting in a significantly higher k_{eff} .

This was confirmed by a KENO calculation using a homogenised core model and a pebble bed height of 149 cm, resulting in an average packing fraction of 0.6203. The calculated k_{eff} for this model was 1.02702 ± 41 pcm. Comparing this value with the result for the zones model results in a Δ_{dens} due to density fluctuations at the wall and bottom of the pebble bed of 144 pcm, in good agreement with values found for the infinite cylinder in section 3.5.2.

PHANTOM shows a lower Δ_{dens} than KENO, which can be explained by the slight difference in the geometry model. Calculations with KENO using the same geometry model as PHANTOM gave for the homogeneous model $k_{eff} = 1.02172 \pm 0.00046$ and for the zones model $k_{eff} = 1.02753 \pm 0.00041$, resulting in $\Delta_{dens} = 581 \pm 62$ pcm. Another cause of the difference can be the statistical uncertainties in the KENO calculations. Although the difference with the KENO results for the homogeneous and zones calculations as well as the Δ_{dens} value are larger than one σ , they are smaller than two σ , so they still fall within a 95% confidence interval of the KENO results.

Table 3.6: k_{eff} results for exact (pebbles) calculation and calculations using the zones model together with the streaming correction on cross sections from equations 3.2 and 3.6. The streaming effect $\Delta_{streaming}$ is calculated for the KENO pebbles calculation by subtracting the KENO zones result from the reported k_{eff} . For the other calculations, $\Delta_{streaming}$ is the change in k_{eff} when using the corrected cross sections, compared to using the uncorrected cross sections. Also reported is the experimental value from Williams (1995).

Calculation	k_{eff}	$\Delta_{streaming}$
Experiment	1.0129	
KENO 238gr pebbles	1.01606	-1240
KENO 238gr $(\bar{\mu}\Sigma)_{corr}$	1.02311	-535
DALTON 50gr D_{corr}	1.01492	-1085
PHANTOM 50gr $(\bar{\mu}\Sigma)_{corr}$	1.01315	-932

The difference between DALTON and KENO is too large to be caused by statistical errors or differences in the geometry model, due to a significantly lower k_{eff} for the zones model. Diffusion models are well known to have troubles dealing with the void space above the pebble bed. Also, in the zones model, large changes in density occur in the pebble bed over small distances. Especially near the top of the pebble bed, where the density of the bed shows a sudden drop and is bordered by a void, diffusion models may have problems calculating the flux correctly.

Neutron Streaming Effect on k_{eff}

The effect of neutron streaming $\Delta_{streaming}$ on k_{eff} was calculated by comparing a KENO calculation using the zones model with a KENO calculation in which all pebbles were modelled separately. Also investigated was the effect of the streaming correction factor C_{str} by comparing KENO, DALTON and PHANTOM calculations using corrected cross sections with uncorrected calculations. The zones model was used for these calculations, except for PHANTOM. As before (see section 3.5.3), in PHANTOM the calculation using the zones model together with the corrected cross section set did not converge, so the homogeneous geometry model was used (and the result is compared with the homogeneous uncorrected calculation). Results are shown in Table 3.6

The streaming effect $\Delta_{streaming}$ from the KENO pebbles calculation is larger than observed for the infinite cylinder (Table 3.3). There are several explanations for this. In part this is due to the larger surface to volume ratio for the PROTEUS core. As one expects the leakage to be proportional to the surface area, a bigger surface area will result in more leakage. The PROTEUS core has a surface to volume ratio almost 50% larger than for the infinite cylinder, so $\Delta_{streaming}$ is also expected to be larger.

Secondly, as seen in the calculations for the infinite cylinder model, the standard

deviation for the streaming effect is over 100 pcm, which is mainly due to the stochastic nature of the pebble bed itself. However, the difference in $\Delta_{streaming}$ between PROTEUS and the infinite cylinder is too large to be explained by these effects alone.

The third factor is the different geometry layout for the PROTEUS core. Leakage at the upper surface, with its low pebble bed density bordered by void space, will have a larger effect on k_{eff} than leakage at a reflector wall, as the probability of a leaked neutron to be reflected back into the pebble bed is lower. Also, the probability for a leaked neutron to reenter the core is smaller in a finite geometry than in an infinite geometry, especially for neutrons near the corners of the core.

Finally, it should be noted that the results for the KENO pebbles model of $k_{eff} = 1.01606 \pm 0.00048$ compares well with the experimental result of 1.0129 ± 0.001 reported in Williams (1995), showing the importance of including neutron streaming in k_{eff} calculations for pebble beds.

Examining the $\Delta_{streaming}$ for the corrected calculations, as before the KENO calculations using corrected cross sections show poor comparison with the pebbles model. Results from applying the streaming correction to DALTON or PHANTOM compare well with the pebbles results, although still underestimating the streaming effect.

Effect of Non-Uniform Dancoff Factor on k_{eff}

As with the infinite cylinder model, the effect of possible variations in the Dancoff factor was examined. A separate set of cross sections was prepared for the pebble bed using a lower Dancoff factor, assuming neutrons exiting a pebble would have zero probability of reentering a new fuel pebble. For the homogenised core case, all core material within 6 cm of the core boundary was replaced with material using the lower Dancoff factor. The same was done in the zonal case. For the exact model, all pebbles with their centre within 6 cm of the core wall or top used the homogenised fuel zone with the lower Dancoff factor.

Calculations were performed with KENO for the homogenised case, the zones case, and the exact pebbles case, and the resulting k_{eff} was compared with the KENO results from Tables 3.5 and 3.6. The resulting differences Δ_{Dan} in k_{eff} due to changes in the Dancoff factor are in Table 3.7. As can be seen from the Table, there is no significant change in k_{eff} due to variations in the Dancoff factor in a pebble bed reactor.

3.7 Conclusions

The effect on k_{eff} of density fluctuations, neutron streaming in between the pebbles and variations in the Dancoff factor in a randomly stacked pebble bed were calculated for an infinite cylinder of 62.71 cm radius and for the PROTEUS experimental facility.

For the infinite cylinder model, taking into account radial density fluctuations in the pebble bed resulted in a small increase in k_{eff} compared to a uniform density model.

Table 3.7: k_{eff} and uncertainty σ (in pcm) of KENO calculations using a corrected Dancoff factor in the outer layer of the pebble bed, and the difference (Δ_{Dan} in pcm) with calculations using a uniform Dancoff factor.

Core model	k_{eff}	σ	Δ_{Dan}
Homogenised	1.02164	± 42	-33
Zones	1.02816	± 40	-30
Pebbles	1.01624	± 43	+18

However, for the PROTEUS core model taking into account both radial and axial density fluctuations in the pebble bed caused a much higher increase in k_{eff} . This leads to the conclusion that the effect of density fluctuations on k_{eff} due to wall effects can be neglected, but the lower packing fraction at the top of a pebble bed can cause a significant underestimation of k_{eff} when using a uniform packing fraction. For taller pebble beds, this effect will be smaller, as the region of lower density will be a smaller percentage of the total volume of the pebble bed. To take this effect into account when using a core model with a uniform density, one can use an effective height of the pebble bed half a pebble diameter lower than the top of the actual pebble bed, preserving the average packing fraction in the bulk of the pebble bed.

Neutron streaming caused a significant drop in k_{eff} in the infinite cylinder model. In the PROTEUS calculations neutron streaming lowered k_{eff} by more than 1%. For larger cores, the effect is expected to be smaller. However, even for larger cores such as the HTR-PM we expect a significant effect on k_{eff} due to streaming.

Applying the streaming correction to the diffusion coefficient as proposed by Lieberoth and Stojadinović (1980) significantly underestimated the change in k_{eff} due to neutron streaming. Thus, until a more accurate form of the correction factor for neutron streaming is found, an exact model of the pebble bed is required to accurately calculate k_{eff} for pebble bed reactors, especially for smaller cores.

Lowering the Dancoff factor in the outer 6 cm of the pebble bed to take into account the lower probability of neutrons to enter another fuel pebble here resulted for both the infinite cylinder model and PROTEUS in no significant change in k_{eff} , leading to the conclusion that variations in the Dancoff factor in pebble bed reactors can be ignored.

Finally, it should be noted that although both the non-uniform density profile and the neutron streaming effect can have a large influence on k_{eff} , especially for small cores such as PROTEUS, their effects on k_{eff} are of opposite sign. Thus, when using a homogeneous model, the errors made by ignoring both effects partially cancel, explaining the relative success of using homogeneous core models in pebble bed analysis.

TURBULENCE MODELLING FOR POROUS MEDIA IN PEBBLE BED REACTORS

The content of this chapter was submitted for publication to Nuclear Engineering and Design (Auwerda et al., 2014).

4.1 Introduction

To calculate flow and heat transfer inside pebble beds, the porous media approach is commonly used, in which a set of averaged equations is solved for a homogenised model of the pebble bed, using a porosity value to describe the pebble packing (Rousseau et al., 2006; Zhou et al., 2012). Probably the most widely used models to describe pebble bed flow and heat transfer are those detailed in the German KTA rules (KTA, 1983) and implemented in THERMIX (Struth, 1995; Lei et al., 2004). The KTA rules consist for a large part of empirical relations based on the behaviour of large beds. They do not take into account local variations in the bed, as it is almost impossible to measure locally the flow and heat transfer inside a pebble bed, especially without disturbing the flow field. Although they work well for the average of the entire bed, it is difficult to predict local behaviour in the case of non-uniform porosity distributions and near interfaces, such as near the wall, near complicated geometries, and at the top of the bed around the interface of the bed and void space. Codes based on these rules are often limited to 2D (structured) cylindrical geometries, and cannot include details such as the noses in the AVR reactor, coolant holes and control rods in the reflector, and the cone shape of the outflow region of the pebble bed. Recently more advanced codes are being developed including 3D capabilities, such as ATTICA3D (Seubert et al., 2012), but these are often

still based on highly empirical simplified equations and limited in the geometric shapes that can be modelled due to the use of structured grids.

It is well known that the porosity of randomly stacked beds is not uniform, but exhibits strong fluctuations near solid boundaries (Benenati and Brosilow, 1962), which for example can lead to increased coolant flow speeds at the wall, called wall-channelling (Schertz and Bischoff, 1969; Bader et al., 2011). Fluctuations in porosity also exist in the bulk of the bed due to the stochastic nature of the stacking, with porosities ranging from 0.28 to 0.60 for small clusters of pebbles (Auwerda et al., 2013). These changes in porosity might have significant effects on local coolant flow rates, and thus on local temperatures, which might result in hotspots. As these changes in porosity take place over small distances of the order of one pebble diameter, the validity of the existing models in predicting coolant flow and heat transfer is questionable in these cases, but also near complicated geometry structures such as corners, the noses in the AVR, and at interfaces between the pebble bed and void, as was illustrated by the discrepancy between predicted and measured temperatures in the AVR using melt-wire pebbles (Moormann, 2008).

In recent years, several researchers have calculated flow and heat transfer at the microscopic level by explicitly modelling the individual pebbles using direct numerical simulations (DNS) (Romkes et al., 2003), large-eddy simulations (LES) (Pavlidis and Lathouwers, 2013) or Reynolds average Navier-Stokes (RANS) (Shams et al., 2011). However, as the geometries and flow fields in a pebble bed are very complex, it is only possible to do these detailed calculations on very small clusters of pebbles, and even then it is difficult to do accurate calculations due to the high Reynolds number of the flow and the challenge of creating meshes that correctly capture the geometry with the touching pebbles (Lee et al., 2007a,b). As a typical pebble bed reactor contains 420,000 pebbles (Zhang et al., 2009) and even a small test reactor such as the HTR-10 contains 27,000 pebbles (Wu et al., 2002), these detailed methods can not be used for real reactors.

Taking a different approach to model flow through porous media, various authors have developed turbulence models for porous media (Masuoka and Takatsu, 1996; Antohe and Lage, 1997; Pedras and de Lemos, 2001; de Lemos, 2006; Nakayama and Kuwahara, 2008; Teruel and Rizwan-Uddin, 2009). These models use the porous media approach in which a porosity value is used to describe the geometry, and incorporate an extension of classical turbulence models to these porous media. The definition of the (turbulent) kinetic energy is not always the same in these models, and usually includes (at least partially) the dispersion of the flow due to the porous structure of the bed. The benefit of these models is that they use a less empirical description of flow through porous beds and include more physics. The various effects of the flow are separated and modelled independently, so that the models can be applicable to a broader range of problems. Flow and heat transfer in pebble beds do not purely depend on local properties, but also to some extent to the flow and bed geometry in the direct vicinity. The porous model can incorporate these effects through the transport equation of the kinetic energy, and should thus be able to better calculate flow and heat transfer around changes in porosity and

near boundaries. Finally, the equations for the kinetic energy can be stated in such a way that they become the regular turbulence equations for non-porous flow in the case the porosity is unity, which makes them very suitable to describe flow around the interface of void and bed, something that is not possible with the simplified empirical codes.

In this paper a new turbulence model for porous media is described, specifically for use in pebble beds. Its definition of the kinetic energy k closely resembles the work of Teruel and Rizwan-Uddin (2009), and does not attempt to make a distinction between time and space fluctuations, capturing in k all variations in the flow filtered out in the averaging process leading to the macroscopic porous flow equations. For the averaging process ensemble averaging methods (Drew, 1983) are used following the work of Lathouwers (1999); Lathouwers and Bellan (2001), which also form the main source for the closure relations for the various terms in the averaged equations. The derivation of the equations is detailed in Section 4.2.

The model was implemented in OpenFOAM (OpenFOAM Foundation, 2012), creating the pebFoam solver, supporting 3D calculations and unstructured meshes, and capable of investigating complicated geometries. Calculation results of pebFoam were compared with experimental results of two different experiments on the SANA facility, detailed in Section 4.3. In the first experiment the cavity was completely filled by a randomly stacked pebble bed, and in the second experiment only to 2/3 leaving a cavity above the bed. Next, to demonstrate the 3D capabilities of the code, the coolant flow and temperature distribution for a 1/30th core section of the HTR-PM including a fully detailed coolant channel in the reflector and cone shaped bottom of the core were calculated and compared with 2D results from THERMIX. For each of these cases, calculations were performed for both uniform and non-uniform porosity distributions. Finally, the results are discussed and conclusions presented in Section 4.5.

4.2 The flow and heat transfer model

In this section the turbulence model for porous media is derived, resulting in the averaged porous equations for continuity, momentum, enthalpy, kinetic energy and dissipation rate. Thermal non-equilibrium is assumed between the fluid and solid phase. The starting point of the derivation is similar to that of Teruel and Rizwan-Uddin (2009) in that the resulting kinetic energy k should capture all kinetic energy filtered in the averaging process, and the resulting averaged equations should become the clear-flow turbulent equations when the porosity goes to unity. All quantities are split into a space-time averaged quantity plus a fluctuation. There is no distinction between space and time fluctuations, they are all filtered out in the averaging process. The macroscopic turbulent kinetic energy (MTKE) k as defined here models all kinetic energy filtered out in the averaging process. It includes the trace of the hydrodynamic dispersion of the mean flow, also called dispersive kinetic energy (Raupach and Shaw, 1982). For a more detailed discussion, see Teruel and Rizwan-Uddin (2009).

In a pebble bed, besides time fluctuations there is dispersion of the flow due to the geometry of the bed. This dispersion leads to extra energy and momentum transport. In porous media models, the energy transport due to flow dispersion is often included as a dispersive conductivity in the diffusion term of the energy equation (Hunt and Tien, 1988). The momentum transport due to the flow dispersion is usually ignored, as inside porous media the flow resistance due to porous drag dominates the momentum equation. However, the momentum dispersion will lead to increased momentum exchange with the wall, as was shown by Giese et al. (1998). In our model, the kinetic energy of the dispersion of the flow is included in the MKTE. The dispersion of energy and momentum are included in their respective transport terms through the kinetic energy in the turbulent viscosity, similar to regular turbulence models.

One benefit is that this model can handle the effect of flow dispersion in a porous media on nearby areas, such as at the interface of porous and clear flow areas. Another benefit is that the momentum exchange with the wall is included. Finally, the resulting averaged equations are similar to the clear-flow turbulent equations. This makes it possible to use the model to calculate flow patterns around the interface of a void space above a pebble bed during natural circulation, something that is not possible with simplified empirical codes such as THERMIX and ATTICA3D.

First we define the averaging rules that are used, after which the derivation of the averaged or macroscopic equations is given, starting from the microscopic flow problem. Next, closure relations are given for the various parts, resulting in the k - ϵ closure model and its constants. The last section gives the temperature equation for the solid pebble phase.

4.2.1 Ensemble averaging

As was already mentioned, from a practical point of view we want to capture in the kinetic energy k all variations in the flow that contribute to momentum and heat transfer not captured in the averaged equations, which means we will not make any distinction between space fluctuations and time fluctuations. To derive the averaged equations we use ensemble averaging, based on a statistical average of individual realisations both in time and space, see Drew (1983) and Lathouwers and Bellan (2001). The ensemble average of a physical quantity f is

$$\langle f \rangle(\mathbf{x}, t) = \int_{\Omega} f(\mathbf{x}, t; \omega) d\mu(\omega) \quad (4.1)$$

where $d\mu(\omega)$ is the probability of observing realisation ω , and Ω is the set of all possible realisations. In the derivations below we will use the phase indicator $\chi(\mathbf{x}, t)$ which is 1 if the position (\mathbf{x}, t) is in the fluid phase and 0 when in the solid, and has the following properties:

$$\frac{\partial \chi}{\partial t} + \mathbf{u} \cdot \nabla \chi = 0 \quad (4.2)$$

$$\nabla \chi = \mathbf{n} \delta(\mathbf{x} - \mathbf{x}_i) \quad (4.3)$$

$$\phi = \langle \chi \rangle \quad (4.4)$$

where \mathbf{x}_i constitute all points on the interface, and \mathbf{n} denotes the surface normal vector pointing inwards the fluid. ϕ is the porosity of the pebble bed. The definition of the phase average \bar{f} of f is

$$\bar{f} = \frac{\langle \chi f \rangle}{\langle \chi \rangle} = \frac{\langle \chi f \rangle}{\phi} \quad (4.5)$$

with which we can decompose the local instantaneous quantity f in its average and a fluctuating part: $f = \bar{f} + f'$. Finally the interfacial average \bar{f}_i of a variable f is defined as

$$\bar{f}_i = \frac{\langle f \delta(\mathbf{x} - \mathbf{x}_i) \rangle}{\langle \delta(\mathbf{x} - \mathbf{x}_i) \rangle} = \frac{\langle f \delta(\mathbf{x} - \mathbf{x}_i) \rangle}{s} \quad (4.6)$$

where s is the average interfacial area per unit volume.

4.2.2 Averaging the equations

To obtain the averaged equations, we start with the local instantaneous equations, multiply them by the phase indicator χ , and take the ensemble average. In the following derivations we ignore the fluctuating part of the density ($\rho = \langle \rho \rangle$) except in the buoyancy term, but we do not assume the density to be constant. For the continuity equation

$$\frac{\partial \rho}{\partial t} + \nabla \cdot \rho \mathbf{u} = 0 \quad (4.7)$$

with \mathbf{u} the fluid velocity, the ensemble average reads

$$\frac{\partial \langle \chi \rho \rangle}{\partial t} + \nabla \cdot \langle \chi \rho \mathbf{u} \rangle = 0 \quad (4.8)$$

The local instantaneous momentum equation is

$$\frac{\partial \rho \mathbf{u}}{\partial t} + \nabla \cdot \rho \mathbf{u} \mathbf{u} = \nabla \cdot \boldsymbol{\sigma} + \rho \mathbf{g} \quad (4.9)$$

with stress $\boldsymbol{\sigma} = -p\mathbf{I} + \mu(\nabla \mathbf{u} + (\nabla \mathbf{u})^T) - \frac{2}{3}\mu \nabla \cdot \mathbf{u} \mathbf{I} = -p\mathbf{I} + \boldsymbol{\tau}$, pressure p , dynamic viscosity μ , gravitational acceleration \mathbf{g} and deviatoric stress tensor $\boldsymbol{\tau}$. \mathbf{I} is the identity tensor. The ensemble averaged momentum equation is

$$\frac{\partial \langle \chi \rho \mathbf{u} \rangle}{\partial t} + \nabla \cdot \langle \chi \rho \mathbf{u} \mathbf{u} \rangle = \nabla \cdot \langle \chi \boldsymbol{\sigma} \rangle + \langle \chi \rho \mathbf{g} \rangle - \langle \boldsymbol{\sigma} \cdot \nabla \chi \rangle \quad (4.10)$$

where the term $\mathbf{W} = -\langle \boldsymbol{\sigma} \cdot \nabla \chi \rangle$ is the fluid-solid momentum transfer, which is the drag force due to the porous structure. The local instantaneous enthalpy equation is

$$\frac{\partial \rho h}{\partial t} + \nabla \cdot \rho \mathbf{u} h = \nabla \cdot (\alpha \nabla h) \quad (4.11)$$

with h the fluid enthalpy and $\alpha = \mu/\text{Pr}$ its thermal diffusivity. The ensemble averaged enthalpy equation is

$$\frac{\partial \langle \chi \rho h \rangle}{\partial t} + \nabla \cdot \langle \chi \rho \mathbf{u} h \rangle = \nabla \cdot \langle \chi \alpha \nabla h \rangle - \langle \alpha \nabla h \cdot \nabla \chi \rangle \quad (4.12)$$

where the final term $\langle \alpha \nabla h \cdot \nabla \chi \rangle$ again represents the transfer at the fluid-pebble interface, in this case the heat transfer.

With the definitions from the ensemble averaging we can rewrite the averaged equations to:

$$\frac{\partial \phi \rho}{\partial t} + \nabla \cdot \phi \rho \bar{\mathbf{u}} = 0 \quad (4.13)$$

$$\frac{\partial \rho \phi \bar{\mathbf{u}}}{\partial t} + \nabla \cdot \rho \phi \bar{\mathbf{u}} \bar{\mathbf{u}} = \nabla \cdot \phi \bar{\boldsymbol{\sigma}} - \nabla \cdot \phi \rho \mathbf{R} + \phi \rho \mathbf{g} - \mathbf{W} \quad (4.14)$$

$$\frac{\partial \phi \rho \bar{h}}{\partial t} + \nabla \cdot \phi \rho \bar{\mathbf{u}} \bar{h} = \nabla \cdot \phi \alpha \nabla \bar{h} - \nabla \cdot \phi \overline{\rho \mathbf{u}' h'} - \langle \alpha \nabla h \cdot \nabla \chi \rangle \quad (4.15)$$

where we have defined the turbulent stress tensor $\mathbf{R} = \langle \chi \mathbf{u}' \mathbf{u}' \rangle / \phi$.

4.2.3 Closure

Various parts of the derived set of equations need closure. First, the averaged viscous stress $\bar{\boldsymbol{\tau}}$ is modelled similar to the microscopic stress tensor $\boldsymbol{\tau}$:

$$\bar{\boldsymbol{\tau}} = \mu (\nabla \bar{\mathbf{u}} + (\bar{\mathbf{u}})^T) - \frac{2}{3} \mu \nabla \cdot \bar{\mathbf{u}} \quad (4.16)$$

With the help of Equation 4.6 we can decompose the fluid-solid momentum transfer into $\mathbf{W} = -\bar{p}_i \nabla \phi + \mathbf{W}'$ and combine it with the stress term to write $\nabla \cdot \phi \bar{\boldsymbol{\sigma}} + \mathbf{W} = -\phi \nabla \bar{p} + \nabla \cdot \phi \bar{\boldsymbol{\tau}} + (\bar{p}_i - \bar{p}) \nabla \phi + \mathbf{W}'$. To model the interfacial momentum transfer, we use that the pressure difference between the bulk and the interface $(\bar{p}_i - \bar{p})$ will be small in the helium gas due to its low density, and can be either ignored or incorporated in the interfacial momentum transfer:

$$(\bar{p} - \bar{p}_i) \nabla \phi + \mathbf{W}' \approx \mathbf{W}' \quad (4.17)$$

Expressions for the interfacial momentum transfer itself are, especially for close packings, highly empirical, and we will use the usual pebble bed pressure drop equation from KTA rule 3101.3 (KTA, 1983), which can be written as:

$$\mathbf{W}' = 160 \frac{\mu}{d_{peb}^2} \frac{(1-\phi)^2}{\phi} \bar{\mathbf{u}} + 3 \frac{\mu^{0.1} \rho^{0.9}}{d_{peb}^{1.1}} \frac{(1-\phi)^{1.1}}{\phi^{0.1}} |\bar{\mathbf{u}}|^{0.9} \bar{\mathbf{u}} \quad (4.18)$$

with d_{peb} the pebble diameter. Along the same line the interfacial heat transfer $\langle \alpha \nabla h \cdot \nabla \chi \rangle$ is modelled as

$$\langle \alpha \nabla h \cdot \nabla \chi \rangle = -B \left(T_{peb} - \frac{h}{c_p} \right) \quad (4.19)$$

$$B = \frac{6(1-\phi) \alpha c_p \text{Nu}}{d_{peb} d_{peb}} \quad (4.20)$$

where c_p is the fluid specific heat capacity at constant pressure and Nu is the pebble-coolant heat transfer Nusselt number. This equation couples the coolant temperature with the pebble surface temperature T_{peb} . KTA rule 3102.2 (KTA, 1983) is used to determine the pebble-coolant heat transfer Nusselt number. The models used for these two quantities are empirical quantities based on the average properties of an entire pebble bed, and it would be highly desirable to derive models based on local properties of the pebble bed and fluid flow. As mentioned in the introduction, we expect that in the coming years detailed CFD calculations of small sections of the pebble bed will help construct such advanced models.

To find closure for the turbulent stress tensor \mathbf{R} a two-equation k - ϵ type model is derived. The transport equation for $R_{ij} = \langle \chi \mathbf{u}'_i \mathbf{u}'_j \rangle / \phi$ can be derived from $\langle u'_i \chi \mathcal{N}(u_j) + u'_j \chi \mathcal{N}(u_i) \rangle = 0$, where $\mathcal{N}(u) = 0$ is the Navier-Stokes equation in operator form.

$$\begin{aligned} \frac{\partial \phi \rho R_{ij}}{\partial t} + \frac{\partial \phi \rho \bar{u}_l R_{ij}}{\partial x_l} = & -\phi \rho \left(R_{il} \frac{\partial \bar{u}_j}{\partial x_l} + R_{jl} \frac{\partial \bar{u}_i}{\partial x_l} \right) \\ & + \frac{\partial}{\partial x_l} \left[\phi \left(-\overline{\rho u'_l u'_i u'_j} + u'_l \sigma'_{jl} + u'_j \sigma'_{il} \right) \right] + \phi \left(p' \frac{\partial u'_i}{\partial x_j} + p' \frac{\partial u'_j}{\partial x_i} \right) \\ & - \phi \left(\tau'_{jl} \frac{\partial u'_i}{\partial x_l} + \tau'_{il} \frac{\partial u'_j}{\partial x_l} \right) - \langle u'_i \sigma'_{jl} \frac{\partial \chi}{\partial x_l} + u'_j \sigma'_{il} \frac{\partial \chi}{\partial x_l} \rangle + \overline{\chi u'_i \rho' g_j} + \overline{\chi u'_j \rho' g_i} \end{aligned} \quad (4.21)$$

From this we construct the transport equation for the kinetic energy $k = \frac{1}{2} R_{ll}$, by taking the trace of the above equation:

$$\begin{aligned} \frac{\partial \phi \rho k}{\partial t} + \nabla \cdot \rho \phi \bar{\mathbf{u}} k = & -\phi \rho \mathbf{R} : \nabla \bar{\mathbf{u}} + \nabla \cdot \phi \left(-\frac{1}{2} \overline{\rho \mathbf{u}' (\mathbf{u}' \cdot \mathbf{u}')} + \mathbf{u}' \cdot \boldsymbol{\sigma}' \right) \\ & - \phi \overline{\boldsymbol{\tau}' : \nabla \mathbf{u}'} - \langle \mathbf{u}' \cdot \boldsymbol{\sigma}' \cdot \nabla \chi \rangle + \phi \overline{\rho' \mathbf{u}' \cdot \mathbf{g}} \end{aligned} \quad (4.22)$$

where we have used that the trace of the pressure-strain correlation is zero for low Mach number flows. Here the terms on the right hand side are, in order, the production due to mean shear, the transport of stress due to viscosity and fluctuations in velocity and pressure, the dissipation, the production/dissipation due to interfacial work, and the production/dissipation due to buoyancy. It should be noted that the kinetic energy k not only contains regular turbulence, but also dispersion of the flow due to the geometry of the pebble bed. It is a measure of the total kinetic energy of all deviations of the flow in the actual bed from the ensemble averaged flow field $\bar{\mathbf{u}}$ in the porous model. The production of the dispersive kinetic energy is included through the interfacial work term. This term includes the work done by the solid pebble bed to disperse the flow.

4. Turbulence modelling for porous media in pebble bed reactors

The separate terms in Equation 4.22 need closure. First, the turbulent stress tensor \mathbf{R} is modelled by the classical Boussinesq relation:

$$\mathbf{R} = \overline{(\mathbf{u}'\mathbf{u}')} = \frac{2}{3}k\mathbf{I} - \nu_T (\nabla \bar{\mathbf{u}} + [\nabla \bar{\mathbf{u}}]^T) + \frac{2}{3}\nu_T \nabla \cdot \mathbf{u}\mathbf{I} \quad (4.23)$$

$$\mu_T = \rho \nu_T = \rho C_\mu k^2 / \epsilon \quad (4.24)$$

where the turbulent viscosity μ_T is written as in the standard k - ϵ model and C_μ is a model constant. For the turbulent and molecular transport term the usual eddy-viscosity based gradient diffusion formulation is used.

$$\nabla \cdot \phi \left(-\frac{1}{2} \rho \mathbf{u}'(\mathbf{u}' \cdot \mathbf{u}') + \mathbf{u}' \cdot \boldsymbol{\sigma}' \right) = \nabla \cdot \phi \left(\frac{\mu_T}{\sigma_k} + \mu \right) \nabla k \quad (4.25)$$

with σ_k a model constant. This formulation is also used for the turbulent/dispersive enthalpy transport

$$\phi \overline{\rho \mathbf{u}' h'} = -\phi \frac{\mu_T}{\sigma_t} \nabla h \quad (4.26)$$

where σ_t is another constant of the k - ϵ model. This term includes the heat transfer due to flow dispersion in the porous bed. The buoyancy term is similarly modelled with a gradient-type diffusion model, see also de Lemos and Braga (2003)

$$\phi \overline{\rho' \mathbf{u}' \cdot \mathbf{g}} = -\frac{\phi}{\rho} \frac{\mu_T}{\sigma_t} \mathbf{g} \cdot \nabla \rho \quad (4.27)$$

The interfacial work $-\langle \mathbf{u}' \cdot \boldsymbol{\sigma}' \cdot \nabla \chi \rangle$ is handled as in Teruel and Rizwan-Uddin (2009). They noted $\mathbf{u} = 0$ at the interface. But as $\mathbf{u} = \bar{\mathbf{u}} + \mathbf{u}'$, this means $\mathbf{u}' = -\bar{\mathbf{u}}$ at the interface, and we can rewrite the term as

$$-\langle \mathbf{u}' \cdot \boldsymbol{\sigma}' \cdot \nabla \chi \rangle = \langle \bar{\mathbf{u}} \cdot \boldsymbol{\sigma}' \cdot \nabla \chi \rangle = \bar{\mathbf{u}} \cdot \langle \boldsymbol{\sigma}' \cdot \nabla \chi \rangle = \bar{\mathbf{u}} \cdot \mathbf{W} \quad (4.28)$$

where \mathbf{W} is modelled using Equation 4.18. Finally, the dissipation term is

$$-\phi \overline{\boldsymbol{\tau}' : \nabla \mathbf{u}'} = -\rho \phi \epsilon \quad (4.29)$$

and the transport equation for the dissipation rate is written similar as in the classical k - ϵ model, resulting in the following set of equations:

$$\frac{\partial \rho \phi}{\partial t} + \nabla \cdot \phi \rho \bar{\mathbf{u}} = 0 \quad (4.30)$$

$$\begin{aligned} \frac{\partial \rho \phi \bar{\mathbf{u}}}{\partial t} + \nabla \cdot \rho \phi \bar{\mathbf{u}} \bar{\mathbf{u}} &= -\phi \nabla \bar{p} + \phi \rho \mathbf{g} - \mathbf{W} \\ &+ \nabla \cdot \phi (\mu + \mu_T) (\nabla \bar{\mathbf{u}} + (\nabla \bar{\mathbf{u}})^T - \frac{2}{3} (\nabla \cdot \bar{\mathbf{u}}) \mathbf{I}) \end{aligned} \quad (4.31)$$

$$\frac{\partial \phi \rho \bar{h}}{\partial t} + \nabla \cdot \phi \rho \bar{\mathbf{u}} \bar{h} = \nabla \cdot \phi \left(\alpha + \frac{\mu_T}{\sigma_t} \right) \nabla \bar{h} + \frac{6(1-\phi)}{d_{peb}} \frac{\alpha c_p \text{Nu}}{d_{peb}} \left(T_{peb} - \frac{h}{c_p} \right) \quad (4.32)$$

$$\begin{aligned} \frac{\partial \phi \rho k}{\partial t} + \nabla \cdot \phi \rho \bar{\mathbf{u}} k = & -\phi \rho \mathbf{R} : \nabla \bar{\mathbf{u}} - \rho \phi \epsilon + \bar{\mathbf{u}} \cdot \mathbf{W} \\ & + \nabla \cdot \phi \left(\frac{\mu_T}{\sigma_k} + \mu \right) \nabla k - \frac{\phi}{\rho} \frac{\mu_T}{\sigma_t} \mathbf{g} \cdot \nabla \rho \end{aligned} \quad (4.33)$$

$$\begin{aligned} \frac{\partial \phi \rho \epsilon}{\partial t} + \nabla \cdot \phi \rho \bar{\mathbf{u}} \epsilon = & -C_1 \frac{\epsilon}{k} \phi \rho \mathbf{R} : \nabla \bar{\mathbf{u}} + \nabla \cdot \phi \left(\mu + \frac{\mu_T}{\sigma_\epsilon} \right) \nabla \epsilon - C_2 \rho \phi \frac{\epsilon^2}{k} \\ & - C_1 C_3 \frac{\epsilon}{k} \frac{\phi}{\rho} \frac{\mu_T}{\sigma_t} \mathbf{g} \cdot \nabla \rho - C_W \frac{|\bar{\mathbf{u}}|}{d_{peb}} \bar{\mathbf{u}} \cdot \mathbf{W} \end{aligned} \quad (4.34)$$

where C_1 , C_2 , C_3 , σ_ϵ and C_W are model constants, and $|\bar{\mathbf{u}}|/d_{peb}$ is the inverse of the timescale of the dissipation of the kinetic energy due to the porous structure of the medium (the dispersion of the flow).

4.2.4 Model constants

Like normal turbulence models, the final set of equations contain various model constants. For most constants, we use the same values as in the standard Launder-Spalding model (Launder and Spalding, 1974). Note that for $\phi \rightarrow 1$ the standard model is obtained from the derived porous model. As suggested in Lathouwers (1999); de Lemos (2006) we use for $C_W = C_2$. The last constant σ_t describes the relation between the amount of kinetic energy in the fluctuations of the flow and the resulting increase in heat transfer. We can use the KTA relation for the increase in heat transfer in a uniform pebble bed to find this model constant, by relating the effective diffusion of heat according to the KTA rule with μ_T/σ_t and the steady state values of k and ϵ in an infinite bed.

For 1D steady state flow in an infinite medium, values for k and ϵ are

$$k = \frac{C_{\epsilon 2}}{C_{\epsilon W}} \frac{d_{peb}}{\|\mathbf{u}\|} \frac{\mathbf{u} \cdot \mathbf{W}}{\rho \phi} \quad (4.35)$$

$$\epsilon = \frac{\mathbf{u} \cdot \mathbf{W}}{\rho \phi} \quad (4.36)$$

resulting in

$$\mu_T = \rho C_\mu \frac{k^2}{\epsilon} = \rho C_\mu \left(\frac{C_{\epsilon 2} d_{peb}}{C_{\epsilon W} \|\mathbf{u}\|} \right)^2 \frac{\mathbf{u} \cdot \mathbf{W}}{\rho \phi} \quad (4.37)$$

According to Schlünder (1966) the effective thermal conductivity due to convection in a pebble bed can be written as

$$\lambda_{eff} = \lambda \text{Pe} / K \quad (4.38)$$

where $Pe = RePr$ is the Peclet number and

$$K = 8 \left(2 - \left(1 - 2 \left(d_{peb} / D_{bed} \right) \right)^2 \right) \quad (4.39)$$

which is for large beds similar to $\lambda_{eff} = \lambda_0.11Pe$ found by Wakao and Kato (1969). Combining Equations 4.37 and 4.38 with $\lambda_{eff} = \mu_T / \sigma_t$, taking typical properties for large pebble beds such as the HTR-10 ($D/d = 30$) and HTR-PM ($D/d = 50$), helium properties at $p = 7$ MPa and $T = 500^\circ\text{C}$, a flow speed of $u = 4$ m/s and a porosity $\phi = 0.39$ results in $\sigma_t = 1.46$.

4.2.5 Solid pebble temperature equation

As fluid and solid temperatures can be different in porous media, a separate temperature equation is solved for the pebble temperatures. This equation solves for the pebble surface temperature T_{peb} .

$$\frac{\partial(1-\phi)\rho_{peb}c_{p,peb}T_{peb}}{\partial t} = \nabla \cdot K_{peb,eff} \nabla T_{peb} + B(T_{peb} - T_{fluid}) + Q \quad (4.40)$$

Here Q is the power density in the pebble bed and $K_{peb,eff}$ is the effective thermal conductivity through the pebble phase. For $K_{peb,eff}$ the Zehner-Bauer-Schlünder correlation is used (Zehner and Schlünder, 1972; Breitbach and Barthels, 1980; IAEA, 2000). The pebble surface temperature equation is coupled to the fluid temperature T_{fluid} through the pebble-coolant heat transfer B defined in Equation 4.20.

4.3 Calculations for SANA experiments

The SANA test facility (Selbsttätige Abfuhr der Nachwärme) was built in the '90's at FZJ (Forschungszentrum Jülich) to supply experimental data for the heat transfer in pebble beds (Lange, 1995). The facility consists of a central heating rod, surrounded by a pebble bed of 1 m high and 1.5 m in diameter. The top and bottom of the bed are heavily insulated to minimise axial heat losses, and the whole facility is encased in a steel cylindrical vessel, see Figure 4.1. The main path for heat transfer is in the radial direction through the pebble bed and through the steel vessel to the surrounding air. Several experiments were performed with the SANA facility from 1994-1996 using different pebble sizes and materials, different heating powers, and different gases (Stöcker and Nießen, 1997; Stöcker, 1998). Two of these experiments were selected to compare with calculation results from the pebFoam code, both under helium atmosphere with no forced convection and using graphite pebbles of 6 cm diameter. The first experiment used a completely filled bed heated by a full-length heating rod at 35 kW. In the second experiment the cavity was filled with pebbles up to 2/3 leaving a void above the bed, heated by a half-length rod at 25 kW. First, a detailed description of the SANA facility is given, followed by a description of the two experiments with a comparison of calculation results from pebFoam with the measurements. In Section 4.3.4 the grid quality is examined using a grid convergence study.

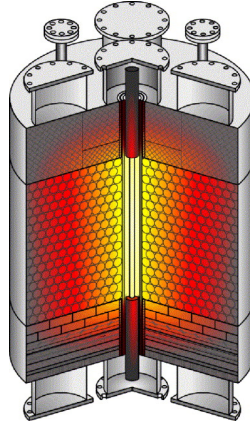


Figure 4.1: Overview of the SANA test facility (Stöcker and Nießen, 1997).

4.3.1 Description of the SANA facility

A schematic overview of the 2D r - z geometric model of the SANA facility used in the calculations is given in Figure 4.2. The facility is centrally heated by a hollow graphite heating rod with inner and outer radii of $r_i = 1.1$ cm and $r_o = 1.6$ cm, which is connected at the top and bottom to the electric power supply by solid graphite electrodes with a radius of 4.0 cm. The rod is surrounded by a graphite tube with inner and outer radii of $r_i = 5.5$ cm and $r_o = 7.0$ cm to protect it from the pebble bed. The main heat transfer mechanism to the protection tube is radiation. The top and bottom electrodes are surrounded by water jackets to cool them.

The pebble bed rests on layers of various insulation materials with a total thickness of 40 cm, designed for insulation and also to bear the load of the pebble bed. The top of the 1 m high cavity containing the bed is also insulated with a 40 cm thick layer. In radial direction the pebble bed is bounded at $r = 7$ cm by the outside of the protection tube and at $r = 75$ cm by the inside of the 6 mm thick steel vessel surrounding the facility. During the experiments several pebble sizes and materials were used, but the two experiments we investigated both used pebbles made of non-irradiated graphite type Sigri AL-2-500 with a diameter of $d_{peb} = 6$ cm, and in both of the experiments the SANA facility was filled with helium gas at ambient pressure. For a description of the various graphite and insulation material properties see Stöcker and Nießen (1997).

To measure the temperature inside the pebble bed and the surrounding materials, thermocouples were installed inside the pebble bed, in the insulation layers, on the inside of the protection tube, and on the surface of the steel vessel at various horizontal and radial positions. The thermocouples inside the pebble bed were attached to the surface of the graphite pebbles. As the thermal conductivity of the pebbles is much higher than that

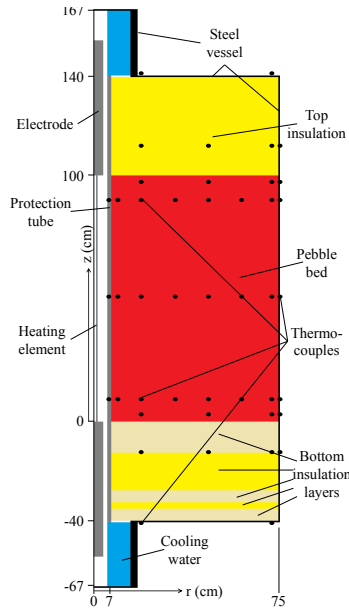


Figure 4.2: Geometric model of the SANA experimental facility

of the helium, measured temperatures were effectively the pebble surface temperatures. The reported uncertainties for the thermocouples were 1% in temperature, 2 cm in axial, and 1 cm in radial position (Stöcker, 1998).

Stöcker (1998) reported that when fully filled the bed contained approximately 9500 pebbles of 6 cm diameter and had a bulk porosity of 0.41. However, given the dimensions of the bed, 9500 pebbles result in an average porosity of 0.39, and to get a porosity of 0.41 the bed would have to contain 9138 pebbles. Also, it was mentioned the void fractions within half a pebble diameter of the inner and outer cylindrical walls should be taken as 0.65 and 0.50 to take the effect of the wall into account, but the possible effects on the porosity near the top and bottom of the bed were not mentioned.

To better define the porosity distribution of the bed we generated a pebble bed with the desired dimensions using the removing overlaps method developed by us and detailed in Auwerda et al. (2013), resulting in a bed containing 9348 pebbles, with an average porosity of 0.3965. The resulting locally averaged porosities for the regions within 3 cm of the walls are 0.5209 at the inner boundary, 0.5025 at the outer wall, 0.4785 at the bottom of the bed and 0.8655 at the top. The porosity for the bulk of the bed more than half a pebble diameter away from the walls is 0.3681. Both the average porosity of the bed and the porosity near the inner wall of the bed are significantly different than the values reported in literature, and the effects on the porosity near the bottom and especially the top of the

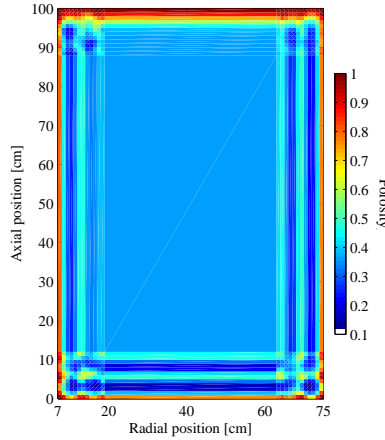


Figure 4.3: Porosity map of the pebble bed for the completely filled pebble bed.

bed are significant.

The porosity distribution of the bed was calculated for each 1 cm layer within 12 cm of the walls, and for the bulk of the bed 12 cm away from the walls. The resulting spatial distribution of the void fraction is shown in Figure 4.3 where the variations in void fraction near the walls is clearly visible. These fluctuations are absent at the top of the bed, where the porosity gradually goes to zero towards the wall, as here the bed is not formed against the wall, but simply not filled any further.

As was mentioned in Stöcker (1998); Bader et al. (2011), even though the experiments were carried out at atmospheric pressure, where effects of natural convection are generally small, natural circulation in the bed had a significant influence on the resulting temperature distribution in the facility. As the resulting velocity distribution strongly depends on the porosity in the bed, we calculated the temperature distributions of the experiments for both a nonuniform (realistic) porosity distribution shown in Figure 4.3, and for a uniform porosity distribution with the porosity set everywhere to the average value of 0.3965.

In pebFoam radiative heat transfer from the heating rod and electrodes to the protective sleeve and other surrounding parts was included. Another challenge was modelling the heat transfer from the steel vessel to the surroundings. The surface of the steel vessel was surrounded by a wire-mesh to prevent people from touching the hot wall, and the air temperature inside the room containing the facility was measured during the experiments. However, the heat transfer from the vessel to the surroundings was very complicated, and happened through natural convection and radiation. The literature suggests using a heat transfer coefficient of $9 \text{ W/m}^2\text{K}$. However, for a steel vessel at 225°C with emissivity of

0.8 and an ambient room of 25°C, the heat transfer due to radiation alone would already result in a heat transfer coefficient of $h = \dot{q}_{rad}/\Delta T = 0.8\sigma(498^4 - 298^4)/(498 - 298) = 12.2 \text{ W/m}^2\text{K}$, and the coefficient would be highly temperature dependent. Thus, we implemented a temperature dependent heat transfer at the outside of the steel vessel combining radiative heat transfer to the surrounding and free convection at a vertical plate. For the convective part the Nusselt number was calculated using $Nu = 0.13(GrPr)^{1/4}$ (Janssen and Warmoeskerken, 1987), where Gr and Pr are the Grashof and Prandtl numbers. To estimate the reduction in heat transfer due to the wire-mesh surrounding the steel vessel, the vessel surface heat transfer was multiplied by a constant. This constant was adjusted to get the best match between calculated and measured vessel surface temperatures, resulting in a value of 0.85.

A 2D grid was created with the blockMesh OpenFOAM utility. The grid was pure orthogonal, with grid cells outside the pebble bed on average 2 cm wide. Inside the pebble bed, 30 cells in radial and 48 cells in axial direction were used for the bulk of the bed. The area from 1 to 12 cm from the walls was split in 33 uniform cells. The area within 1 cm of the walls was split in 6 cells, using a non-uniform grading of the cells with a cell-width-ratio of 1.1, resulting in a cell width of $\Delta y = 0.1296 \text{ cm}$ next to the wall. The total mesh size was 13608 cells for the pebble bed part, plus 1568 cells for the surrounding geometry.

4.3.2 Completely filled pebble bed

The first SANA experiment simulated with pebFoam had a cavity completely filled with 6 cm diameter graphite pebbles forming a 1 m high pebble bed, a nominal heating power of 35 kW, and a helium atmosphere. The total power dissipated in the heating rod of 32.02 kW and in the electrodes of 1.94 kW was given in Stöcker (1998) and used as a volumetric source in the components. As was mentioned in Section 4.3.1, calculations were performed for both a uniform and a nonuniform porosity distribution. The calculated velocity fields are in Figures 4.4a and 4.4b. In Figure 4.5 the axial velocities u_z for the uniform and nonuniform porosity halfway up the bed at $z = 50 \text{ cm}$ are shown versus the radial position r .

Comparing the velocity fields in Figure 4.4, both fields show the natural circulation of the helium gas inside the pebble bed. However, in the case of nonuniform porosity the flow is much more confined to the walls, where porosity is large and thus flow resistance is small, with a much higher flow speed. Both flow fields are similar to the flow fields in Bader et al. (2011), except that for the nonuniform case wall-channelling is also observed at the top and bottom of the bed. Both flow fields have a higher flow speed at the inner wall compared to the outer wall, as the helium density is lower at the inner wall due to the higher temperature, and because of the smaller radius of the bed at the inner wall. For the nonuniform case the difference in flow speed in Figure 4.4b is especially evident due to the strong wall-channelling effect, with an even higher porosity and thus stronger wall-channelling at the inner wall than at the outer. As can be seen in Figure 4.5, in the bulk of the bed the fluid velocities of the uniform and nonuniform case are similar.

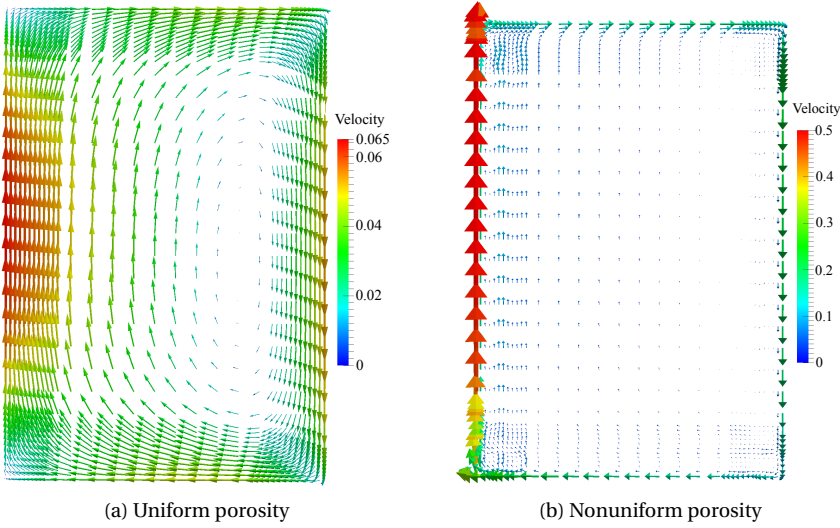


Figure 4.4: Calculated helium velocity fields (in m/s) for the 35kW completely filled pebble bed.

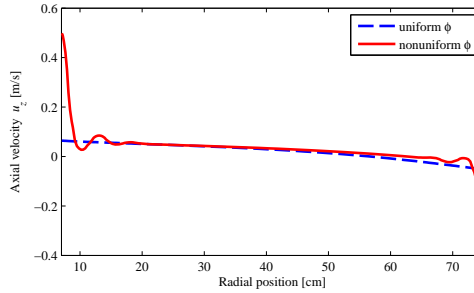


Figure 4.5: Axial helium velocity for the completely filled pebble bed at $z = 50$ cm (centre of bed).

Clearly visible is the increased flow speed at the walls due to the higher porosity for the nonuniform porosity distribution, resulting in an increase of 27% in the circulating mass flow due to natural circulation.

In Figure 4.6a the calculated temperature profiles are shown as a function of axial position, with the dashed lines depicting the calculations using a uniform porosity distribution and the solid lines a nonuniform porosity distribution. The axial temperature profiles are shown at various fixed radial positions, corresponding to measurement positions

4. Turbulence modelling for porous media in pebble bed reactors

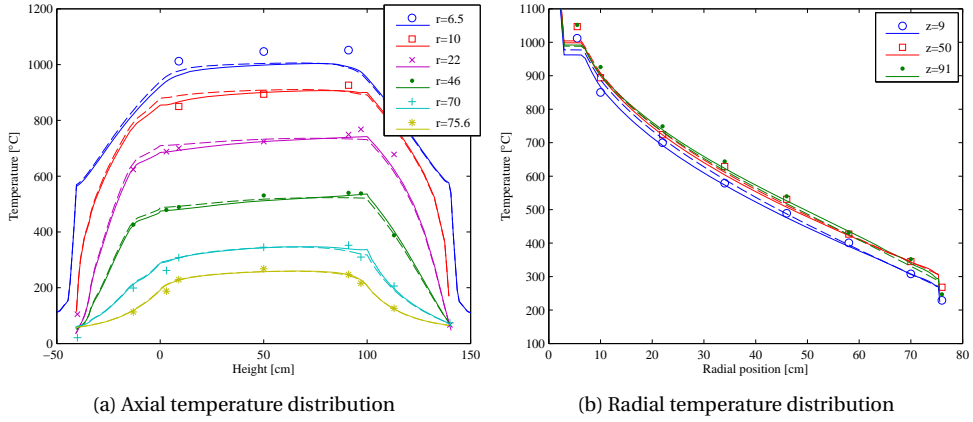


Figure 4.6: Calculated solid temperature profiles for uniform (dashed line) and nonuniform (solid line) porosity distribution compared with experimental results (symbols) for the completely filled pebble bed.

in the SANA experiment, shown as symbols in the figure. During the SANA experiment measurements were also performed with thermocouples at $r = 34$ and $r = 58$ cm, but for readability we have chosen not to show these measurements. The pebble bed is located between $0 < z < 100$ cm, and $7 < r < 75$ cm, with above and below the bed the insulation materials. The temperature profile at $r = 75.6$ cm corresponds to the outer surface of the steel vessel surrounding the pebble bed. In Figure 4.6b the temperature profiles are shown as a function of radial position, near the bottom ($z = 9$), middle ($z = 50$), and at the top ($z = 91$) of the bed.

At most measurement points there is a good match between the measured and calculated temperatures, especially for the nonuniform porosity calculations. Only the measurement points at $r = 6.5$ cm show a clear discrepancy with the calculation results. Stöcker (1998) reports that the thermocouples were situated at $r = 6.5$ cm. However, the same report also gives an inner and outer radius of the protection tube of 5.5 and 7 cm. Thus it is unclear where exactly the thermocouples were situated. The strange shape of the radial temperature profiles in Figure 4.6b at $r < 5.5$ cm is because here the helium void is situated between the heating rod and protection tube, where most heat transport takes place by radiation.

The measurements show higher temperatures near the top of the bed than near the bottom as a result of natural circulation. The calculated temperatures for the uniform porosity distribution show smaller temperature differences between the top and bottom of the bed. The calculation results for the nonuniform case show a better match, showing a comparable temperature gradient between the bottom and top of the bed as the

measurements. As a result of the lower porosity near the walls, there is a stronger natural circulation in the nonuniform porosity case, leading to a bigger difference between temperatures at the bottom and top of the bed, which can be clearly seen in the profiles in Figure 4.6a. For the radial temperature profiles in Figure 4.6b this results in a larger difference between the temperature profiles at $z = 9$ cm and $z = 91$ cm than for the uniform porosity case. On average, the difference between calculated and measured temperatures inside the pebble bed was 15.8 °C (1.9%) for the uniform porosity distribution with a maximum difference of 38.6 °C (6.4%) at $r = 10$, $z = 9$. The nonuniform distribution resulted in noticeably lower differences with the measurements, with an average difference of 12.6 °C (1.6%) and a maximum difference of 30.5 °C (5.6%) at $r = 70$, $z = 3$. The biggest temperature differences for the nonuniform case are at the top and bottom corners at the cold wall, where local temperatures might be influenced by the local structure of the packing. Given the uncertainty in the measurements due to uncertainties in measured temperatures and in measurement location (the radial temperature gradient is around 10 °C per cm), other differences between calculated and measured temperatures are acceptable.

Stöcker (1998) calculated temperature profiles with both TINTE and THERMIX for a nonuniform porosity distribution. Similar to our results he found a relative large difference at $r = 70$, $z = 3$ between his calculated results and the measured value. However, where our results match the other measured values in the bed quite well, he found a larger discrepancy between his calculated values and the measured values towards the centre of the pebble bed. Results for TINTE overestimated temperatures at $r = 10$ cm with more than 50 °C where THERMIX underestimated temperatures with more than 100 °C, and both codes strongly underestimated the axial temperature gradient in this region. Similarly, results by Bader et al. (2011) using ATTICA3D also show differences with measured values of more than 50 °C.

4.3.3 Partially filled pebble bed

For the second SANA experiment used for validation of pebFoam, the top part of the pebble bed was removed, leaving a 66 cm high pebble bed with a cavity of 34 cm above the bed. This case was chosen to demonstrate the capability of pebFoam to calculate heat and mass transfer including natural circulation for a pebble bed topped with an empty cavity. This is not possible with simplified empirical codes such as THERMIX and ATTICA3D, as they do not contain models for momentum interchange between flow regions or with the walls. Different flow regions such as the void space above the bed and the pebble bed only though mass flows.

The bed was heated at the bottom 50 cm using a half length heating rod, with the top half of the heating rod replaced by a longer electrode. Again 6 cm diameter graphite pebbles were used with helium as gas and a nominal heating power of 25 kW Stöcker (1998). The power dissipated in the heating rod was reported as 20.34 kW, with 3.43 kW dissipated in the electrodes. As before calculations were performed for a uniform and a

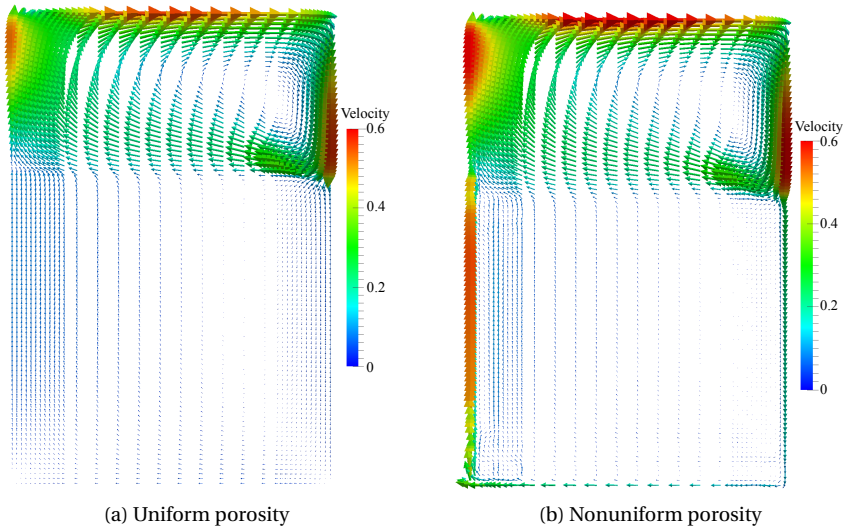


Figure 4.7: Calculated helium velocity fields (in m/s) for the 25kW partially filled pebble bed.

nonuniform porosity distribution in the pebble bed. To get these porosities the computer generated stacking described in Section 4.3.1 was used, but with all pebbles with any part above 66 cm removed. This resulted in a 66 cm high pebble bed containing 6059 pebbles, with an average porosity of 0.4073, lower than for the full pebble bed because there are relatively more edge effects in a smaller bed. For the nonuniform porosity distribution a detailed distribution similar to the one depicted in Figure 4.3 was used, while for the uniform porosity distribution a uniform porosity of 0.4073 was used, and both beds used a porosity of 1 for the cavity above the bed. The mesh was similar as the mesh for the completely filled bed, except that the mesh resolution in the axial direction was finer to capture the interface between the pebble bed and cavity.

The calculated velocity fields using a uniform and nonuniform porosity are shown in Figures 4.7a and 4.7b respectively. Both fields show a relatively strong natural circulation in the cavity, with the backwards flow along the top of the pebble bed partially penetrating the top layer of the bed. The flow speeds through the pebble bed are much lower than in the cavity, but only slightly lower than in the completely filled pebble bed experiment, see Figures 4.5 and 4.8. As for the completely filled pebble bed experiment, in the nonuniform case the wall channelling effect is clearly visible, resulting in a 14% higher mass flow through the pebble bed due to natural convection than for the uniform porosity distribution, and in a 13% increased in the natural convection in the cavity above the bed.

As in the previous section, the axial solid temperature profiles for the uniform (dashed

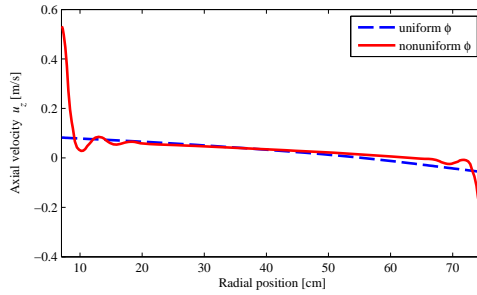


Figure 4.8: Axial helium velocity for the partially filled pebble bed at $z = 50$ cm (centre of bed).

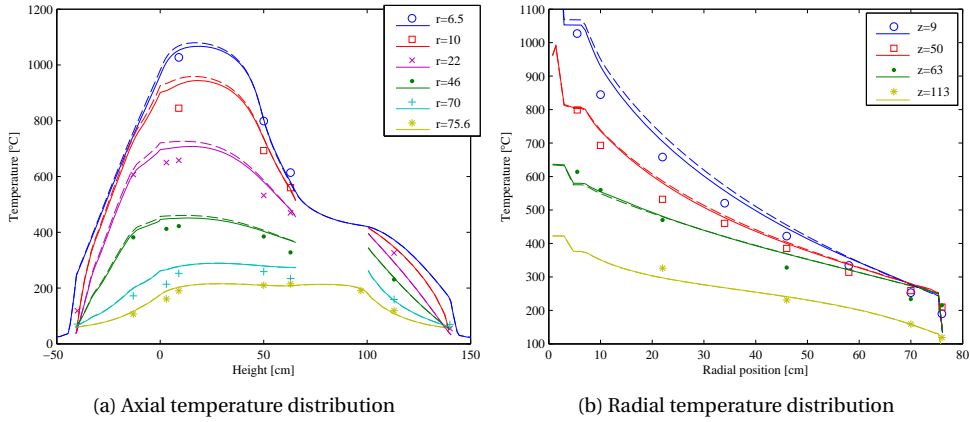


Figure 4.9: Calculated solid temperature profiles for uniform (dashed line) and nonuniform (solid line) porosity distribution compared with experimental results (symbols) for the partially filled pebble bed.

line) and nonuniform (solid line) porosity profiles are shown in Figure 4.9a for various radial positions together with the experimental results. As there were no pebbles between $z = 66$ cm and $z = 100$ cm, here no temperature values inside the bed are shown. The radial solid temperature profiles are shown in Figure 4.9b, including the radial temperature profile at $z = 113$ cm through the top insulation layer, as there were no measurements in the cavity above the pebble bed. In Figure 4.9a strong axial temperature gradients can be seen near the top of the bed at $z = 66$ cm, as only the bottom half of the bed was heated, and the top half lost heat through radiation and through the stronger convection in the cavity on top of the bed. There is a reasonable match for the temperature profiles with the measurements, with temperatures for the nonuniform porosity distribution again

Table 4.1: Meshes used for grid convergence study. N_{cells} is the number of mesh cells in the mesh, and Δy is the width of the smallest cell next to the wall.

Index	N_{cells}	Δy
1	1512	0.4762
2	6048	0.2155
3	13608	0.1296

closer to the measured values than for the uniform porosity distribution. On average, the difference between calculated and measured temperatures inside the pebble bed was 40 °C (1.9%) for the uniform porosity distribution with a maximum difference of 106 °C (6.4%) at $r = 10$, $z = 9$. The nonuniform distribution resulted in noticeably lower differences with the measurements for almost every point, with an average difference of 33 °C (1.6%) and a maximum difference of 85 °C (5.6%) at $r = 10$, $z = 9$. Even with the increased natural circulation in the nonuniform porosity case, calculated temperatures inside the bed, especially near the bottom and close to the heating rod, were higher than was measured. As in the completely filled bed the calculated effective heat transfer in radial direction through the pebble bed was relatively accurate, perhaps the dissipated power in the heating rod was higher than reported.

4.3.4 Grid convergence study

To evaluate the mesh quality, for both the completely filled and the partly filled bed the grid convergence was examined using the method described by Roache (1998) based on Richardson extrapolation. Three different grids were compared. The finest one is the one described in Section 4.3.1, consisting of 108×126 cells with a cell width next to the wall of $\Delta y = 0.1296$ cm. Two coarser grids were used, the middle-sized grid had 54×63 cells and $\Delta y = 0.2155$ cm, and the coarsest grid had 36×42 cells and $\Delta y = 0.4762$ cm, see Table 4.1.

To perform the grid convergence study, the calculated temperatures at three thermocouple locations were compared: near the hot wall ($r = 10$, $z = 50$); near the bottom of the bed ($r = 46$, $z = 3$); and near the top of the bed ($r = 46$, $z = 97$). For the grid refinement ratios r_{ij} between grid i and j the ratios between the cell-widths at the wall are used, resulting in $r_{12} = 2.21$ and $r_{23} = 1.6625$. The grid convergence rate p is calculated with

$$p = \frac{1}{\ln(r_{23})} \left(\ln\left(\frac{T_{12}}{T_{23}}\right) + \ln\left(\frac{r_{23}^p - 1}{r_{12}^p - 1}\right) \right) \quad (4.41)$$

where $T_{ij} = T_i - T_j$ is the difference in calculated temperatures for grid i and j . The grid convergence index (GCI) provides an estimate of the amount of discretisation error in

Table 4.2: Results for the grid convergence study for the partly filled bed and nonuniform porosity distribution applied to the temperature at three different locations. T_i is the calculated temperature for grid i , T_{23}^* is the extrapolated solution and $GC I_{23}$ is the grid convergence index of the fine mesh.

Location (r, z)	(10, 50)	(46, 3)	(46, 97)
T_1	1011.62	714.90	621.42
T_2	1009.65	715.94	621.80
T_3	1009.26	716.27	621.92
T_{23}^*	1008.97	716.73	622.09
$GC I_{23}$	0.0394%	0.0810%	0.0329%

the finest grid solution relative to the converged numerical solution

$$GC I_{23} = 1.25 \frac{|T_3 - T_2|/T_3}{r_{23}^p - 1} \quad (4.42)$$

The extrapolated solution T_{23}^* , which is the solution for an infinitely fine mesh, can be estimated with

$$T_{23}^* = \frac{r_{23}^p T_3 - T_2}{r_{23}^p - 1} \quad (4.43)$$

Results for the partly filled bed with nonuniform porosity distribution are given in Table 4.2. Similar or smaller values for the $GC I_{23}$ were found for the uniform distribution, and for the completely filled bed for both uniform and nonuniform porosity distribution. The very small values for the $GC I_{23}$ show results for the fine grid are very close to the solution for an infinitely fine mesh.

4.4 HTR-PM 3D calculations

The Chinese High Temperature Reactor-Pebble bed Modular (HTR-PM) is a 250 MW_{th} reactor design, with an 11 m high pebble bed consisting of 420,000 6 cm diameter graphite pebbles, contained within a 3 m diameter cylindrical cavity surrounded by graphite reflectors. The coolant is helium at a pressure of 7 MPa, which first flows upwards through 30 coolant channels situated evenly spaced in the reflector at a distance of 2 m from the centre of the bed, before flowing down through the bed. The helium mass flow rate is 96 kg/s, with an inflow temperature of 250 °C and an outflow temperature of 750 °C (Zhang et al., 2009). The first HTR-PM is currently under construction in Shidaowan, China. We have chosen the HTR-PM reactor design to test the 3D capabilities of pebFoam and its ability to simulate a full reactor, making use of pebFoam's ability to capture complicated geometric shapes. First a detailed description will be given of the geometric model used in the calculations, followed by the results compared with calculation results by THERMIX

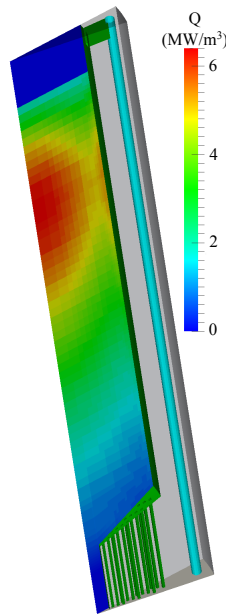


Figure 4.10: Overview of HTR-PM geometric model including the power density Q in the pebble bed.

(Struth, 1995; Lei et al., 2004), one of the most widely used codes in the past two decades for pebble bed reactors (Haque et al., 2006; Boer et al., 2010; Zheng et al., 2009).

4.4.1 Description of the HTR-PM model

The geometric model used for the pebFoam calculation consists of a 12° wedge ($1/30^{\text{th}}$) of the HTR-PM, surrounding one coolant channel in the reflector. It contains the pebble bed, including the cone-shaped bottom reflector and pebble discharge tube. Surrounding the bed is the graphite reflector from $r = 1.5$ m to $r = 2.25$ m with an 18 cm diameter coolant channel at $r = 2$ m. At the top of the bed is the helium void space. For simplicity, surrounding structural parts such as top reflector, bottom carbon bricks and the reactor pressure vessel were not included in the model. The pebble bed had a radius of 1.5 m, with its top located at $z = 0$ m. The cone-shaped bottom narrowed from $z = 10.71$ m towards the 0.25 m radius pebble discharge tube at $z = 11.43$ m. An overview of the geometric model used in the calculations is in Figure 4.10, with the coolant flow path highlighted, and in grey background the graphite reflector. Also shown is the power density inside the pebble bed, which is the same as was used in THERMIX.

The mesh used for most of the pebble bed had cell height $\Delta z = 20$ cm and a cell width

of $\Delta r = 10$ cm. Towards the wall smaller cells were used narrowing to $\Delta r = 0.897$ cm at the reflector wall. In angular direction one cell was used in the central part of the bed, refining towards the wall, using 6 cells in angular direction at the wall. The total mesh size of the fluid phase was 4641 cells. The reflector also used a cell height of $\Delta z = 20$ cm. Cells widths Δx and Δy were mostly around 5 cm to follow the cylindrical shape of the coolant channel through the reflector. The total number of cells used for the solid reflector region was 15738 cells. The mesh was created with the OpenFOAM blockMesh utility using hexes. Although no true mesh convergence study was performed, calculations with mesh cells double and triple the size in the near-wall region resulted in differences in calculated temperatures and velocities of less than 0.05%, giving confidence the mesh quality was sufficient.

In THERMIX the pebble bed is usually modelled as a simple cylinder with flat ends ignoring the cone shape at the bottom, as THERMIX is limited to 2D structured r - z meshes. Structural parts not fitting in the r - z geometry, such as the coolant channels in the side reflector, are modelled as a porous zone, using a porosity parameter to describe the volume fraction occupied by the coolant channels. A benefit of THERMIX is that it is relatively simple to include all structural parts of the reactor, such as top and bottom reflectors, core barrel, and pressure vessel. For an example of the THERMIX model see Zheng et al. (2009).

As the THERMIX calculations were not performed by ourselves, but results were provided by Yanhua Zheng, several differences exist between the geometric models of pebFoam and THERMIX. First, the geometric model used by THERMIX included a much larger part of the reactor, extending further above, below and to the side of the model used in pebFoam. However, most of these outlying parts have little effect on what happens inside the core during normal operations, and thus could easily be left out when using proper boundary conditions. As heat losses in the axial direction are relatively low in a HTR-PM, zero gradient temperature boundary conditions were used at the top and bottom of the pebFoam geometry. In radial direction, during normal operation, reflector temperatures on the outside of the coolant channels in the reflector are close to 250 °C, and the outside of the reflector is surrounded by a helium gap connected to the helium inflow, which allowed us to use a fixed temperature boundary condition of 250 °C at $r = 2.25$ cm.

In THERMIX, directly below the core at $11 < z < 12.4$ m for the full width of the core is a porous bottom reflector. Through the reflector helium flows down out of the core into the hot helium plenum at $12.4 < z < 13.2$ m, from which it exits the core model. In pebFoam, the cone-shaped reflector at the bottom and the pebble discharge tube are modelled explicitly, together with outflow channels through the bottom reflector in the region $0.3 < r < 1.35$ m. As we could not find detailed information on the geometry of these channels, we have chosen to model them similar as in the HTR-10 (IAEA, 2000), where the porous outflow region channels did not extend all the way to the side of the reflector. The volume, pressure drop relation, and heat exchange with the reflector of the channels were chosen to be similar to the porous outflow region of THERMIX. In the

pebFoam model, the pebble discharge tube and porous graphite region below the pebble bed extend to $z = 13$ m, where the helium flows out of the model in vertical direction. As during normal operation there is a strong helium flow, ignoring the hot helium plenum at the bottom will not have a significant effect on temperatures in the upwind flow direction.

Finally the THERMIX model includes a leakage flow through the reflector at $1.556 < r < 1.69$ m and a control rod region at $1.77 < r < 1.85$, both of which are modelled as porous regions in the reflector through which helium flows from the top of the core to the bottom helium plenum, cooling the reflector. To compensate for these leakage flows, the total flow rate in pebFoam was lowered to 92.4 kg/s to have an identical mass flow rate through the pebble bed as in THERMIX.

As in the SANA calculations, the pebFoam calculations were performed for both a uniform and a nonuniform porosity distribution. In the uniform case, a porosity of $\phi = 0.390$ was used throughout the whole pebble bed region, identical to THERMIX. For the nonuniform porosity distribution, with a computational tool we generated a pebble bed with HTR-PM dimensions including the pebble discharge tube and the cone-shaped bottom, containing 100,000 pebbles. The porosities of this bed were calculated in the near-wall regions: within 3 cm of the reflector wall; within 3 cm of the cone-shaped bottom; and within 3 cm of the wall of the discharge tube. The resulting porosities were $\phi = 0.474$ at the reflector wall from $1.47 < r < 1.5$ m, $\phi = .500$ in the 3 cm above the cone, and $\phi = .502$ at the wall of the pebble discharge tube from $0.22 < r < 0.25$ m. In the nonuniform model, porosities within 3 cm of the walls were set to these values, and the porosity of the bulk of the bed was changed to $\phi = 0.386$ to maintain an average porosity of 0.39.

As was mentioned before, the power density was taken from the input of the THERMIX calculations and is shown in Figure 4.10. It was calculated using VSOP99 (Rütten and Haas, 2003) for the THERMIX geometry with a uniform porosity of 0.39 by Zheng Yanhua and made available to us. For the nonuniform porosity distribution we scaled the power density with the porosity by first multiplying the power density with the nonuniform porosity and then normalising. Given the large migration length of neutrons in pebble bed reactions, on the order of 50 cm, the neutron flux is hardly affected by local changes in porosity (Auwerda et al., 2010b). As such, the error introduced in power density for the nonuniform porosity distribution by not recalculating the flux will be relatively small.

4.4.2 Calculation results for the HTR-PM model

The solid temperature distribution for the uniform and nonuniform pebFoam calculations on the intersection plane through the centre of the geometry are shown in Figure 4.11, together with results from THERMIX. A fairly rough colour distribution for the temperatures was chosen to better show the iso-temperature lines and make it easier to compare the three cases. The white lines outline the location of the coolant channel, upper helium plenum, and pebble bed.

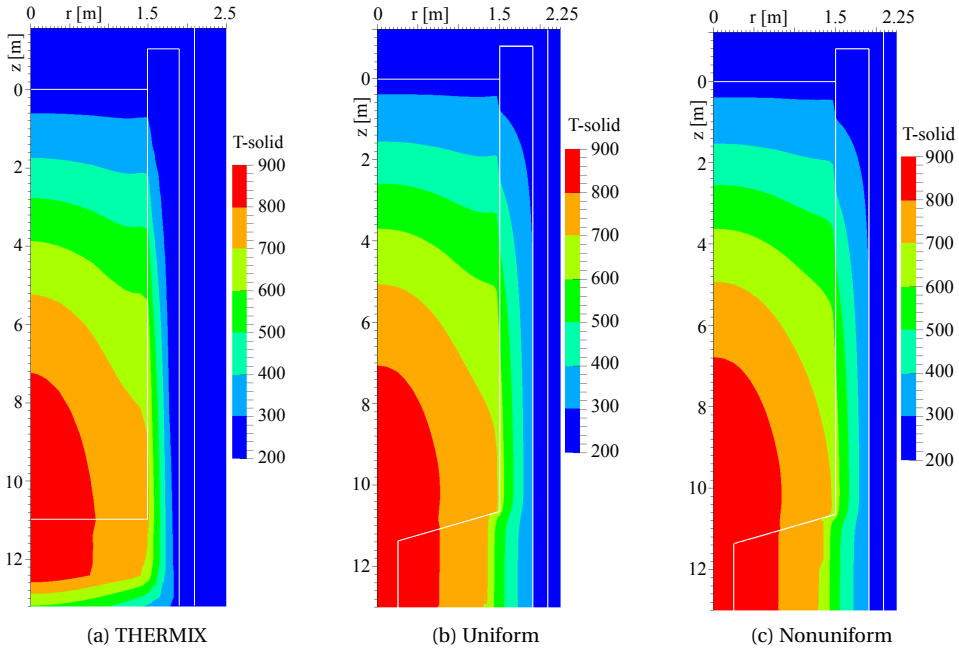


Figure 4.11: Solid temperature distribution in °C as calculated by THERMIX, and by pebFoam using a uniform and nonuniform porosity distribution. The white lines outline the location of the coolant channel, upper helium plenum, and pebble bed.

Although the temperature distributions are very similar, there are some differences, most caused by differences in the geometric models. First, the temperature distribution of THERMIX drops near the bottom of the geometry, while for the pebFoam calculations it remains nearly constant due to the difference in model of the outflow region. In THERMIX the helium is collected and leaves the geometry in this region with little heat transfer to the graphite, while in pebFoam helium flows out of the calculation domain at $z = 13$ m, with a zero-gradient temperature boundary condition. Additionally, as there are no outflow channels in pebFoam for $r > 1.35$ m, no hot helium flows through the bottom reflector between $1.35 < r < 1.5$ m, resulting in lower temperatures in this region than in THERMIX where the porous reflector region extends to $r = 1.5$ m. The inclusion of the pebble discharge tube at the bottom of the core in the pebFoam model had little effect on flow patterns, as although the flow speed in the channels through the bottom reflector is much higher than through the bed, the effective porosity in this region is much lower than in the bed, resulting in similar flow rates through the reflector as through the discharge tube.

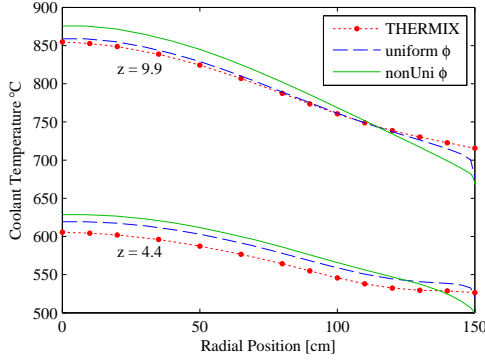


Figure 4.12: Radial coolant temperature profiles at $z = 4.4$ and $z = 9.9$ m calculated by THERMIX and by pebFoam with uniform and nonuniform porosity distribution.

In THERMIX there is a stronger temperature gradient in the reflector region between the core and coolant channel at $1.5 < r < 1.91$ m than in pebFoam for the entire core length. This is caused by the flow of cold helium through the leakage channel and control rod channel in THERMIX, cooling the reflector in this region, which is absent in the pebFoam model. This also results in increased heat transfer in pebFoam to the helium flowing through the coolant channel, causing an 8 °C increase of the helium temperature at the top of the pebble bed at $z = 0$ m compared to THERMIX, observable as a small shift of the iso-temperature lines in Figures 4.11b and 4.11c towards the top of the bed.

To investigate the small differences visible in Figure 4.11 in the shape of the temperature profiles inside the pebble bed, especially near the reflector wall and for the nonuniform bed, the radial coolant temperature profiles for the three cases are shown in Figure 4.12 at $z = 4.4$ m just below the peak in power density, and at $z = 9.9$ m near the cone-shaped bottom of the pebble bed. The axial coolant velocity u_z at $z = 4.4$ m is shown in Figure 4.13.

In general there is a good match between the calculated temperature profiles, especially between the results from pebFoam with a uniform porosity and THERMIX, but there are some differences. First, the temperatures at $z = 4.4$ m for both pebFoam cases are slightly higher than for THERMIX, 12 °C for the uniform case at $r = 0$, as a result of the higher temperature of the coolant flowing into the bed at the top of the core. This also causes the higher coolant velocity in Figure 4.13 for the uniform porosity case, as the helium density is lower and mass flow is the same. The temperature profile for the uniform porosity case at $z = 4.4$ m has an almost identical shape to the one calculated by THERMIX, except very close to the wall at $r = 1.5$ m. Here the temperature drops slightly for pebFoam, as in pebFoam heat transfer from the coolant to the reflector wall is included while in THERMIX there is only heat transfer from the pebbles to the reflector. At $z = 9.9$ m, due to the higher heat transfer to the wall, the pebFoam uniform temperature profile lies very

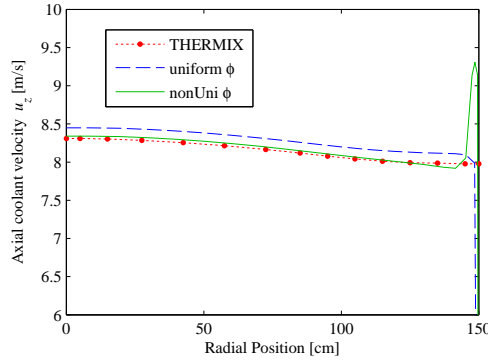


Figure 4.13: Axial coolant velocity profiles at $z = 4.4$ m as calculated by THERMIX, and by pebFoam using a uniform and nonuniform porosity distribution.

close to the one from THERMIX for most of the bed, except closer to the wall where it is 22 °C lower.

The temperature and velocity profiles from pebFoam with a nonuniform porosity differ more significantly from those of THERMIX and also from the uniform case. The lower porosity near the wall results in an increased coolant velocity at the wall, 1.3 m/s higher than for the uniform case, and slightly lower velocities through the rest of the bed, 0.02 m/s lower than for the uniform case, see Figure 4.13. This results in a lower coolant temperature near the wall where mass flow is increased, and higher temperatures towards the centre of the bed where there is a lower mass flow, see Figure 4.12. Further down in the core at $z = 9.9$ this effect is more pronounced, causing even lower temperatures in the near wall region and significantly higher temperatures towards the centre, 20 °C lower at the wall and almost 20 °C higher at the centre than for the uniform porosity case.

4.5 Discussion and Conclusions

This paper describes a new thermal-hydraulics model for pebble beds based on turbulence modelling for porous media. All space-time fluctuations filtered out in the averaging process are included in its definition of the kinetic energy k , and when the porosity goes to unity (non-porous flow) the model becomes identical to the classical k - ϵ model, allowing easy calculation of flows near pebble bed interfaces. The model was implemented in OpenFOAM resulting in the pebFoam solver, supporting 3D unstructured meshes of arbitrary shapes and sizes and capable of handling complicated geometries.

To test pebFoam, calculation results for two different SANA experiments, the first with a completely filled pebble bed and the second with a partially filled bed with a cavity on top, were compared with measurement data. Additionally results for a 3D wedge of the

HTR-PM were compared with results from 2D THERMIX calculations. To better study the effects of the porosity distribution in the pebble bed and of the lower porosities near the walls, for both SANA and the HTR-PM porosity distributions were derived from a computer generated pebble bed, and calculations were performed using both a uniform averaged porosity value and a more detailed nonuniform porosity distribution including porosity variations near the boundaries of the bed.

Results for pebFoam agreed well with both the measurements of the SANA experiments and with the THERMIX calculations, showing its capability to accurately calculate flow and temperature distributions for both natural circulation and under full power forced convection conditions. The simulation of the partially filled bed with a cavity on top, in which relatively strong natural circulation developed in the cavity, showed the capability of the model to simulate the interface between pebble bed and cavity, where the top surface of the bed interacts with the flow in the cavity above. Additionally, the HTR-PM calculations demonstrated the 3D capabilities of the code, including complicated structures such as the coolant channel in the reflector and the cone-shaped bottom of the pebble bed.

Although the SANA experiments were performed under atmospheric pressure, previous studies have already shown that natural circulation plays a significant role in the resulting temperature distributions. This was confirmed by the calculations with pebFoam, as the results for the nonuniform porosity distribution, in which natural circulation was enhanced due to the lower porosities near the walls, agreed better with experimental results than results for a uniform porosity distributions. This also confirmed previous observations in literature that the nonuniform porosity distribution has a significant effect on heat transfer under natural circulation due to the wall-channelling effect (Stöcker, 1998; Bader et al., 2011).

Comparison of the HTR-PM calculations for uniform and nonuniform porosity distributions demonstrated that also for full power operating conditions the porosity distribution can have a small but significant effect on the resulting temperature distribution, as the nonuniform porosity distribution with lower porosities near the walls resulted in higher mass flow near the wall and lower flow through the bed than for the uniform distribution, leading to lower temperatures near the wall and 20 °C higher temperatures towards the centre of the bed. Although this indicates the lower porosity near the walls results in higher fuel temperatures, the SANA experiments showed that wall-channelling of the flow also increases natural circulation and could result in lower pebble temperatures during accident scenarios.

EFFECTS OF NON-UNIFORM POROSITY DISTRIBUTIONS IN COUPLED STEADY STATE AND TRANSIENT ANALYSIS

In the previous chapter we have seen that wall-channelling of the flow increased the heat transfer due to natural circulation in the SANA experiments, see Figure 4.4. This wall-channelling is caused by the higher porosity near the wall of a randomly packed bed, resulting in lower flow resistance and thus higher fluid velocities near the wall. In Section 2.7 we found that the porosity in the bulk region of a randomly packed bed is not uniform but fluctuates, see Figure 2.12. As a result clusters of pebbles can have a higher or lower porosity, which might affect the local power density, coolant flow and temperature distribution, possibly resulting in hotspots.

In this chapter we investigate the effect of both the wall-channelling and the local porosity fluctuations on the power density, flow and heat transfer in a pebble bed high temperature reactor. To perform the calculations, the pebFoam thermal-hydraulics code described in the previous chapter was coupled to the PHANTOM neutron transport code. Three different porosity distributions in the pebble bed were investigated. The first one is a uniform porosity distribution. The second distribution has a higher porosity near the walls and the top of the bed to investigate the effect of wall-channelling. The third has both higher porosities near the walls and a lower porosity at the point of maximum power production to investigate the effect of a densely packed cluster of pebbles.

The steady state power and temperature distributions were calculated for a 3D quarter core model of the HTR-PM and compared for the three porosity distributions. Besides

the steady state normal operation case, the pressurised and the depressurised loss of forced cooling (PLOFC and DLOFC) transients were investigated. The depressurised loss of forced cooling transient was chosen because it is the most demanding transient for pebble bed HTRs, during which the highest fuel temperatures are reached (Kugeler and Schulten, 1989). As such, it is the most important transient to show the passive safety feature of a pebble bed reactor. Densely packed clusters might cause hotspots here. During a DLOFC, the coolant density is low and the effect of natural circulation is almost negligible. On the other hand, during a pressurised loss of cooling transient natural convection of helium through the pebble bed is a very important part of the heat transfer (Boer et al., 2010; Zheng et al., 2009). This makes the PLOFC transient a good candidate to investigate the possible increase of natural convection due to wall-channelling.

5.1 The coupled calculation scheme

Similar to Boer (2008), our coupled calculation scheme consists of two parts. The first part determines the equilibrium core composition of the pebble bed and generates the nuclear data used for the steady state and transient analysis. The second part, the pebFoam-PHANTOM coupled code system, consists of a WRAPPER program, which calls pebFoam and PHANTOM to perform the thermal-hydraulic and neutronic analysis, and handles the data transfer between the two programs.

5.1.1 Equilibrium core composition calculation

In pebble bed reactors, pebbles usually travel multiple times through the core before being discarded, increasing their burnup with every pass. Each time a pebble is taken out at the bottom of the core, its burnup is measured. If the burnup is below a certain threshold, the pebble is put back at the top of the core. Else, the pebble is discarded and a fresh pebble is added to the core. As a result, the core will contain a mixture of pebbles at various burnup stages with burnup changing over the core height.

To determine the equilibrium core composition of the pebble bed, we implemented a core depletion scheme in MATLAB (The MathWorks Inc., 2012) based on the work of Wols et al. (2014) and Boer (2008); Boer et al. (2009). Generation of homogenised cross sections and collapsing of cross sections is handled as described in Section 3.3 using SCALE-6 (SCALE-6, 2009) routines. The burnup calculations are performed with the ORIGIN SCALE-6 routine. The DALTON diffusion code (Boer et al., 2009) calculates the reactivity, neutron flux and power distribution.

The scheme consists of an iterative procedure, see Figure 5.1. First, initial homogenised core cross sections are generated using the nuclide composition of fresh pebbles. Next, DALTON uses these cross sections to calculate an initial guess for the flux and power distribution. The core is divided into N_{ax} 50 cm high axial zones. For every pass of the pebble through the core, the scheme follows the pebble through each axial zone, and

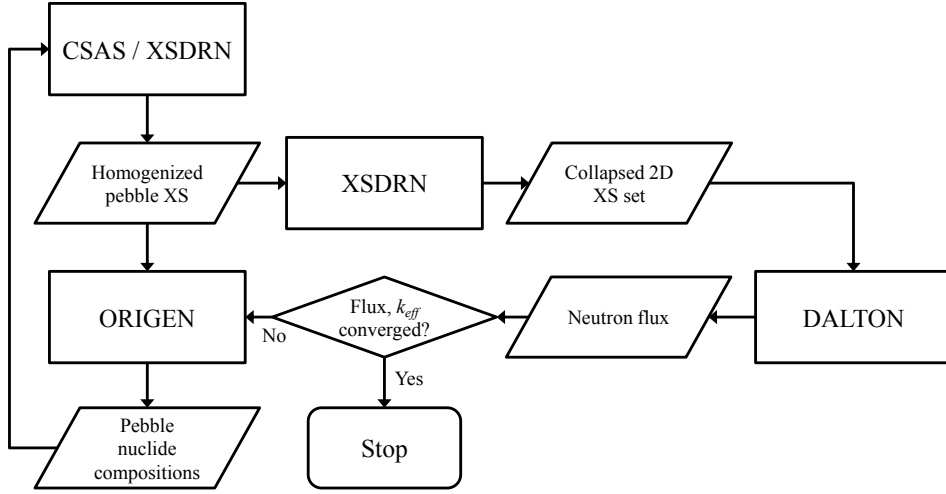


Figure 5.1: Calculation scheme to determine the equilibrium core composition.

in each zone depletes the fuel in the pebble using the local power and flux spectrum from DALTON. The residence time of the pebble in each zone is calculated from the total number of pebbles in the core, the total power, and the target burnup of the pebbles. This results for every axial zone in N_{pass} pebble compositions, one for each pass. For each zone, the N_{pass} pebble compositions are mixed to create the homogenised collapsed cross sections. These cross sections are used by DALTON to calculate a new flux guess, and as background cross sections when creating the individual collapsed pebble cross section sets from the pebble nuclide compositions. This process is repeated until the flux and k_{eff} are converged and a steady state is reached.

Once the equilibrium core composition has been determined, a temperature dependent collapsed cross section library is created. This library contains macroscopic cross section sets for every material zone in the coupled calculation at multiple temperatures. For the zones containing fissile material, the library also includes temperature dependent collapsed microscopic ^{135}Xe cross sections. This cross section library is used as input for the second part of the coupled calculation scheme.

5.1.2 The pebFoam-PHANTOM coupled code system

Several others have used coupled code systems to analyse pebble bed HTR transients. These coupled code systems all consist of a thermal-hydraulics code to calculate flow and heat transfer, and a neutronics code (diffusion or transport) to calculate the flux distribution from which the power density distribution is derived. Often the THERMIX 2D thermal-hydraulics code is used to calculate the flow and heat transfer, see for example

5. Effects of non-uniform porosity distributions in coupled steady state and transient analysis

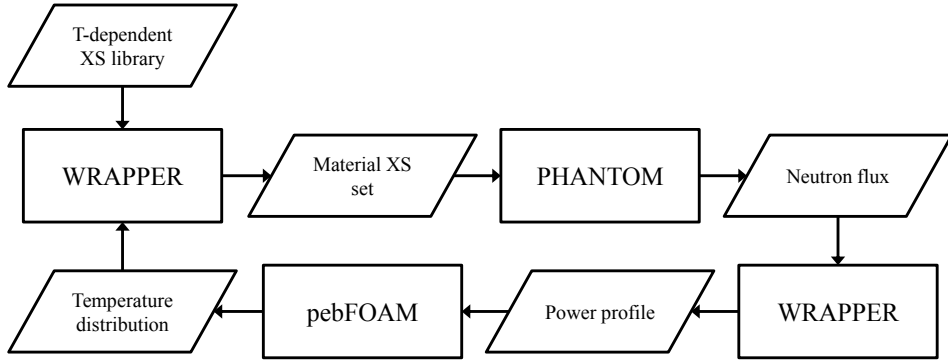


Figure 5.2: Schematic overview of the pebFoam-PHANTOM coupled code system.

PANTHERMIX (Oppe et al., 1998), NEM(DORT-TD)-THERMIX (Tyobeka et al., 2007), PEBBED-THERMIX(KONVEK) (Gougar et al., 2010) and PARCS-THERMIX (Downar et al., 2002). Boer (2008) coupled THERMIX to the DALTON diffusion code to investigate PLOFC, DLOFC and control rod withdrawal (CRW) transients for the AVR (Ding et al., 2009), the HTR-10 and the PBMR (Boer et al., 2010). Zheng et al. (2009) used THERMIX together with VSOP (Rütten and Haas, 2003) to investigate PLOFC and DLOFC transients in the HTR-PM, and used the TINTE (Gerwin et al., 1989) code system to investigate a water ingress transient (Zheng et al., 2010). More recently, Seubert et al. (2012) developed the ATTICA3D thermal-hydraulics code and coupled it to the TORT-TD neutron transport code, resulting in a code system with both 3D thermal-hydraulics and neutron transport functionality, although limited to structured grids.

To be able to use the pebFoam thermal-hydraulics code described in the previous chapter for coupled transient calculations, we coupled pebFoam to the PHANTOM neutron transport code. As both codes support 3D unstructured meshes, the resulting pebFoam-PHANTOM coupled code system has no restrictions to the geometries it can handle. This makes it capable of handling for example the cone-shaped bottom of the pebble bed, the cylindrical coolant holes in the reflector, and the noses holding the control rods in the AVR (Krüger, 1989).

Similar to Boer et al. (2009), the pebFoam-PHANTOM coupled code system is driven by a WRAPPER program, which handles the data transfer and calls the thermal-hydraulics and neutronics codes, see Figure 5.2. The three parts of the code system, the PHANTOM neutron transport code, the pebFoam thermal-hydraulics code, and the WRAPPER program, are described below.

PHANTOM

The PHANTOM neutron transport code uses spherical harmonics for the angular discretisation of the neutron flux. Geometric discretisation is done using finite elements, supporting 3D unstructured meshes. In the coupled calculation, PHANTOM calculates the spatial flux distribution and the fission power per element using neutron cross sections obtained from the WRAPPER program based on the local temperatures and ^{135}Xe concentrations.

pebFoam

The pebFoam thermal-hydraulics code is described in detail in Chapter 4. It is implemented in the open source OpenFOAM framework (OpenFOAM Foundation, 2012), which uses finite volume discretisation and supports 3D unstructured meshes. PebFoam uses a porous turbulence model to calculate the fluid flow and heat transfer inside the pebble bed. The effective pebble-bed thermal conductivity is modelled according to the Zehner-Bauer-Schlünder correlation (Zehner and Schlünder, 1972; Breitbach and Barthels, 1980; IAEA, 2000), and correlations for the graphite and helium material properties are taken from THERMIX (Struth, 1995). Radiative heat transfer through void spaces such as the cold helium plenum and coolant channels is included. In the coupled calculation, pebFoam calculates the helium flow field and the solid and helium temperature distributions using the power density distribution Q obtained from the WRAPPER program.

WRAPPER

The WRAPPER program consists of a collection of scripts written in the Python programming language (van Rossum, 1995). First, it handles program control, calling pebFoam and PHANTOM in turn, each time creating new control files to advance the time step. Second, it handles data transfer between pebFoam and PHANTOM. When PHANTOM is finished, it reads the power density for each element from PHANTOM, converts these to the power density for each volume element for pebFoam, and scales the power density distribution to the reactor power given at input. When pebFoam is finished, the WRAPPER program reads the temperatures for each volume element from pebFoam and calculates the average solid temperature for each PHANTOM material zone. It also uses the power density for each element together with the material cross sections to calculate the ^{135}Xe concentrations for each zone. It then uses the ICE routine from SCALE to create new cross sections for each PHANTOM material zone at the proper temperature and ^{135}Xe concentration from the cross section library.

5.2 The HTR-PM geometry

Simulations were performed for a 3D quarter core model of the Chinese 250 MW_{th} High Temperature Reactor Pebble bed Modular (HTR-PM) (Zhang et al., 2009). The HTR-PM

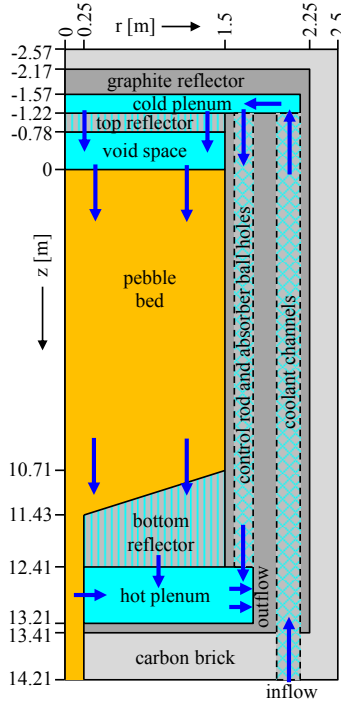


Figure 5.3: Schematic overview of a r - z projection of the HTR-PM geometry (not to scale). The blue arrows show the helium flow direction during normal operation. Helium flows into the reactor at the bottom of the coolant channels at 250 °C, and flows out of the reactor from the hot helium plenum at 750 °C.

design has a 3 m diameter pebble bed with an effective height of 11 m, containing 420,000 pebbles. Each pebble contains 7 g uranium with a 8.9% enrichment in 10,000 TRISO particles. The pebbles pass on average 15 times through the core before being discarded, reaching a target burnup of 90,000 GWd/tU. The reactor is cooled with helium at 70 bars, with an inlet temperature of 250 °C and outlet temperature of 750 °C.

Details for the geometry were taken from IAEA (2000); Zheng and Shi (2008); Zheng et al. (2009) and private communications with prof. Zheng Yanhua from INET, Tsinghua University. Figure 5.3 shows a schematic overview of a 2D r - z projection of the HTR-PM geometry. Similar to Zheng et al. (2009) we chose the origin of the z -axis at the top of the pebble bed, with positive direction down towards the bottom of the bed.

The cone-shaped bottom of the pebble bed has a 30 degrees angle, narrowing to the 0.5 m diameter pebble discharge tube. Above the pebble bed and below the porous top reflector is a 78 cm void space. The bed is surrounded by a graphite reflector with an

outer radius of 2.25 m. Situated at a radial position of $r = 1.65$ m inside the reflector, are eight 13 cm diameter control rod channels and 22 small absorber ball holes. Around the graphite reflector is a layer of carbon brick, extending from $z = -2.572$ m to $z = 14.208$ m, with an outer radius of $r = 2.5$ m. Cold helium of 250 °C enters the core at the bottom and flows up through 30 coolant channels with a diameter of 18 cm, equidistantly placed at $r = 200$ cm in the graphite reflector. The cold helium is collected at the top of the core in the cold helium plenum situated inside the graphite reflector between $z = -1.567$ m and $z = -1.217$ m. From this plenum, the helium flows down through channels in the 43.7 cm thick porous top reflector and through the pebble bed. After exiting the pebble bed and flowing through the cone-shaped porous bottom reflector, the helium is collected below the core in the hot helium plenum, situated between $z = 12.408$ m and $z = 13.208$ m. From there the hot helium exits the core in the radial direction with an outlet temperature of 750 °C.

5.2.1 Geometric model

The geometric model consists of a 3D quarter core with symmetric boundary conditions at the $x = 0$ and $y = 0$ boundaries, see Figure 5.4. As both PHANTOM and OpenFOAM support 3D unstructured meshes, many geometric details can be included. The model includes the cylindrical coolant channels in the side reflector through which the cold helium flows upwards. Also included are the control rod channels and small absorber ball holes, connecting the upper cold helium plenum with the hot helium plenum below the bottom reflector. Coolant can flow through these channels, bypassing the core. Zheng and Shi (2008) report that 1% of the total mass flow flows through the control rod tubes, and the maximum bypass flow through gaps between the graphite components is 4% of the total flow rate. In most studies (Zheng and Shi, 2008; Zheng et al., 2012) this leakage flow is modelled to flow through the reflector area containing the control rods and small absorber ball holes. Similarly, we scaled the pressure drop over the control rod channels and small absorber ball holes to let 5% of the flow rate flow through them.

The top and bottom porous reflectors of the HTR-PM contain many small channels through which the helium flows. To model these, we would need an extremely fine mesh in these regions. We created wider channels through the top and bottom reflector, so only axial flow is allowed in these regions without the need to refine the mesh. These channels are modelled as porous regions and their porosities were set so the top and bottom reflectors had the correct total porosity, 14% for the top and 9% for the bottom reflector. Heat transfer and pressure drop were also modelled to be similar to channels of the reported diameter, 8 cm for the top and 2 cm for the bottom reflector.

5.2.2 Pebble bed porosity distributions

To investigate the effects of non-uniformities on the temperature distribution during transients, three different porosity distributions are compared. The first porosity distribution,

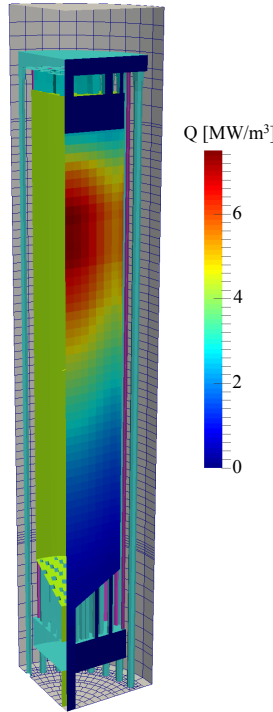


Figure 5.4: The 3D quarter core HTR-PM geometric model used in the calculations with the steady state power density distribution Q inside the pebble bed. The pebble bed-reflector interface is shown in green. The coolant channels through the reflector, cold helium plenum, channels through top reflector, channels through bottom reflector, and hot helium plenum are shown in cyan. The control rod and absorber ball channels are shown in purple. The surrounding graphite reflector and carbon brick outer boundary is shown in grey.

called uniPor, is a uniform porosity distribution, with is almost always used in pebble-bed calculations. The second distribution, the wallPor distribution, takes into account that in a randomly stacked bed porosities near the walls of the bed are higher than in the bulk of the bed, see Chapter 2. The third porosity distribution, localPor, includes a densely packed cluster in the centre of the bed at the location where the maximum temperature is reached during the DLOFC transient.

In literature, almost exclusively a uniform porosity of 0.39 is used for all pebble bed designs, from the smaller HTR-10 (27,000 pebbles) and AVR (100,000 pebbles) to the larger HTR-PM (420,000 pebbles) and PMBR (452,000 pebbles) (Jing et al., 2002; Krüger, 1989; Reitsma et al., 2006). But in a randomly packed bed, the porosity near the walls is

lower than in the bulk of the bed, see Chapter 2. Thus, it seems likely that the average porosity of a large bed such as the HTR-PM is smaller than of a smaller bed such as the HTR-10, as there is relatively more bulk volume away from the walls.

To verify this, we generated a randomly stacked pebble bed with the HTR-10 geometry, with a radius of 0.9 m and a 30 degrees cone at the bottom containing 27,000 pebbles, using the program described in Section 2.3. The average porosities of three different boundary zones were calculated. The first zone is the zone within 3 cm of the radial reflector wall, between $r = 0.87$ and $r = 0.9$. The second zone is at the bottom of the bed within 3 cm the cone-shaped bottom reflector. The third zone is the top 6 cm of the bed. The average porosity in the region within 3 cm of the radial wall was 0.483. The porosity near the cone-shaped bottom was 0.508 and in the top 6 cm 0.694. The bulk porosity away from the walls was 0.369, resulting in the average uniform porosity of 0.390 stated in literature (Jing et al., 2002).

For the HTR-PM geometry we also generated a randomly stacked bed, with a radius of 1.5 m, narrowing at the bottom with a 30 degrees cone to a 0.5 m diameter pebble discharge tube. As generating a bed containing all 420,000 pebbles in the HTR-PM would take far too much time, we used 67,500 pebbles, resulting in a bed of roughly 2 meters high. Although smaller than the 11 meter high HTR-PM, the bed was sufficiently large to get reliable average porosity values for the various regions. The porosity within 3 cm of the radial wall was 0.474, the porosity within 3 cm of the bottom of the cone was 0.500, and the porosity of the top 6 cm of the bed was 0.692. The porosity of the bulk of the bed was 0.370. We also determined that the porosity within 3 cm of the wall of the pebble discharge tube was 0.502.

The porosity near the wall of the 1.5 m radius HTR-PM geometry is lower than the 0.9 m radius HTR-10 geometry due to the difference in wall curvature. If the radius of the wall is larger, the wall more closely resembles a flat surface, and the stacking at the wall can more closely resemble perfect hexagonal layers, resulting in a lower porosity. The porosity values of 0.37 and lower for the bulk are in line with other values found earlier. In Table 2.1 a porosity of 0.3685 is given for the bulk of the bed more than five pebble diameters away from a wall, and in Section 4.3.1 we found a porosity of 0.3681 for the zone of the bed at least 3 cm away from a wall.

To create the wallPor distribution we used the values found of the 1.5 m radius HTR-PM geometry: a porosity of 0.692 for the top 6 cm of the bed; a porosity of 0.474 for the zone within 3 cm of the radial reflector; a porosity of 0.500 for the zone within 3 cm of the cone shaped bottom; a porosity of 0.502 for the zone within 3 cm of the wall of the tube; and a porosity of 0.370 for the bulk of the bed. For the uniPor distribution, the average porosity for the entire HTR-PM using the values in the wallPor distribution was determined, resulting in a porosity of 0.376, much lower than the 0.39 used in literature.

The localPor distribution has the same porosities at the boundaries and bulk as the wallPor distribution. In Section 2.7 we saw significant variation in porosity values for

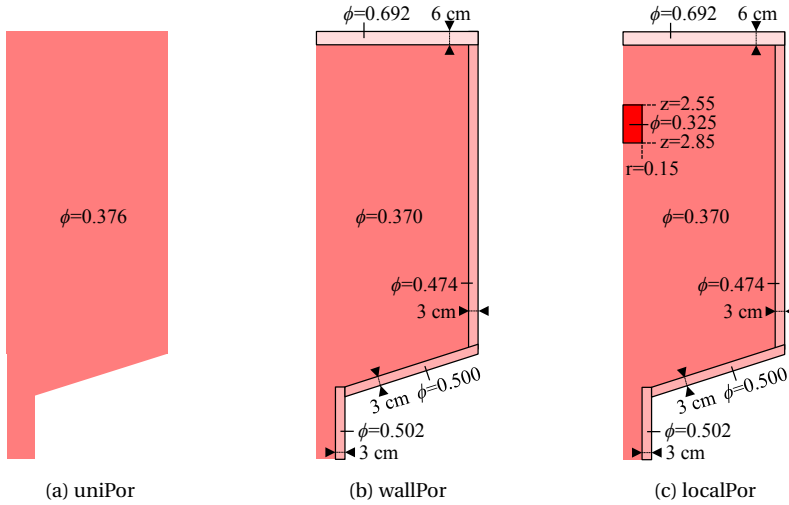


Figure 5.5: 2D r - z projection of the three investigated porosity distributions for the pebble bed. For each zone the porosity ϕ is indicated.

small clusters of pebbles throughout the bulk of the bed. For clusters with a diameter of 5 pebble diameters 0.5% of all clusters away from the wall had a porosity of 0.325 or smaller, see Figure 2.12. For larger clusters of 7.5 pebble diameters less than 0.01% of the clusters had a porosity smaller than 0.325. For even larger clusters of 10 pebble diameters, no clusters with a porosity < 0.34 were found. The porosity was set to 0.325 in a cylindrical zone with a height and diameter of 30 cm, 5 pebble diameters. The centre of this cylinder was at $r = 0$ and $z = 2.7$ m from the top of the bed, around the peak power density, where the maximum temperature is reached during the DLOFC transient. Figure 5.5 shows a schematic overview of the three porosity distributions.

5.3 Coupled steady state calculations

The steady state power density and temperature distributions were calculated for the three porosity distributions with the coupled pebFoam-PHANTOM calculation scheme using the 3D quarter core geometric model described in the previous section. In PHANTOM, vacuum boundary conditions for the flux were used at the outer boundaries of the carbon brick. In pebFoam, adiabatic boundary conditions were set for the top and bottom of the geometry, at $z = -2.572$ m and $z = 14.208$ m. Due to the relatively tall height of the HTR-PM compared to its diameter, and as the HTR-PM design includes insulation layers at the top and bottom, this is a minor simplification. At the outer radial boundary of the carbon brick, at $r = 2.5$ m, the temperature boundary condition was set to a fixed temperature

of $T = 250\text{ }^{\circ}\text{C}$. In the HTR-PM design, the carbon brick is surrounded by a helium layer, which is kept at $250\text{ }^{\circ}\text{C}$ during normal operation. The helium inflow temperature was set to $250\text{ }^{\circ}\text{C}$ and the helium mass flow to 26.5 kg/s , one quarter of the full-core 96 kg/s for the HTR-PM design. The pressure at the outflow was set to 70 bars .

5.3.1 Results

Although calculations were done for a 3D quarter core model, for clarity results are shown on 2D planes or 1D lines through the geometry. A 2D projection of the calculated steady state power density profile Q for the uniPor distribution is shown in Figure 5.4. The power peak occurs in the upper part of the pebble bed, at $z = 2.7\text{ m}$ from the top of the bed, as here pebbles have a lower burnup than further down. The steady state solid temperature distribution on a 2D plane at $x = 0$ through the HTR-PM is shown in Figure 5.6 for the uniPor distribution. The maximum fuel temperature occurs at the centre of the core, around $z = 12\text{ m}$ just inside the fuel discharge tube. In the reflector the cold coolant channel between $r = 1.91\text{ m}$ and $r = 2.09\text{ m}$ is visible, as the slice runs through the middle of a coolant channel. Heat flows through the graphite reflector around the coolant channel, explaining the higher reflector temperature on the outside of the coolant channel near the bottom of the core. Hot helium is collected in the bottom plenum between $z = 12.408\text{ m}$ and $z = 13.208\text{ m}$ and flows out of the core in the radial direction at $r = 1.69\text{ m}$ with a temperature of $750\text{ }^{\circ}\text{C}$. Temperatures at the outflow in Figure 5.6 are lower, as the solid temperature here is lower than the helium temperature.

To see the differences between the three different porosity distributions, the radial power density profile $Q(r)$ is shown in Figure 5.7, the radial velocity profile $u_z(r)$ in Figure 5.8a, and the radial fuel temperature profile $T(r)$ in Figure 5.8b, at $z = 2.7\text{ m}$ from the top of the pebble bed. The values are averaged over the 90° angle of the quarter core mesh. Here the power density reaches its peak, and it is through the centre of the densely packed cluster between $z = 2.55\text{ m}$ and $z = 2.85\text{ m}$ in the localPor distribution.

The power density profile of the uniPor distribution peaks at the centre of the bed and lowers towards the wall, but increases again close to the wall due to the extra moderation of the graphite reflector, see Figure 5.7. In contrast, the wallPor distribution has a lower power density next to the wall, as here the porosity is lower and thus the fuel density is lower. In the rest of the bed the power density is slightly higher due to a higher fuel density. The power density profile for the localPor distribution is identical to the wallPor distribution for most of the bed. Only at the location of the densely packed cluster the power density is increased due to the denser pebble packing. As can be seen from the three profiles, the differences in power density follow almost exactly the differences in the packing fraction and thus in fuel density. The neutron flux distribution is hardly affected by the porosity distribution due to the large neutron migration length of around 50 cm in a pebble bed reactor, see Section 3.5.2.

5. Effects of non-uniform porosity distributions in coupled steady state and transient analysis

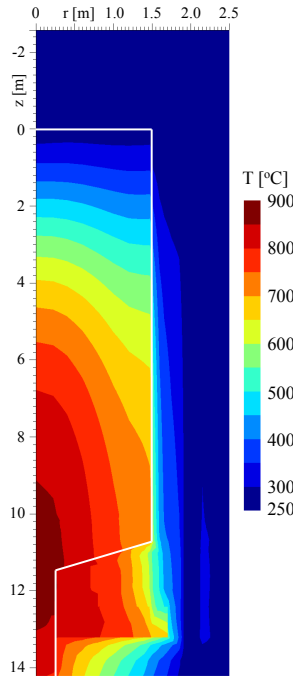


Figure 5.6: Steady state solid temperature distribution for a uniform porosity distribution (uniPor) on a 2D plane through the geometric model. The location of the pebble bed is outlined in white.

The axial coolant velocities u_z shown in Figure 5.8a are phase averaged velocities. To get the volume averaged velocities they have to be multiplied by the porosity. For the uniPor distribution, the velocity is only slightly higher near the centre of the bed than near the wall, as at the centre the temperature is higher and the density is lower. As the porous drag force scales with $\rho^{0.9} u^{1.9}$, see Equation 4.18, the lower coolant density at the centre allows for a slightly higher coolant velocity for the same pressure drop. The velocity profile of the wallPor distribution clearly shows the wall-channelling effect, with a sharp increase in the axial coolant velocity near the wall. As the porosity is also higher near the wall, the increase in the coolant mass flow is even larger. The velocity through the rest of the bed is slightly lower than for the uniPor case, as the total mass flow has to stay the same. The velocity profile of the locaPor distribution is almost identical to that of the wallPor distribution except at the centre. Here the velocity is lower due to the lower porosity and larger flow resistance, resulting in a 20% lower mass flow than for the wallPor distribution. Part of the flow is diverted around the densely packed cluster, resulting in slightly elevated flow velocities between $r = 0.15$ m and $r = 0.5$ m.

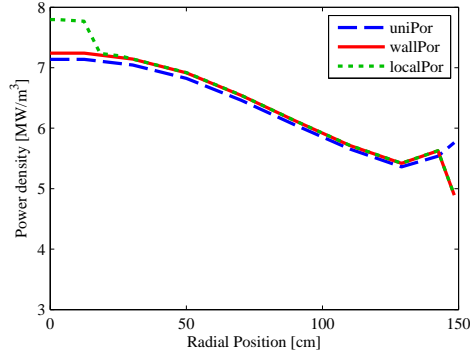


Figure 5.7: Power density profile versus radial position at $z = 2.7$ m from the top of the pebble bed at steady state full power for: uniform porosity distribution (uniPor); lower porosity near the wall (wallPor); low porosity cluster at $z = 2.7$ and $r = 0$ (localPor).

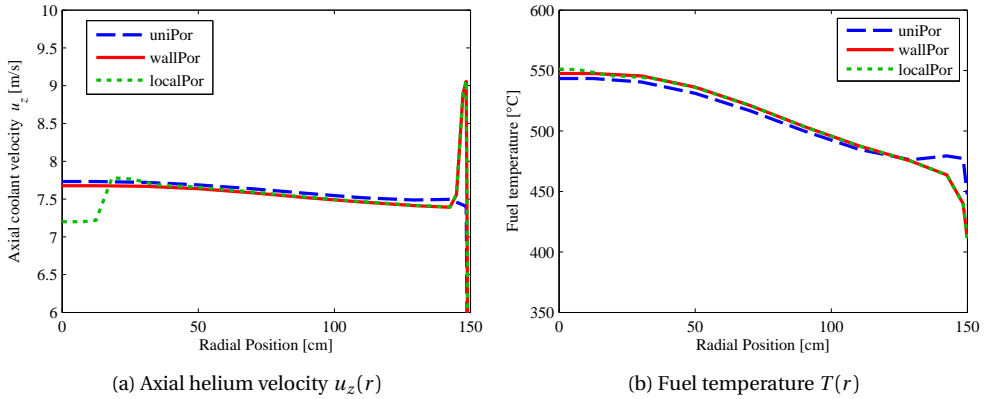


Figure 5.8: Fuel temperature profile and Axial helium velocity profile versus radial position at $z = 2.7$ m from the top of the core for: uniform porosity distribution (uniPor); lower porosity near the wall (wallPor); low porosity cluster at $z = 2.7$ and $r = 0$ (localPor).

The resulting fuel temperature distributions that define the safety of the reactor are shown in Figure 5.8b. For all distributions the temperature near the centre of the bed is higher, as here the power density is higher. For the uniPor distribution, there is a slight rise in the temperature close to the wall due to the increase in power density near the wall. However, the wallPor and localPor distributions show a sharp decrease in the fuel temperature here, as for these distributions the power density is lower and the coolant flow significantly higher at the wall, resulting in a cooler region next to the wall. In the bulk

5. Effects of non-uniform porosity distributions in coupled steady state and transient analysis

of the bed away from the wall, the wallPor and localPor distributions result in a slightly higher fuel temperature than for the uniPor distribution, as here the power density is higher and coolant flow lower. This also results in a higher maximum fuel temperature at the bottom of the core of 886.6 °C for the wallPar distribution, 21.5 °C higher than the 865.1 °C for the uniPor distribution. For the localPor distribution the temperature in the centre of the densely packed cluster is only slightly higher, 3.4 °C, compared to the wallPor distribution. Although the effect on coolant flow and power density is significant, the cluster is too small to cause a significant change in the fuel temperature. As the effect is mostly local, temperatures in the rest of the core are almost identical to the wallPor distribution.

5.3.2 Effect of earthquakes

During an earthquake, the shaking of the reactor could lead to an increase in the pebble bed packing fraction, resulting in an increase of the k_{eff} . To quantify this increase, we need to know the packing fraction values before and after an earthquake.

Scott and Kilgour (1969) made a distinction between random loose and random close packings. They investigated the porosities of cylinders of different sizes, extrapolating results to find the porosity of an infinitely large bed without boundary effects. They found that for random loose packings there is not one fixed porosity, but the porosity depends, among other things, on the method of filling and the pebble friction factors. For carefully filled loosely packed beds using spheres with relatively low friction factors they found an infinite porosity of 0.389. Random close packings were generated by shaking the cylinders either manually or with a mechanical or electromagnetic vibrator. Independent of the method of shaking they found a fixed porosity of 0.3634 for infinitely large randomly close packings.

Similar results were found by Groen (2009) and Baronner (2012) using the PebBEx facility described in Section 2.2. They also found the porosity to depend on the filling method, with carefully filling the bed resulting in a higher porosity. For a bed with a relatively dense packing, filled by quickly pouring the pebbles in the vessel, manually shaking the bed did not cause a noticeable change in porosity. From these results we conclude that an earthquake will not cause the bulk of a randomly packed bed to reach a lower void fraction than 0.3634, and will not cause the packing of a randomly packed bed to change to a regular packing.

In Section 5.2.2 we found for pebble bed reactors a porosity of 0.370 for the bulk region away from the walls, with higher porosities near the boundaries. This indicates a relatively dense packing in a pebble bed reactor, close to that of a shaken bed. Given that the pebbles in a pebble bed reactor are constantly recycled, causing the pebbles to move, such a dense packing seems realistic. Ougouag and Cogliati (2007) investigated the effect of earthquakes on the porosity of a PBMR reactor using a discrete elements method (DEM) to simulate the movement of the pebbles. They found porosities before and after the

Table 5.1: Average porosities, effective pebble bed height, and the change in k_{eff} compared to the uniPor packing for four pebble bed packings. The uniPor packing represents the expected packing density during normal operations. The loose packing corresponds to a conservative limit on the packing density before an earthquake and the shaken packings correspond to expected and conservative packing densities after an earthquake.

Pebble bed packing	Average porosity	Effective pebble bed height [m]	Δk_{eff} [pcm]
Loose	0.3900	11.2498	-228
uniPor	0.3761	11.0000	0
Shaken	0.3696	10.8852	+94
Shaken, ignoring walls	0.3634	10.7797	+199

simulated earthquake of 0.3813 and 0.3727. Although these values seem to indicate higher porosities than the ones we found for the HTR-PM, the PBMR design has an annular core, resulting in a relatively large volume of the bed being close to walls. Taking account of the annular geometry of the PBMR and higher packing fractions near the inner and outer walls, these values also indicate porosities away from the walls close to 0.370 before the earthquake and 0.3634 afterwards.

To investigate the effect of earthquakes on the k_{eff} of the HTR-PM, four different packings were compared. The steady-state result for the homogeneous uniPor packing from the previous section was used for the packing during normal operation. For the packing after an earthquake, the shaken packing, the porosity was lowered to 0.3696, corresponding to a decrease of the bulk porosity from 0.37 to 0.3634 and a decrease of the porosities near the boundaries by a similar amount. The top of the pebble bed was lowered from 11 m to 10.8852 m to conserve the number of pebbles in the reactor. For a conservative limit on the packing fraction after an earthquake, for the third packing boundary effects were ignored, and the porosity was set to 0.3634. The fourth packing, the loose packing, represents a conservative limit on the packing before an earthquake, with an average porosity of 0.39 and a pebble bed height of 11.2498 m. The temperature and pebble burnup distributions of the beds were taken from the uniPor case and scaled to the new pebble bed heights of the packings.

For the three new pebble bed packings the k_{eff} was calculated and compared with the k_{eff} of the uniPor steady state case. The average porosity, effective core height, and difference in k_{eff} compared to the uniPor packing are given in Table 5.1. Comparing the uniPor packing with the shaken packing gives a realistic estimation of the increase in k_{eff} due to an earthquake of only 94 pcm. Even our most conservative estimate, starting with an unrealistically loose packing of 0.39 before the earthquake and ignoring the lower packing fraction near boundaries after the earthquake results in an increase in k_{eff} of 427 pcm. Such reactivity increases can easily be countered by thermal feedback or control rod movement, especially given that these increases are not instant but occur over the

time of the earthquake.

5.4 DLOFC and PLOFC transient analysis

Two transients were investigated, the depressurised and the pressurised loss of forced cooling transients (DLOFC and PLOFC). Both transients use as the initial state the steady state power and temperature distributions. At $t = 0$ the helium mass flow is set to zero. For the DLOFC the pressure inside the core is set to 1 bar, for the PLOFC the pressure is kept at 70 bars. The inflow and outflow locations are closed, so that no helium can flow in or out, and the pressure is allowed to increase during the transients. The top and bottom boundaries use adiabatic boundary conditions. 60 seconds into the transient the reactor is scrammed inserting $\Delta\rho_{scram} = -0.05$ reactivity into the core.

During the steady state calculations, the outer boundary of the carbon brick was fixed to 250 °C. However, during the transients it is important to realistically model the heat loss in the radial direction, and the core model described in Section 5.2 was extended. In the HTR-PM design, there is a 15 cm helium gap between the carbon brick and the surrounding core barrel, which is located between $r = 2.65$ m and $r = 2.69$ m. Between $r = 2.85$ m and $r = 2.981$ m, separated from the core barrel by a 16 cm helium gap, is the reactor pressure vessel (RPV). Outside the RPV is an air-filled cavity and across it at $r = 4.21$ m is the reactor cavity cooling system (RCCS) consisting of a water-cooled panel. The RCCS is a passive system designed to take away the decay heat from the core to the atmosphere during a loss of cooling transient. The helium gaps, core barrel, and RPV were added to the 3D geometric model. Heat transfer from the RPV to the water-cooled panel was included in pebFoam as a boundary condition. This boundary condition calculates the thermal flux from the RPV to the water-cooled panel, including both radiative heat transfer and the heat transfer due to natural convection in the air-filled cavity. It uses a fixed temperature of 70 °C for the water-cooled panel and emissivities of 0.9 for the RPV and water-cooled panel.

For simplicity, a point-kinetics model was added to pebFoam instead of doing a fully coupled calculation with PHANTOM. Boer et al. (2010) showed the difference between using a point-kinetics model and using 2D diffusion to evaluate the prompt fission power during the HTR-10 DLOFC transient can be significant, with the point-kinetics model overestimating the prompt fission power during shutdown by up to 10% of the initial power. However, the goal of the calculations is to compare different porosity distributions, not to calculate the transients for the HTR-PM in as much detail as possible. As in our calculations the reactor is scrammed after 60 seconds and the prompt power drops quickly, it is less important for the resulting temperatures to evaluate the neutronics with such detail, not justifying the significant increase in computational time and complexity of a fully coupled calculation.

The point-kinetics equations with six precursor groups solved in pebFoam are (Duder-

stadt and Hamilton, 1976)

$$\frac{dP_p}{dt} = \frac{\rho(t) - \beta}{\Lambda} P_p(t) + \sum_{i=1}^6 \lambda_i C_i(t) \quad (5.1)$$

$$\frac{dC_i}{dt} = \frac{\beta_i}{\Lambda} P_p(t) - \lambda_i C_i(t) \quad \text{with } i = 1 \dots 6 \quad (5.2)$$

with P_p the prompt fission power and C_i the precursor concentration of group i . The precursor coefficients λ_i and β_i for ^{235}U from Duderstadt and Hamilton (1976) are used. The neutron life $\Lambda = 0.0011$ s is taken from Zheng et al. (2009). The reactivity change $\rho(t)$ is caused by temperature feedback $\Delta\rho_T(t)$ from the pebbles and the reflector, changes in the ^{135}Xe concentration $\Delta\rho_{Xe}(t)$, and reactivity insertion $\Delta\rho_{scram}(t)$.

Temperature feedback coefficients for the fuel pebbles and the reflector were calculated with PHANTOM. The k_{eff} and temperature distribution at steady state were known from the previous calculations. New temperature dependent cross sections were generated and a new k_{eff} was calculated for 100 K higher pebble bed temperatures, keeping the temperatures of the reflector constant. The pebble temperature feedback coefficient was calculated with $\alpha_{peb} = \Delta k_{eff} / \Delta T = -6.75$ pcm/K. To determine the reflector feedback coefficient, the k_{eff} was calculated for the case where all temperatures, both in the pebble bed and in the reflector, were increased by 100 K, as during a LOFC transient a reflector temperature increase always follows a core temperature increase. The reflector temperature feedback coefficient was calculated using $\alpha_{ref} = \Delta k_{eff} / \Delta T - \alpha_{peb} = 2.12$ pcm/K.

The ^{135}Xe concentration during the transient is calculated using the equations and parameters from Duderstadt and Hamilton (1976) for the coupled ^{135}I and ^{135}Xe concentrations. The reactivity effect due to the change in ^{135}Xe concentration, ΔN_{Xe} , was approximated using

$$\Delta\rho_{Xe} = -\frac{\sigma_{a,Xe,av} \Delta N_{Xe}}{\Sigma_{a,av}} \frac{1}{1 + L^2 B_g^2} \quad (5.3)$$

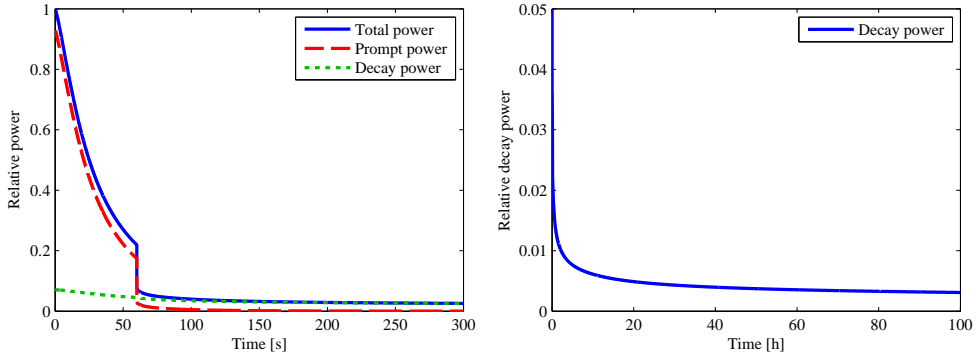
with $\sigma_{a,Xe,av}$ the effective one-group ^{135}Xe microscopic absorption cross section for the core and $\Sigma_{a,av}$ the effective one-group total macroscopic cross section inside the core. These were calculated by integration over energy E and spatial position \mathbf{x}

$$\Sigma_{a,av} = \frac{\int \int \varphi(E, \mathbf{x}) \Sigma(E, \mathbf{x}) dE d\mathbf{x}}{\int \int \varphi(E, \mathbf{x}) dE d\mathbf{x}} \quad (5.4)$$

resulting in values for $\sigma_{a,Xe,av} = 7.50 \times 10^5$ b and $\Sigma_{a,av} = 1.24 \times 10^{-3} \text{ cm}^{-1}$. The term $1/(1 + L^2 B_g^2)$ is the non-leakage probability, and is equal to k_{eff}/k_{∞} . A value of 0.89 was found by calculating the k_{∞} of the pebble bed with PHANTOM.

To calculate the total reactor power P_t , the decay heat P_d is added to the prompt power P_p . The decay heat is calculated with the following equation (ANS Standards Committee,

5. Effects of non-uniform porosity distributions in coupled steady state and transient analysis



(a) Relative power production during the first 300 seconds of the DLOFC. At $t = 0$ the coolant flow is stopped and at $t = 60$ s the reactor is scrammed.

(b) Relative time-dependent decay heat.

Figure 5.9: Development of the relative power production over time during the DLOFC transient, as a fraction of the total power of 250 MW at steady state.

1993), again using parameters for ^{235}U fuel.

$$P_t(t) = P_p(t) + \sum_{j=1}^{23} P_{d_j}(t) \quad (5.5)$$

$$\frac{dP_{d_j}}{dt} = -\lambda_j P_{d_j}(t) + \gamma_j P_p(t) \quad \text{with } j = 1 \dots 23 \quad (5.6)$$

The initial values of P_{d_j} were determined by assuming an irradiation time of 500 days, half the average residence time of a pebble in the core before reaching discharge burnup. To obtain the power density distribution at time t the power density distribution from the steady state calculations is scaled with the total power $P_t(t)$ from Equation 5.5.

5.4.1 DLOFC transient results

The relative total power (Equation 5.5), prompt power (Equation 5.1), and decay heat (Equation 5.6) for the first 300 seconds of the DLOFC transient are shown in Figure 5.9a. Figure 5.9b shows the relative decay power for the first 100 hours of the transient as a fraction of the total power during steady state. At the start of the transient, the total and prompt power immediately start to drop due to the negative fuel temperature feedback. At 60 seconds the reactor is scrammed and the prompt power almost immediately drops to zero, leaving only the decay power to heat up the core.

Figure 5.10 shows the solid temperature distribution on a 2D plane for the uniPor distribution at $t = 21$ h, when the maximum temperature is reached. As can be seen by

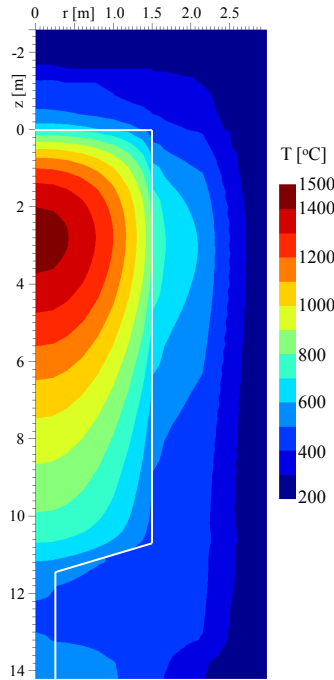


Figure 5.10: Solid temperature distribution during the DLOFC transient at $t = 21$ h, when maximum fuel temperature is reached, for a uniform porosity distribution (uniPor). The location of the pebble bed is outlined in white.

comparison with Figure 5.6, during the DLOFC transient the location of the maximum fuel temperature shifts from the bottom of the core towards a position more at the top of the pebble bed. The new maximum fuel temperature is located at $z = 2.7$ m from the top of the core, at the location of maximum power density. Figure 5.11a shows the maximum and average fuel temperature over time during the DLOFC transient for the three different porosity distributions. The first few hours of the transient the fuel temperature increases rapidly, until the peak maximum fuel temperature of 1439°C for the uniPor distribution is reached at $t = 21$ hours. As the decay power decreases, and the heat flux to the outside increases due to higher temperatures the maximum fuel temperature drops to 1351°C at $t = 100$ h.

These values are in range with those reported in literature. Using THERMIX, Zheng et al. (2009) found a maximum temperature of 1492°C after 26 hours, dropping to 1350°C at $t = 100$ h. Zheng et al. (2012) report maximum fuel temperatures of 1444 , 1466 and 1531°C occurring at $t = 27$ h, dropping to values between 1330 and 1380°C at $t = 100$ h, using respectively ATTICA3D, THERMIX without, and THERMIX with the effect of the fast

5. Effects of non-uniform porosity distributions in coupled steady state and transient analysis

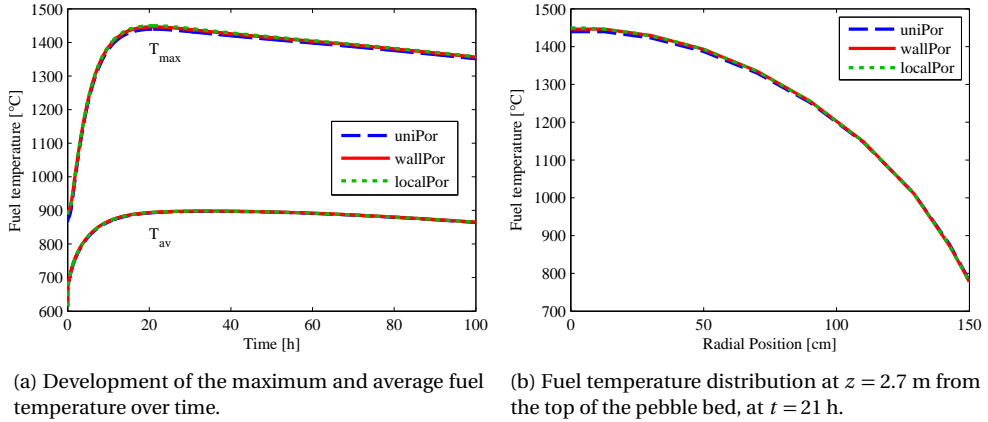


Figure 5.11: Fuel temperature profiles during the DLOFC transient for the three different porosity distributions: uniform porosity distribution (uniPor); lower porosity near the wall (wallPor); low porosity cluster at $z = 2.7$ m and $r = 0$ (localPor).

neutron irradiation dose on the pebble graphite thermal conductivity. The relatively small differences are easy to accept, especially considering the uncertainties and differences in the solid material properties, the irradiation dose of the graphite, the porosity, the power density distribution, and the geometric model.

The differences between the temperature profiles in Figure 5.11a are very small for the three different porosity distributions. Figure 5.11b shows the radial temperature distribution 21 hours into the DLOFC transient at $z = 2.7$ m, the location of the maximum fuel temperature. The shape of the radial fuel temperature profile is almost identical for the three different distributions. Only at the centre of the bed there is a small difference between the uniPor and wallPor distribution due to the higher power in the bulk of the bed for the wallPor distribution. Here the wallPor distribution reaches a maximum temperature of 1446 °C, only 7 °C higher than for the uniPor distribution. As for the steady state results, the temperature profile for the localPor distribution is almost identical to that of the wallPor distribution. Only inside the densely packed cluster at the centre of the bed, where the power density is higher, the fuel temperature is 3.5°C higher compared to the wallPor distribution. The size of the cluster is too small to cause a significant increase in temperature.

5.4.2 PLOFC transient results

In the PLOFC transient, as in the DLOFC transient, after the coolant flow stops at $t = 0$, the fission power quickly drops due to the negative temperature feedback and the core heats up mainly due to the decay power. Figure 5.12 shows the development of the maximum

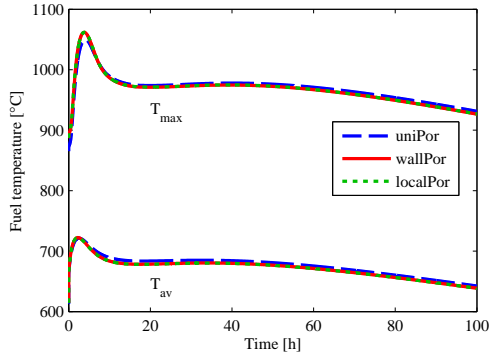


Figure 5.12: Development of the maximum and average fuel temperature over time during the PLOFC transient for the three different porosity distributions: uniform porosity distribution (uniPor); lower porosity near the wall (wallPor); low porosity cluster at $z = 2.7$ and $r = 0$ (localPor)

and average fuel temperature during the PLOFC transient for the three different porosity distributions. During the transient the temperature quickly rises to a sharp peak value at $t = 4$ h. Figures 5.13a and 5.13b show the 2D solid temperature distribution and the 2D helium flow field in the HTR-PM core for the uniPor distribution 4 hours into the transient.

The decay power is highest where the power density was high, in the centre and towards the top of the core. The pebble bed loses heat in radial direction to the reflector. Due to the temperature difference between the hot centre and the cooler wall of the pebble bed, the helium starts to circulate, see Figure 5.13b. The helium heats up while it flows up through the centre of the core. The hot helium flows into the void space above the bed, and through the porous top reflector in the cold helium plenum, causing the relatively high temperatures in these areas in Figure 5.13a. In these regions, flow resistance is lower than through the bed and a relatively strong circulation of the flow is seen in Figure 5.13b. The hot helium then flows down along the reflector wall, slowly cooling down until it reaches the hot helium plenum at the bottom of the core. In the PLOFC the core stays pressurised, and the helium density is high enough that the heat transfer due to natural circulation is significant, increasing the heat transfer from the centre of the bed to the graphite reflector. As a result, the maximum pebble temperature is much lower than in the DLOFC, and is reached much earlier in the transient. Also, as hot helium flows up through the centre of the core, heat is transferred up, shifting the location of the maximum fuel temperature towards the top of the pebble bed, at $z = 0.72$ m below the top of the bed, see Figure 5.13a.

Compared to the results reported by Zheng et al. (2009), the shape of the temperature distribution during the PLOFC is similar. However, Zheng et al. report a higher peak

5. Effects of non-uniform porosity distributions in coupled steady state and transient analysis

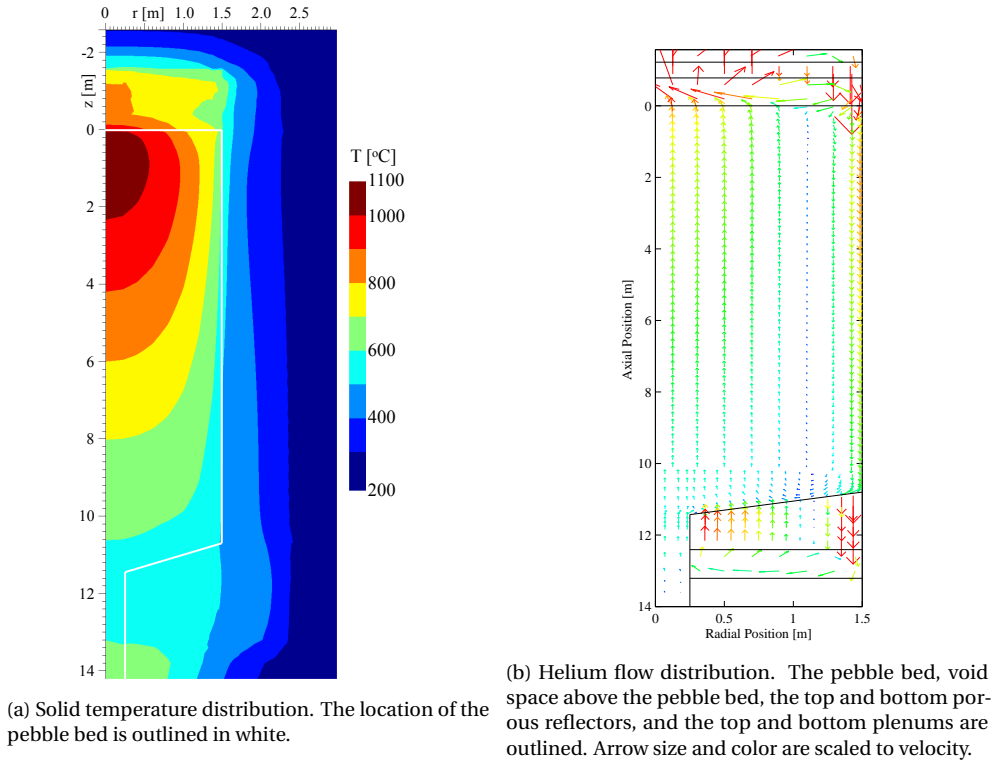


Figure 5.13: Solid temperature and helium flow distribution during the PLOFC transient at $t = 4$ h, when the peak maximum fuel temperature is reached, for a uniform porosity distribution (uniPor).

fuel temperature of $1134\text{ }^{\circ}\text{C}$ at $t = 7.6$ h compared to our value of $1049\text{ }^{\circ}\text{C}$ at $t = 4.0$ h for the uniPor distribution. This difference can be explained as Zheng et al. assumed a constant pressure of 70 bar throughout the transient, where we isolated the core and let the pressure increase to a maximum value of 90 bar, resulting in a higher helium density and stronger natural circulation.

As natural circulation plays an important role in the PLOFC transient, and as Section 4.3 showed the wall-channelling effect significantly increased heat transfer by natural circulation in the SANA experiments, we expected the wallPor distribution to have a lower maximum fuel temperature than the uniPor distribution. However, the wallPor distribution resulted in a peak maximum fuel temperature of $1062\text{ }^{\circ}\text{C}$, $13\text{ }^{\circ}\text{C}$ higher than for the uniPor distribution. Later in the transient the maximum and average fuel temperatures are indeed slightly lower for the wallPor distribution. As also the peak maximum fuel temperature is reached 11 minutes earlier than for the uniPor distribution, this seems

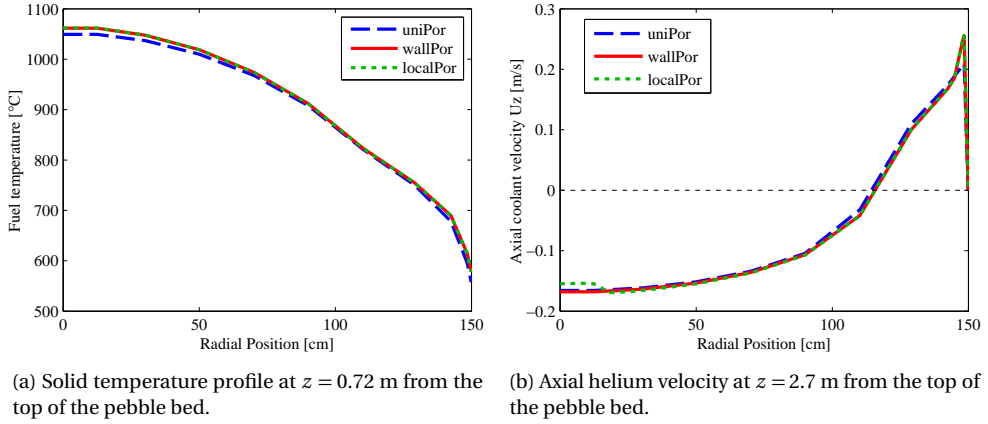


Figure 5.14: Temperature and axial helium velocity profiles 4 hours into the DPLOFC transient for the three different porosity distributions: uniform porosity distribution (uniPor); lower porosity near the wall (wallPor); low porosity cluster at $z = 2.7$ m and $r = 0$ (localPor).

to indicate a slight increase in the heat transfer by natural circulation for the wallPor distribution, although the temperature difference of only 4.5 °C at $t = 100$ h shows that this difference is very small.

The main reason for the higher peak fuel temperature for the wallPor case is the higher initial fuel temperatures in the central part of the bed at $t = 0$. As heat is transported by natural circulation up from the bottom through the centre of the bed, this temperature difference most strongly affects the top of the bed, where the peak fuel temperature occurs. Although not visible in Figure 5.12, the difference between the maximum temperatures for the wallPor and the uniPor distributions indeed steadily decrease over time. For $t > 7$ h, the maximum temperature for the wallPor distribution is lower than for the uniPor distribution.

Figure 5.14a shows the radial fuel temperature profiles at $z = 0.72$ m and $t = 4$ h. Besides the higher central fuel temperature, the fuel temperature close to the wall is also higher for the wallPor case than for the uniPor case. The reason is the larger helium velocity next to the wall due to the wall-channelling effect, which can be seen in Figure 5.14b, in which the axial velocity for the three porosity distributions is shown at $z = 2.7$ m and $t = 4$ h as a function of the radial position. As the helium temperature is highest in the void space above the pebble bed, and the helium velocity next to the wall is larger for the wallPor distribution, the helium has less time to cool down, resulting in higher temperatures next to the wall than for the uniPor distribution.

5. Effects of non-uniform porosity distributions in coupled steady state and transient analysis

Although the wallPor distribution does result in a larger positive helium velocity next to the wall, the velocities in the rest of the bed are almost identical to the uniPor case, indicating hardly any change in the total mass flow. The pebble bed in the SANA experimental facility also had an inner wall, facilitating wall-channelling not only for the downward flow, but also for the upward flow along the hot wall. In the HTR-PM, although flow resistance is smaller along the cold reflector wall, the helium still has to rise through the centre of the pebble bed where flow resistance is large.

The localPor distribution with the higher packing density at the centre of the bed results in a slightly smaller axial coolant velocity at the location of the densely packed cluster. As the cluster is too small to significantly disturb the flow, temperatures are almost identical to those of the wallPor distribution, resulting in a peak maximum fuel temperature only 0.25 °C higher than for the wallPor distribution.

5.5 Discussion and Conclusions

The effects of non-uniformities in the porosity distribution in pebble bed reactors on the power density, coolant velocity and temperature distribution during steady state and transients were investigated. Three different porosity distributions in the pebble bed were compared. The first was a uniform distribution called uniPor. The second distribution, wallPor, took into account that near the boundaries of a pebble bed the porosity is higher, and had higher porosities in the regions near the walls and top and a lower porosity in the bulk. The final distribution, localPor, was used to investigate the effect of variations in porosity in the bulk of the bed, and had a cylindrically shaped densely packed cluster of 30 cm high and 30 cm diameter with a porosity of 0.325 at the location of maximum power density. To compare the three porosity distributions, coupled steady state and depressurised and pressurised loss of forced cooling (DLOFC and PLOFC) transient calculations were performed with the pebFoam-PHANTOM coupled calculation scheme for a 3D quarter core model of the HTR-PM.

As in pebble beds the porosity in the bulk is lower than near the walls, the average porosity of larger pebble beds will be lower than for smaller beds. For the HTR-PM geometry we found an average uniform porosity of 0.376, significantly lower than the 0.39 used in literature.

The densification of the pebble bed during an earthquake was found to cause only a small increase in reactivity. Using realistic packing densities before and after an earthquake, a change in k_{eff} of only 96 pcm was found for the HTR-PM, far too small to cause any safety problems. As the packing is already quite dense during normal operation and will not drop below 0.3634 due to shaking of the bed, the change in porosity of a pebble bed during an earthquake is limited.

The differences in the porosity distributions hardly affected the neutron flux distribution as the neutron migration length in pebble bed reactors is relatively large. The

differences in power density between the three porosity distributions were almost directly proportional to the differences in packing fraction.

The densely packed cluster in the localPor distribution only affected the velocity and power density inside the cluster. The resulting temperature differences were small and local due to the small size of the cluster, having no effect on the maximum fuel temperature during steady state, and resulting in a 3.5 °C higher temperature in the DLOFC transient and a 0.25 °C higher temperature in the PLOFC transient. As the number of pebbles in a cluster scales with the cube of its diameter, the occurrence of a large enough cluster of densely packed pebbles to significantly affect the temperature is extremely unlikely.

In cylindrical pebble beds, taking into account the higher porosity near the wall and the lower porosity in the bulk of the pebble bed results in slightly higher temperatures in the centre of the bed during normal operation and, to a lesser degree, during DLOFC and PLOFC transients. This is caused by the higher power density in the bulk of the bed due to the increased packing density, and the lower mass flow in the bulk due to the strong increase in the mass flow along the wall. For the HTR-PM we found during normal operation an increase in the maximum fuel temperature of 21.5 °C for the wallPor distribution compared to the uniPor distribution. During the DLOFC transient we found an increase in the peak maximum fuel temperature of 7 °C and during the PLOFC transient an increase of 13 °C. In the DLOFC transient this was expected as natural convection is unimportant. During the PLOFC transient, natural convection was hardly increased due to the wall-channelling effect in the wallPor distribution, as flow still had to circulate up through the densely packed centre of the bed, where flow resistance is large.

For smaller cylindrical pebble beds with a higher wall area to volume ratio, when taking into account the non-uniform porosity distribution the temperature increase in the centre of the bed might be more pronounced. The AVR and HTR-10 designs have twice the wall area to volume ratio as the HTR-PM, which could result in a relatively high portion of the coolant flow being diverted along the wall due to wall-channelling, resulting in significantly higher temperatures in the centre of the core than would be predicted when assuming a uniform porosity. On the contrary, for annular pebble beds such as the PBMR, we expect that taking into account the lower porosity near the walls will result in a lower maximum fuel temperature. As in annular pebble beds the maximum fuel temperature occurs along the wall of the inner reflector, here the lower porosity near the walls will result in a lower power density and higher coolant flow. Additionally, during a PLOFC transient, the smaller flow resistance at both the inner and outer walls in annular pebble beds might significantly increase heat transfer by natural convection, resulting in lower peak maximum fuel temperatures.

CONCLUSIONS AND RECOMMENDATIONS

Pebble bed type high temperature reactors offer air-pollution-free and greenhouse-gas-free energy and are passively safe, with the added benefits of high outlet temperatures and online refuelling. In a pebble bed reactor the spherical fuel pebbles form a randomly stacked bed. A better understanding of the properties of this stacking and of the details of neutron transport and heat and mass transfer throughout the pebble bed is essential to accurately predict the temperature distribution inside the reactor core of pebble bed reactors.

The objective of this thesis is to investigate the stochastic properties of the pebble bed core and to investigate the effects of the non-homogeneity of the pebble bed on the neutronics and thermal-hydraulics.

6.1 Conclusions

Analysis of the stacking properties of pebble beds using both computer generated beds and experimental results show that the packing density of randomly stacked pebble beds is not uniform. Near boundaries, the stacking properties differ from those in the bulk of the bed. It was discovered that the stacking properties near solid walls closely resemble those of a hexagonal close packing, as the pebbles form ordered layers parallel to the wall. Further away from the wall, the ordering between the layers is lost. This results in strong fluctuations in the radial packing fraction close to the wall, gradually disappearing away from the wall. Right next to the wall, the porosity is significantly higher than in the rest of the bed, rising to unity at the wall. As a result, the average packing density of randomly stacked beds depends on their surface to volume ratio, with larger beds with lower surface to volume ratio having a lower average void fraction for the entire bed than smaller beds. It

was also shown that strong variations in packing density occur on a local scale throughout the bulk of randomly packed beds involving volumes containing up to a hundred pebbles. On a larger scale, these fluctuations gradually disappear, and averaged over large volumes of several thousands of pebbles and more variations in packing fractions were shown to be almost nonexistent.

Neutron transport calculations demonstrated that the fluctuations in packing density inside the bed do not have a significant effect on the flux distribution or k_{eff} of pebble bed reactors due to the large migration length of neutrons inside pebble bed reactors, much larger than the size of the fluctuations. However, ignoring the lower density in a pebble bed right next to the wall and especially at the top of a pebble bed can result in a small but significant overestimation of the neutron leakage for small pebble beds, leading to an underestimation of k_{eff} . The reverse is true when ignoring the streaming of neutrons through the void space in between the pebbles, causing a significant underestimation of leakage for small pebble bed reactors. We expect the effect of neutron streaming on k_{eff} to be large enough to be noticeable even for larger pebble bed reactors, but small enough to be ignored in most cases. Variations in the Dancoff factor near the boundaries of the pebble bed can safely be ignored.

We developed a thermal-hydraulics model for pebble beds presented in this thesis based on turbulence modelling for porous media, and demonstrated its capabilities to accurately predict flow and heat transfer in pebble beds both under natural convection conditions and during normal reactor operation. As the model equations become identical to the clear-flow turbulent equations when the porosity goes to unity, it is straightforward to apply the model to cases where a cavity is present on top of the pebble bed. Comparison of measurements and calculations for two SANA experiments confirmed that for the SANA geometry the lower packing density near the wall has a significant effect on heat transfer under natural circulation due to wall-channelling of the flow.

Coupled calculations were used to investigate the effects of non-uniformities in packing density for the HTR-PM for both steady-state and pressurised and depressurised loss of forced cooling transients. The occurrence of densely packed clusters inside the pebble bed was proven to have a negligible effect on the temperature distribution, during normal operation and during transients. Although small clusters with a diameter of up to 5 pebble diameters show large variations in packing density, their size is too small to significantly affect the temperature. As the cluster size is increased, the variation in packing fraction rapidly decreases.

In Chapter 5 we show that earthquakes do not pose a specific safety risk for pebble bed reactors. The core is already rather densely packed with a bulk porosity of 0.37, considering the minimum porosity of 0.3634 a randomly packed bed can reach due to shaking. As a result the maximum change in porosity and thereby the reactivity increase during an earthquake is very limited. For the HTR-PM we found a reactivity increase of 94 pcm, which can easily be countered by thermal feedback or control rod movement.

Taking into account the higher porosity next to the wall instead of assuming a uniform porosity distribution for the whole pebble bed resulted in a strong increase of the mass flow next to the wall during normal operation. As this causes a decrease of the mass flow through the bulk of the pebble bed, this wall-channelling effect results in lower temperatures at the wall and higher temperatures in the centre of the bed. For a large pebble bed with a low surface to volume ratio such as the HTR-PM, the effect on temperature is limited, resulting in an increase of the maximum fuel temperature of 21.5 °C. However, for smaller pebble beds or pebble bed reactors with a relatively large surface to volume ratio such as the AVR, wall-channelling might result in a twice as large or more increase of the maximum fuel temperature at the centre of the bed.

Although comparison of measurements and calculations for two SANA experiments confirmed that the lower packing density next the wall has a significant effect on heat transfer under natural circulation due to the wall-channelling effect and should be taken into account, for the HTR-PM the effect of the lower density next to the wall was shown to be negligible during both depressurised and pressurised LOFC transients. During the DLOFC transient this is no surprise, as for this transient heat transfer by natural convection is unimportant. However, during the PLOFC transient the heat transfer by natural convection was almost identical to the case with uniform porosity, as the flow still had to circulate up through the centre of the pebble bed where the flow resistance is large. From this we conclude that the lower porosity next to the wall hardly affects heat transfer by natural convection in cylindrical pebble beds such as the HTR-PM, but can cause a significant increase of 25% or more of the heat transfer by natural convection in annular pebble beds such as the SANA experimental facility and possibly the PBMR.

The final conclusion of this thesis is that although the pebble bed packing structure and porosity is very different near the wall than in the bulk of the bed, significantly affecting coolant flow in this region, for a large cylindrical pebble bed such as the HTR-PM the effect on neutronics and maximum fuel temperature is limited. Taking into account the non-uniform porosity distribution results in a slightly higher maximum fuel temperature during steady state, causing an even smaller increase during DLOFC and PLOFC transients. However, these conclusions cannot be extended to small pebble beds for which the effects on the temperature distribution might be far more pronounced, or annular pebble beds for which they might be reversed. The occurrence of densely packed clusters of pebbles throughout the pebble bed can safely be ignored, as these clusters are too small to significantly affect temperatures and cause hotspots.

6.2 Recommendations

In this thesis we used both experimental and computational results to show that the packing structure of a randomly packed bed is different near the wall than in the bulk of the bed. However, we were not able to properly validate the packing structure next to the wall of the computer generated bed. More detailed experimental results are needed to show

beyond doubt that our computational method generates beds with a realistic packing structure at the wall. We recommend generating a detailed 3D image of a randomly packed pebble bed, using a large number of pebbles with a well defined diameter, to generate a sufficient amount of statistical data with a small enough uncertainty.

The porosity in the bulk of a randomly packed bed was shown to be significantly lower than near the walls, resulting in lower average porosities for large diameter pebble beds than often used in literature. The bulk porosity was compared indirectly against the reported effective pebble bed height of the HTR-10 and PROTEUS facility, and directly by comparison with measurements on static cylindrical beds. However, as the porosity of randomly packed beds depends on the filling method of bed, we recommend experimental confirmation of the average bulk porosity inside a pebble bed reactor. Measurements should be performed using a pebble bed with a cone-shaped bottom with a hole in which the pebbles are circulated several times to create a stacking in the same manner as in real pebble bed reactors.

Various relations in the thermal-hydraulics model presented in Chapter 4 are based on relations for an average bed and are only valid for a small range of porosity values, for example the relations for the pebble-to-fluid heat transfer and the porous flow resistance. These relations were not derived to describe the near-wall region, where the pebble packing structure is different from the bulk of the bed, with strong variations in porosity and a non-isotropic packing structure. As such it is difficult to predict the actual heat transfer from the coolant to the wall and the flow resistance in the region next to the wall. As it is very difficult to measure properties locally inside a pebble bed without disturbing the flow and heat transfer, it would be interesting to investigate thermal-hydraulics next to the wall with detailed CFD analysis using LES or DNS simulations on small clusters of pebbles. Results could be used to derive more detailed relations for heat transfer and flow resistance as a function of averaged variables such as porosity, average fluid velocity and macroscopic kinetic energy, possibly with non-isotropic values near the wall.

Taking into account the lower porosity near the wall instead of using a uniform porosity distribution resulted in a modest increase of the maximum core temperature of 21.5 °C during normal operation for the HTR-PM due to wall-channelling of the flow. However, in pebble beds with a larger surface to volume ratio, such as the AVR and HTR-10, this temperature increase might be much larger. As for these reactors the volume ratio of the high-porosity region near the wall compared to the bulk volume is twice that of the HTR-PM, wall-channelling will have a more pronounced effect on the mass flow through the centre of the bed. Additionally, for these pebble beds the error in the porosity for the bulk of the bed will be higher when using a uniform porosity, resulting in an overestimation of the porosity of 3.3% (0.39 versus 0.37). This not only results in a significant overestimation of the mass flow through the centre when using a uniform porosity distribution, but also in an underestimation of the power density in the centre. To quantify the effect on the maximum fuel temperature in the centre of these pebble beds, coupled calculations for the steady state normal operation should be performed comparing a uniform porosity

distribution with a realistic porosity distribution.

Although annular pebble bed designs such as the PBMR also have a large surface to volume ratio, we expect wall-channelling to cause a decrease instead of an increase in the maximum pebble temperature. The reason is that in annular pebble beds the maximum temperature occurs at the inner wall, where the mass flow will increase due to the wall-channelling effect. Another benefit of an annular pebble bed design is that during a PLOFC transient the hot coolant can flow up along the inner wall, taking advantage of the wall-channelling effect. As we observed for the SANA facility, this can significantly increase heat transfer by natural circulation, resulting in a lower maximum fuel temperature. Both steady state and transient coupled calculations should be performed to investigate the effects of the lower porosity near the wall on the maximum fuel temperature in annular pebble beds.

BIBLIOGRAPHY

- C. R. A. Abreu. *Simulacao Computacional de Sistemas Granulares: Aplicacao dos Metodos de Monte Carlo e de Elementos Distintos*. Ph.D. thesis, Universidade Federal do Rio de Janeiro, Rio de Janeiro, Brasil, 2004.
- ANS Standards Committee. Decay heat power in light water reactors. Technical Report ANSI/ANS-5.1-1994, American Nuclear Society, USA, 1993.
- B. V. Antohe and J. L. Lage. A general two-equation macroscopic turbulence model for incompressible flow in porous media. *International Journal of Heat and Mass Transfer*, **40**, 3013, 1997.
- W. van Antwerpen, P. G. Rousseau and C. G. du Toit. Accounting for porous structure in effective thermal conductivity calculations in a pebble bed reactor. In *ICAPP 2009*. Tokyo, Japan, 2009.
- W. van Antwerpen, P. G. Rousseau and C. G. du Toit. Multi-sphere unit cell model to calculate the effective thermal conductivity in packed pebble beds of mono-sized spheres. *Nuclear Engineering and Design*, **247**, 183, 2012.
- T. Aste. Variations around disordered close packing. *Journal of Physics: Condensed Matter*, **17**, S2361, 2005.
- G. J. Auwerda et al. Comparison of experiments and calculations of void fraction distributions in randomly stacked pebble beds. In *PHYSOR 2010 - Advances in Reactor Physics to Power the Nuclear Renaissance*. American Nuclear Society, Pittsburgh, Pennsylvania, USA, 2010a.
- G. J. Auwerda et al. Effects of random pebble distribution on the multiplication factor in HTR pebble bed reactors. *Annals of Nuclear Energy*, **37**, 1056, 2010b.

- G. J. Auwerda et al. Effect of non-uniform porosity distribution on thermalhydraulics in a pebble bed reactor. In *Proceedings of NURETH-14*. Toronto, Ontario, Canada, 2011.
- G. J. Auwerda et al. Packing microstructure and local density variations of experimental and computational pebble beds. In *PHYSOR 2012*. American Nuclear Society, Knoxville, Tennessee, USA, 2012.
- G. J. Auwerda et al. Macroscopic and microscopic packing properties of experimental and computational pebble beds. *Nuclear Technology*, **183**, 272, 2013.
- G. J. Auwerda et al. Turbulence modelling for porous media in pebble bed reactors applied to sana experiments and htr-pm. *Submitted to Nuclear Engineering and Design*, 2014.
- J. Bader et al. Validation and application of 3D-methods for the design and safety analysis of high temperature reactors. In *NURETH-14*. Toronto, Ontario, Canada, 2011.
- P. Baronner. Axiale void fractie van een willekeurig gestapeld pebble bed. Internship report, Delft University of Technology, Delft, 2012.
- D. J. Behrens. The effect of holes in a reacting material on the passage of neutrons. *Proceedings of the Physical Society A*, **62**, 607, 1949.
- E. E. Bende et al. Analytical calculation of the average dancoff factor for a fuel kernel in a pebble bed high-temperature reactor. *Nuclear Science and Engineering*, **133**, 147, 1999.
- R. F. Benenati and C. B. Brosilow. Void fraction distribution in beds of spheres. *AIChE Journal*, **8**, 359, 1962.
- B. Boer. *Optimized Core Design and Fuel Management of a Pebble-Bed Type Nuclear Reactor*. Ph.D. thesis, Delft University of Technology, 2008.
- B. Boer et al. In-core fuel management optimization of pebble-bed reactors. *Nuclear Engineering and Design*, **239**, 3105, 2009.
- B. Boer et al. Validation of the DALTON-THERMIX code system with transient analysis of the HTR-10 and application to the PBMR. *Nuclear Technology*, **170**, 306, 2010.
- G. Breitbach and H. Barthels. The radiant heat transfer in the HTR core after failure of the afterheat removal systems. *Nuclear Technology*, **49**, 392, 1980.
- R. Chawla, O. P. Joneja and M. Rosselet. Definition and analysis of an experimental benchmark on shutdown rod worths in LEU-HTR configurations. *Nuclear Technology*, **139**, 50, 2002.
- J. J. Cogliati and A. M. Ougouag. Pebbles: A computer code for modeling packing, flow and re-circulation of pebbles in a pebble bed reactor. In *Proceedings of HTR2006, 3rd International Topical Meeting on High Temperature Reactor Technology*. Johannesburg, South-Africa, 2006.

- V. J. J. van Dijk. Radial void fraction measurements of the pebble-bed inside a pebble-bed reactor. BSc. thesis, available through <http://www.rrr.tudelft.nl/pnr> > publications, Delft University of Technology, Delft, 2008.
- V. J. J. van Dijk. *An Efficient Immersed Boundary Method Based on Penalized Direct Forcing for Simulating Flows Through Arbitrary Porous Media*. Master's thesis, available through <http://www.rrr.tudelft.nl/pnr> > publications, Delft University of Technology, Delft, 2011.
- M. Ding et al. Evaluation of experiments in the AVR with the DALTON-THERMIX code system. *Nuclear Engineering and Design*, **239**, 3105, 2009.
- T. J. Downar et al. PARCS: Purdue advanced reactor core simulator. In *PHYSOR-2002*. Seoul, South Korea, 2002.
- D. A. Drew. Mathematical modeling of two-phase flow. *Annual Review of Fluid Mechanics*, **15**, 261, 1983.
- J. J. Duderstadt and L. J. Hamilton. *Nuclear Reactor Analysis*. John Wiley & Sons, Inc., 1976. ISBN 0-471-22363-8.
- J. L. Finney. A procedure for the construction of voronoi polyhedra. *Journal of Computational Physics*, **32**, 137, 1979.
- H. Freund et al. Numerical simulations of single phase reacting flows in randomly packed fixed-bed reactors and experimental validation. *Chemical Engineering Science*, **58**, 903, 2003.
- Y. X. Gan, M. Kamlah and J. Reimann. Computer simulation of packing structure in pebble beds. *Fusion Engineering and Design*, **85**, 1782, 2010.
- Generation IV International Forum. GIF R&D outlook for generation IV nuclear energy systems, 2009.
- H. Gerwin and W. Scherer. Treatment of the upper cavity in a pebble-bed high-temperature gas-cooled reactor by diffusion theory. *Nuclear Science and Engineering*, **97**, 9, 1987.
- H. Gerwin, W. Scherer and E. Teuchert. The TINTE modular code system for computational simulation of transient processes in the primary circuit of a pebble-bed high-temperature gas-cooled reactor. *Nuclear Science and Engineering*, **103**, 302, 1989.
- M. Giese, K. Rottschäfer and D. Vortmeyer. Measured and modelled superficial flow profiles in packed beds with liquid flow. *AIChE Journal*, **44**, 484, 1998.
- J. S. Goodling et al. Radial porosity distribution in cylindrical beds packed with spheres. *Powder Technology*, **35**, 23, 1983.

- H. D. Gougar et al. Automated design and optimization of pebble-bed reactor cores. *Nuclear Science and Engineering*, **165**, 245, 2010.
- J. Groen. Radial void fraction measurement of a random multisized pebble stacking. BSc. thesis, available through <http://www.rrr.tudelft.nl/pnr> > publications, Delft University of Technology, Delft, 2009.
- H. Haque, W. Feltes and G. Brinkmann. Thermal response of a modular high temperature reactor during passive cooldown under pressurized and depressurized conditions. *Nuclear Engineering and Design*, **236**, 475, 2006.
- M. L. Hunt and C. L. Tien. Effects of thermal dispersion on forced convection in fibrous media. *International Journal of Heat and Mass Transfer*, **31**, 301, 1988.
- IAEA. Heat transport and afterheat removal for gas cooled reactors under accident conditions. Technical Report IAEA-TECDOC-1163, IAEA, Vienna, Austria, 2000.
- L. P. B. M. Janssen and M. M. C. G. Warmoeskerken. *Transport Phenomena Data Companion*. ISBN 90-407-1302-2, Delft University Press, Delft, The Netherlands, third edition, 1987.
- X. Jing et al. Prediction calculations and experiments for the first criticality of the 10 mw high temperature gas-cooled reactor-test module. *Nuclear Engineering and Design*, **218**, 43, 2002.
- W. S. Jodrey and E. M. Torey. Computer simulation of isotropic, homogeneous, dense random packing of equal spheres. *Powder Technology*, **30**, 111, 1981.
- R. Julien, A. Pavlovitch and P. Meakin. Random packings of spheres build with sequential models. *Journal of Physics A: Mathematical and General*, **25**, 1992.
- J. L. Kloosterman and A. M. Ougouag. Comparison and extension of dancoff factors for pebble-bed reactors. *Nuclear Science and Engineering*, **157**, 16, 2007.
- O. Koberl and R. Seiler. Detailed analysis of pebble-bed htr proteus experiments with the monte carlo code tripoli4. In *2nd International Topical Meeting on High Temperature Reactor Technology*. Beijing, China, 2004.
- K. Krüger. *Experimentelle Simulation eines Kühlmitterverlust-Störfalls mit dem AVR-Reaktor*. Ph.D. thesis, FZ Jülich, Germany, 1989.
- KTA. Reactor core design for high-temperature gas-cooled reactors. KTA 3102, Geschäftsstelle des Kerntechnischen Ausschusses, Germany, 1983.
- K. Kugeler and R. Schulten. *Hochtemperatur-reaktortechnik*. ISBN: 3-540-51535-6. Springer-Verlag, Berlin, Germany, 1989.

- M. Lange. Experimente zur selbsttätigen Abfuhr der Nachwärme bei Hochtemperatur-Reaktoren. Jül-3102, Forschungszentrum Jülich GmbH, Jülich, Germany, 1995.
- D. Lathouwers. *Modelling and Simulation of Turbulent Bubbly Flow*. Ph.D. thesis, Delft University of Technology, 1999.
- D. Lathouwers and J. Bellan. Modeling of dense gas-solid reactive mixtures applied to biomass pyrolysis in a fluidized bed. *International Journal of Multiphase Flow*, **27**, 2155, 2001.
- B. E. Launder and D. B. Spalding. The numerical computation of turbulent flows. *Computer Methods in Applied Mechanics and Engineering*, **3**, 269, 1974.
- J. J. Lee et al. Numerical treatment of pebble contact in the flow and heat transfer analysis of a pebble bed reactor core. *Nuclear Engineering and Design*, **237**, 2183, 2007a.
- J. J. Lee et al. Turbulence-induced heat transfer in PBMR core using LES and RANS. *Nuclear Science and Technology*, **44**, 985, 2007b.
- S. Lei et al. A personal computer-based simulation-and-control-integrated platform for 10-MW high temperature gas-cooled reactor. *Nuclear Technology*, **145**, 189, 2004.
- M. J. S. de Lemos. *Turbulence in Porous Media*. Elsevier, 2006.
- M. J. S. de Lemos and E. J. Braga. Modeling of turbulent natural convection in porous media. *International Communications in Heat and Mass Transfer*, **30**, 615, 2003.
- Y. Li and W. Ji. A collective dynamics-based method for initial pebble packing in pebble flow simulations. *Nuclear Engineering and Design*, **250**, 229, 2012.
- J. Lieberoth and A. Stojadinović. Neutron streaming in pebble beds. *Nuclear Science and Engineering*, **76**, 336, 1980.
- T. Masuoka and Y. Takatsu. Turbulence model for flow through porous media. *International Journal of Heat and Mass Transfer*, **39**, 2803, 1996.
- D. Mathews and T. Williams. LEU-HTR PROTEUS system component description. PSI technical memorandum TM-41-93-43, Paul Scherrer Institut, 1995.
- R. Moormann. A safety re-evaluation of the AVR pebble bed reactor operation and its consequences for future HTR concepts. In *HTR-2008*, 265–274. Washington DC, USA, 2008.
- P. Mraško. Homogeneous and isotropic hard sphere model of amorphous metals. *Journal de Physique Colloques*, **41**, 322, 1980.
- G. E. Mueller. Radial void fraction distributions in randomly packed fixed beds of uniformly sized spheres in cylindrical containers. *Powder Technology*, **72**, 269, 1992.

- A. Nakayama and F. Kuwahara. A general macroscopic turbulence model for flows in packed beds, channels, pipes, and rod bundles. *Journal of Fluids Engineering*, **130**, 2008.
- H. Oehme and J. Schoening. Design features and engineering status of the THTR 300 MWe prototype power station. In *Proceedings of the gas-cooled reactor information meeting at the Oak Ridge National Laboratory*. Oak Ridge, Tennessee USA, 1970.
- OpenFOAM Foundation. *OpenFOAM, the open source CFD toolbox*, 2.1.1 edition, 2012.
- J. Oppe, J. B. M. de Haas and J. C. Kuijper. PANTHERMIX (PANTHER-THERMIX) user manual. Technical Report Report ECN-I98-019, ECN, Peten, 1998.
- A. M. Ougouag and J. J. Cogliati. Earthquakes and pebble bed reactors: time-dependent densification. In *M&C + SNA 2007*. Monterey, California, USA, 2007.
- D. Pavlidis and D. Lathouwers. Fluid flow and heat transfer investigation of pebble bed reactors using mesh-adaptive large-eddy simulation. In *NURETH-14*. Toronto, Ontario, Canada, 2011.
- D. Pavlidis and D. Lathouwers. Fluid flow and heat transfer investigation of pebble bed reactors using mesh-adaptive LES. *Nuclear Engineering and Design*, **264**, 161, 2013.
- M. H. J. Pedras and M. J. S. de Lemos. Macroscopic turbulence modeling for incompressible flow through undeformable porous media. *International Journal on Heat and Mass Transfer*, **44**, 1081, 2001.
- M. R. Raupach and R. H. Shaw. Averaging procedures for flow within vegetation canopies. *Boundary Layer Meteorology*, **22**, 79, 1982.
- J. Reimann, R. A. Pieritz and R. Rolli. Topology of compressed pebble beds. *Fusion Engineering and Design*, **81**, 653, 2006.
- J. Reimann et al. X-ray tomography investigations on pebble bed structures. *Fusion Engineering and Design*, **83**, 1326, 2008.
- F. Reitsma et al. The PBMR steady-state and coupled kinetics core thermal-hydraulics benchmark test problems. *Nuclear Engineering and Design*, **236**, 657, 2006.
- P. J. Roache. *Verification and Validation in Computational Science and Engineering*. Hermosa Publishers, Albuquerque, N.M., USA, 1998.
- S. J. P. Romkes et al. CFD modelling and experimental validation of particle-to-fluid mass and heat transfer in a packed bed at very low channel to particle diameter ratio. *Chemical Engineering Journal*, **96**, 3, 2003.
- G. van Rossum. Python tutorial. Technical Report CS-R9526, Centrum voor Wiskunde en Informatica (CWI), Amsterdam, 1995.

- P. G. Rousseau, C. G. du Toit and W. A. Landman. Validation of a transient thermal-fluid systems CFD model for a packed bed high temperature gas-cooled nuclear reactor. *Nuclear Engineering and Design*, **236**, 555, 2006.
- H. J. Rütten and K. A. Haas. V.S.O.P. (99/3) - input description. Internal document, Institut für Sicherheitsforschung und Reaktortechnik (ISR), Forschungszentrum Jülich, 2003.
- C. H. Rycroft et al. Analysis of granular flow in a pebble-bed nuclear reactor. *Physical Review E*, **74**, 2006.
- SCALE-5.1. SCALE: a modular code system for performing standardized computer analysis for licensing evaluation. Technical Report Vols. I-III, Version 5.1, CCC-732; ORNL/TM-2005/39, Oak Ridge National Laboratory, Tennessee, USA, 2006.
- SCALE-6. SCALE: a modular code system for performing standardized computer analysis for licensing evaluation. Technical Report Vols. I-III, Version 5.1, CCC-750; ORNL/TM-2005/39, Oak Ridge National Laboratory, 2009.
- W. W. Schertz and K. B. Bischoff. Thermal and material transport in non-isothermal packed beds. *AIChE Journal*, **15**, 597, 1969.
- E. U. Schlünder. Wärme- und Stoff übertragen zwischen durchströmten Schüttungen und darin eingebetteten Einzelkörpern. *Chemie Ingenieur Technik*, **38**, 967, 1966.
- G. D. Scott and D. M. Kilgour. The density of random close packings of spheres. *Journal of Physics D: Applied Physics*, **2**, 863, 1969.
- A. Seubert et al. The 3-D time-dependent transport code TORT-TD and its coupling with the 3D thermal-hydraulic code ATTICA3D for HTGR applications. *Nuclear Engineering and Design*, **251**, 173, 2012.
- A. Shams et al. Calibration of a pebble bed configuration for direct numerical simulation. In *NURETH-14*. Toronto, Ontario, Canada, 2011.
- W. Soppe. Computer simulation of random packings of hard spheres. *Powder Technology*, **62**, 189, 1990.
- P. L. Spedding and R. M. Spencer. Simulation of packing density and liquid flow in fixed beds. *Computational Chemical Engineering*, **19**, 43, 1995.
- B. Stöcker. Untersuchungen zur selbsttätigen Nachwärmeabfuhr bei Hochtemperaturreaktoren unter besonderer Berücksichtigung der Naturkonvektion (Investigations for self-acting decay heat transport in high temperature reactors under special consideration of natural convection). Forschungszentrum Jülich GmbH, Jül-3504, Jülich, Germany, 1998.
- B. Stöcker and H.-F. Nießen. Data sets of the sana experiment 1994-1996. Forschungszentrum Jülich GmbH, Jül-3409, Jülich, Germany, 1997.

- S. Struth. Thermix-direkt: Ein Rechenprogramm zur instationären zweidimensionalen Simulation thermohydraulischer Transienten. Forschungszentrum Jülich GmbH, Germany, 1995.
- W. K. Terry and A. M. Ougouag. Effects of spatial variations in packing fraction on reactor physics parameters in pebble-bed reactors. In *Nuclear Mathematical and Computational Science: A Century in Review, A Century Anew*. American Nuclear Society, Gatlinburg, Tennessee, USA, 2003.
- F. E. Teruel and Rizwan-Uddin. A new turbulence model for porous media flows. part i: Constitutive equations and model closure. *International Journal of Heat and Mass Transfer*, **52**, 4264, 2009.
- The MathWorks Inc. *MATLAB*. Natick, MA, r2012a edition, 2012.
- C. G. du Toit. The numerical determination of the variation in the porosity of the pebble-bed core. In *Proceedings of the International Topological Meeting on High Temperature Reactor Technology (HTR-TN 2002)*. Petten, The Netherlands, 2002.
- C. G. du Toit. Radial variation in porosity in annular packed beds. *Nuclear Engineering and Design*, **238**, 3073, 2008.
- C. G. du Toit, W. van Antwerpen and P. G. Rousseau. Analysis of the porous structure of an annular pebble bed reactor. In *ICAPP 2009*. Tokyo, Japan, 2009.
- B. Tyobeka, K. Ivanov and A. Pautz. Utilization of two-dimensional deterministic transport methods for analysis of pebble-bed reactors. *Annals of Nuclear Energy*, **34**, 396, 2007.
- C. F. Voronoï. Nouvelles applications des parametres continus a la théorie de formes quadratiques. *Journal für die Reine und Angewandte Mathematik*, **134**, 198, 1908.
- N. Wakao and K. Kato. Effective thermal conductivity of packed beds. *Journal of Chemical Engineering of Japan*, **2**, 24, 1969.
- E. J. M. Wallerbos. *Reactivity effects in a pebble-bed type nuclear reactor*. Ph.D. thesis, Technical University Delft, 1998.
- E. J. M. Wallerbos, A. Hogenbirk and J. E. Hoogenboom. Calculations of reactivity effects of water ingress and neutron streamin in htr-proteus, a small low-enriched uranium fuelled pebble-bed system. In *ICENES '98*. Tel Aviv, Israel, 1998.
- T. Williams. LEU-HTR PROTEUS: configuration descriptions and critical balances for the cores of the HTR-PROTEUS experimental programme. PSI technical memorandum TM-41-95-18, Paul Scherrer Institut, 1995.
- T. Williams, M. Rosselet and W. Scherer. Critical experiments and reactor physics calculations for low-enriched high temperature gas cooled reactors. Technical Report IAEA-TECDOC-1249, IAEA, Vienna, Austria, 2001.

- F. Wols et al. Core design and fuel management studies of a thorium breeder pebble bed high temperature reactor. *Nuclear Technology*, **?**, 2014.
- World Nuclear Association. Electricity supplied by nuclear energy. Available at: <http://www.world-nuclear.org/Nuclear-Basics/Electricity-supplied-by-nuclear-energy/>, Accessed: 28 February, 2014.
- A. Wouterse and A. P. Philipse. Geometrical cluster ensemble analysis of random sphere packings. *Journal of Chemical Physics*, **125**, 2006.
- Z. Wu, D. Lin and D. Zhong. The design features of the HTR-10. *Nuclear Engineering and Design*, **218**, 25, 2002.
- P. Zehner and E. U. Schlünder. Einfluss der Wärmestrahlung und des Druckes auf den Wärmestromtransport in nicht durchströmten Schüttungen. *Chemie Ingenieur Technik*, **44**, 1303, 1972.
- Z. Zhang et al. Current status and technical description of chinese 2 x 250 MWth HTR-PM demonstration plant. *Nuclear Engineering and Design*, **239**, 1212, 2009.
- Y. Zheng and L. Shi. Characteristics of the 250MW pebble-bed modular high temperature gas-cooled reactor in depressurized loss of coolant accidents. In *Proceedings of the 4th International Topical Meeting on High Temperature Technology*. Washington, DC USA, 2008.
- Y. Zheng, L. Shi and Y. Dong. Thermohydraulic transient studies of the Chinese 200 MWe HTR-PM for loss of forced cooling accidents. *Annals of Nuclear Energy*, **36**, 742, 2009.
- Y. Zheng et al. Thermal hydraulic analysis of a pebble-bed modular high temperature gas-cooled reactor with ATTICA3D and THERMIX codes. *Nuclear Engineering and Design*, **246**, 286, 2012.
- Y. H. Zheng, L. Shi and Y. Wang. Water-ingress analysis for the 200 MWe pebble-bed modular high temperature gas-cooled reactor. *Nuclear Engineering and Design*, **240**, 3095, 2010.
- Y. P. Zhou et al. Thermal hydraulic simulation of reactor of HTR-PM based on thermal-fluid network and SIMPLE algorithm. *Progress in Nuclear Energy*, **62**, 83, 2012.

Summary

To more accurately predict the temperature distribution inside the reactor core of pebble bed type high temperature reactors, in this thesis we investigated the stochastic properties of randomly stacked beds and the effects of the non-homogeneity of these beds on the neutronics and thermal-hydraulics in the core of pebble bed reactors.

To investigate the stacking properties of randomly stacked beds, we measured the average packing fraction and the radial and axial packing fraction profiles of a bed containing 5400 pebbles. In a second experiment, three-dimensional X-ray tomography was used to determine the pebble locations of a bed containing 8900 pebbles. Results were used to validate a computational method to generate pebble bed stackings based on the removal of overlaps. Different stacking properties were found near the wall than in the bulk of the bed, indicating the stacking is anisotropic here, forming ordered layers parallel to the wall with hexagonal-like stacking properties. This results in strong fluctuations in the radial packing fraction close to the wall, and a significantly higher porosity next to the wall than in the rest of the bed, rising to unity at the wall. As a result, the average porosity of randomly stacked beds depends on their volume to surface ratio, with larger beds having a lower average void fraction than smaller bed. We also found strong variations in the local porosity throughout the pebble bed, resulting in small clusters of densely packed pebbles.

To investigate the effect of the non-homogeneity of pebble bed on neutron transport, we compared k_{eff} calculations for a model with uniform porosity, a zones model including density fluctuations, and an exact model with all pebbles modelled individually. Calculations were performed for an infinite cylinder and for a model of the PROTEUS facility. For the infinite cylinder we found a 71 pcm higher k_{eff} for the zones model than for the uniform porosity model, showing the effect of density fluctuations at the wall to be very small. However, the same comparison for PROTEUS showed an increase of 649 pcm due to the low packing fraction near the top of the pebble bed, resulting in a much lower average packing fraction in the uniform porosity model. The effect of neutron streaming through the void space in between the pebbles was calculated by comparing the zones model with the exact model, and was found to decrease k_{eff} by 606 pcm for the infinite cylinder, and by 1240 pcm for PROTEUS, showing neutron streaming is an important effect in small pebble bed reactors. Changing the Dancoff factor in the outer part of the pebble bed to compensate for the lower probability of neutrons to enter other fuel pebbles caused no significant changes in k_{eff} .

Next we derived a thermal-hydraulics model for pebble beds based on turbulence modelling for porous media. Calculation results agreed well with measurements from two SANA experiments and with calculation results from THERMIX for the HTR-PM, showing the model's capability to accurately predict the flow and temperature distribution for both natural circulation and during full power operation. Comparison of results for a uniform porosity distribution with results for a nonuniform distribution with lower porosities near

the walls showed the importance of the wall-channelling effect, resulting for the two SANA experiments in increased natural circulation and a better match with measurements.

Finally, we investigated the effects of non-uniformities in the porosity distribution for the HTR-PM during normal operation and DLOFC and PLOFC transients, using coupled thermal-hydraulic and neutron transport calculations. We found that earthquakes can cause only a small change in porosity in pebble bed reactors, limiting the reactivity increase due to an earthquake for the HTR-PM to 94 pcm, which is too small to pose a significant safety risk. The occurrence of a cluster of densely packed pebbles was shown to result in no significant increase in the maximum fuel temperature during normal operation, and only very small increases in the maximum fuel temperature of 3.5 °C in the DLOFC transient and 0.25 °C in the PLOFC transient. Comparison of calculations taking into account the higher porosity at the boundaries with a uniform porosity distribution showed a strong increase of the mass flow next to the wall during normal operation, resulting in a decrease of the mass flow through the bulk of the pebble bed. Combined with the slightly higher power density in the centre of the bed due to the lower porosity, this caused a modest increase of the maximum fuel temperature in the centre of the bed of 21.5 °C during steady state. The increased steady state temperature and power density at the centre of the bed also caused a small increase in the peak maximum fuel temperature of 7 °C for the DLOFC and of 13 °C for the PLOFC transient. During the PLOFC transient, natural convection was almost identical to the case with uniform porosity, as flow still had to circulate up through the densely packed centre of the bed, where flow resistance is large.

We conclude that taking into account the lower porosity near the boundary causes a strong increase in the mass flow next to the wall, but for large cylindrical pebble beds such as the HTR-PM will cause only a small increase of the maximum fuel temperature during steady state, and will hardly affect heat transfer during transients. However, as we expect the temperature increase to be much larger for smaller pebble beds, and as we expect the lower porosity near the inner wall to result in a decrease in the maximum fuel temperature for annular pebble beds, we recommend further research for these types of pebble bed reactors.

Samenvatting

Om nauwkeuriger de temperatuur in de kern van een hoge temperatuur kogelbedreactor te kunnen voorspellen, worden in dit proefschrift de stochastische eigenschappen van willekeurig gestapelde bedden en het effect van de inhomogeniteit van deze bedden op het neutronentransport en de thermo-hydraulische eigenschappen in de kern van een kogelbedreactor onderzocht.

Om de stapel eigenschappen van willekeurig gestapelde bedden te onderzoeken, hebben we de gemiddelde pakkingfractie en de radiale en axiale pakkingfractie-profielen gemeten van een bed met 5400 kogels. In een tweede experiment is met driedimensionale röntgen tomografie de locatie bepaald van alle 8900 kogels in een bed. Met de resultaten is een computerprogramma gevalideerd, wat stapelingen van kogelbedden kan genereren gebaseerd op het elimineren van overlappingen. Voor de stapeling dicht bij een wand vonden we andere eigenschappen dan voor de stapeling midden in een bed. Bij de wand is de stapeling anisotropisch en vormen de kogels geordende lagen parallel aan de wand met eigenschappen vergelijkbaar met een hexagonale dichtste stapeling. Dit resulteert in grote fluctuaties in de radiale pakkingfractie dicht bij de wand en een significant hogere porositeit vlak naast de wand dan in de rest van het bed, met een porositeit die naar 1 gaat direct aan de wand. Als gevolg hiervan is de gemiddelde porositeit van een willekeurig gestapeld bed afhankelijk van zijn oppervlakte-volume verhouding en hebben grotere bedden een lagere gemiddelde porositeit dan kleinere bedden. Ook vonden we grote variaties in de lokale porositeit binnen in een kogelbed, resulterend in kleine clusters met een zeer compacte stapeling.

Om het effect van de inhomogeniteit van het kogelbed op het neutronentransport te onderzoeken hebben we de k_{eff} berekend en vergeleken van een model met een uniforme porositeit, van een zone model waarin fluctuaties in dichtheid zijn meegenomen, en van een exact model waarin alle kogels individueel gemodelleerd zijn. Berekeningen zijn gedaan voor een oneindige cilinder en voor de geometrie van de PROTEUS faciliteit. Voor de oneindige cilinder resulteerde het zone model in een 71 pcm hogere k_{eff} dan het model met de uniforme porositeit, wat aantoont dat het effect van de fluctuaties in porositeit bij de wand zeer klein is. Echter, dezelfde vergelijking voor PROTEUS resulteerde in een 649 pcm hogere k_{eff} voor het zone model, omdat de hoge porositeit vlak bij de top van het bed resulteerde in een veel hogere gemiddelde porositeit in de rest van het bed voor het uniforme model. Door het zone model te vergelijken met het exacte model kon worden berekend dat het stromen van neutronen door de holtes tussen de kogels resulteerde in een 606 pcm lagere k_{eff} voor de oneindige cilinder en een 1240 pcm lagere k_{eff} voor PROTEUS, wat aantoont dat het stromen van neutronen door de holtes een belangrijk effect is in kleine kogelbedreactoren. Het aanpassen van de Dancoff factor in de buitenste rand van het kogelbed als compensatie voor de lagere kans dat neutronen hier een andere splijtstofkogel binnendringen veroorzaakte geen significante veranderingen in k_{eff} .

Vervolgens hebben we een thermo-hydraulica model voor kogelbedreactoren afgeleid,

gebaseerd op turbulentie modellering voor poreuze media. Berekeningen met het model kwamen goed overeen met meetresultaten van twee SANA experimenten en met berekeningen met THERMIX voor de HTR-PM, wat laat zien dat het model accuraat de stromings- en temperatuurverdeling kan bepalen tijdens zowel natuurlijk circulatie als vollast bedrijf. Vergelijking van resultaten voor een uniforme porositeitsverdeling met resultaten voor een niet-uniforme porositeitsverdeling met een lagere porositeit nabij de wand resulteerde voor de twee SANA experimenten in een toename in de natuurlijke circulatie en een betere overeenkomst met meetresultaten, wat het belang van de stroomkanalisering langs de wand aantoonst.

Tot slot hebben we de effecten van inhomogeniteiten in de porositeitsverdeling onderzocht voor de HTR-PM tijdens vollast bedrijf en bij DLOFC en PLOFC transiënten, gebruikmakend van gekoppelde thermo-hydraulica en neutronentransport berekeningen. Berekeningen wezen uit dat aardbevingen slechts een kleine veranderingen in de porositeit in kogelbedreactoren kunnen veroorzaken, waardoor de verhoging van de reactiviteit door een aardbeving voor de HTR-PM gelimiteerd is tot 94 pcm, te klein om een significant veiligheidsrisico te vormen. Het voorkomen van zeer compact gestapelde clusters van kogels resulteerde niet in een significant hogere maximale splijstoftemperatuur tijdens vollast bedrijf en resulteerde in slechts een hele kleine verhoging van de maximale brandstoftemperatuur tijdens DLOFC en PLOFC transiënten van respectievelijk 3.5 °C en 0.25 °C. Een vergelijking van berekeningen waarbij rekening was gehouden met de hogere porositeit bij de wanden met een uniform verdeelde porositeit liet een sterke toename van de massastroom langs de wand zien tijdens vollast bedrijf, wat resulteerde in een verlaging van de massastroom door de rest van het kogelbed. Gecombineerd met de iets hogere vermogensdichtheid in het midden van het bed vanwege de lagere porositeit aldaar, veroorzaakte dit een bescheiden verhoging van de maximale splijstoftemperatuur in het midden van het bed van 21.5 °C tijdens vollast bedrijf. De hogere temperatuur en vermogensdichtheid bij vollast bedrijf in het midden van het bed resulteerden ook in een kleine toename in de piek van de maximale splijstoftemperatuur van 7 °C tijdens de DLOFC en van 13 °C tijdens de PLOFC transient. Tijdens de PLOFC transient was de natuurlijke convectie vrijwel hetzelfde als voor de berekeningen met een uniforme porositeit, aangezien de circulatie van de stroom omhoog liep door het midden van het bed, waar de stromingsweerstand groot is door de lage porositeit.

Wij concluderen dat rekening houden met de lagere porositeit bij de wanden resulteert in een veel hogere massastroom langs de wand, maar dat dit voor grote cilindervormige kogelbedreactoren zoals de HTR-PM in slechts een kleine verhoging van de maximale splijstoftemperatuur resulteert tijdens vollast bedrijf, en nauwelijks effect heeft op het warmtetransport tijdens transiënten. Echter, voor kleine kogelbedden verwachten we een veel grotere toename van de maximale splijstoftemperatuur. Voor annulaire kogelbedden verwachten we juist dat de lagere porositeit bij de binnenste wand een verlaging van de maximale splijstoftemperatuur zal veroorzaken. Hierom bevelen we voor deze twee soorten reactoren verder onderzoek aan.

Acknowledgements

Although doing your PhD research is mostly solitary work, there are many people I would like to thank for their contributions in the past five and a half years.

First, I want to thank my promotor Tim van der Hagen, my copromotor Jan-Leen Kloosterman and Danny Lathouwers for their supervision. I would also like to thank Hugo van Dam for joining us during our monthly meetings.

There are many people who made my six months at INET, Tsinghua University memorable. I would like to thank prof. Li Fu and dr. Zheng Yanhua for their supervision. Specifically, I thank dr. Zheng Yanhua for allowing me to use her THERMIX calculation results of the HTR-PM. Hao Chen and Zheng Ming Ming, thank you for your friendship and making me feel at home in Beijing. My sincere gratitude to Hao Chen, his father, mother and brother, for inviting me to their home during the Chinese new year and showing me the real China. It is a memory I will always carry with me and changed the way I look at the world.

August, Vincent, Joost and Peter I want to thank for building and calibrating the PebBEx facility. Joost and Peter, thank you for your measurement data of the radial and axial packing fraction profiles. Vincent, thank you for your measurement data of the 3D scan of a pebble bed.

I want to thank everyone from PNR/NERA for the many times we shared cake at the coffee table, for the DDBDD's, for the many drinks on Friday evenings in 'het koepeltje' and for making me look forward to go to work every day, especially on Fridays. Thank you Martin, Eduard, Dick, Peter, Anja, Denis, Norbert, Ming, Dimitrios, József, Christophe, Zoltan, Karoly, Stuart (and Edith for the many cakes she baked and the pub quizzes you organised), Luca, Jurriaan, Wim, Valentina, Amer, Stavros, Brian, Johan, Jitka, and all the students. Ine, thank you for making me feel welcome from the very first day as a bachelor student, for always being ready to help, and for arranging many fun things that made our group come together, such as the international evenings and the beer tour through Delft. Frank, my fellow pebble bed PhD and roommate, thank you for our many discussions on work, sports, and religion, and for helping me with the burnup scripts. Bart, thank you for the many good conversations and beers we shared, in and out of the office, before and after our time at PNR/NERA. Zoltan, thank you for suffering me walking into your office when I was in need of a talk or a listening ear to vent my frustrations.

I also want to thank Henk, Koos and Robin for running the bar, and Jan-Willem en Leon for sitting in front of the bar, and making het koepeltje such a good place to drink a beer after work.

My bachelor, master, and internship students, Thomas, Tom, Gunther, Stephane, Frank, Luuk and Peter, thank you for letting me learn how to supervise, and teaching me the great satisfaction that comes from helping someone bring a project to a good end.

Acknowledgements

I also want to thank my colleagues at NIV for never stopping to ask me if I was already finished and when we would have a celebration.

Rami, I want to thank you for helping me finally choose physics, for making me a part of your many research projects when we were kids (too bad we never managed to make enough hydrogen to launch that rocket), and for sharing your passion for science with me.

Mijn familie, Siebe, Amber, Irmin, Wemy, oma, ik wil jullie bedanken voor jullie liefde, voor jullie interesse in mijn werk, en voor alle warmte.

Annemarie, je bent er wanneer ik je nodig heb en je blijft in mij geloven ook als ik dat niet meer doe. Voor jou wil ik zijn wat jij in mij ziet. Bij jou kom ik thuis, waar we ook zijn. Ik hou van je.

List of Publications

- G. J. Auwerda, J. L. Kloosterman, A. J. M. Winkelman, J. Groen, V. J. J. van Dijk. Comparison of experiments and calculations of void fraction distributions in randomly stacked pebble beds. In *PHYSOR 2010 - Advances in Reactor Physics to Power the Nuclear Renaissance*, Pittsburgh, Pennsylvania, USA, 2010.
- G. J. Auwerda, J. L. Kloosterman, D. Lathouwers, T. H. J. J. van der Hagen. Effects of random pebble distribution on the multiplication factor in HTR pebble bed reactors. *Annals of Nuclear Energy*, 37:1056-1066, 2010.
- G. J. Auwerda, J. L. Kloosterman, D. Lathouwers, T. H. J. J. van der Hagen. Effect of non-uniform porosity distribution on thermalhydraulics in a pebble bed reactor. In *Proceedings of NURETH-14*, Toronto, Ontario, Canada, 2011.
- G. J. Auwerda, J. L. Kloosterman, D. Lathouwers, T. H. J. J. van der Hagen. Packing micro-structure and local density variations of experimental and computational pebble beds. In *PHYSOR 2012*, Knoxville, Tennessee, USA, 2012.
- G. J. Auwerda, Y. H. Zheng, J. L. Kloosterman, D. Lathouwers. Comparison of 2D and 3D heat transfer models around the coolant channel in the HTR-PM side reflector. In *6th International Conference on High Temperature Reactor Technology (HTR 2012)*, Tokyo, Japan, 2012.
- G. J. Auwerda, J. L. Kloosterman, D. Lathouwers, T. H. J. J. van der Hagen. Macroscopic and microscopic packing properties of experimental and computational pebble beds. *Nuclear Technology*, 183:272-286, 2013.
- G. J. Auwerda, Y. H. Zheng, J. L. Kloosterman, D. Lathouwers. Comparison of 2D and 3D heat transfer models around the coolant channel in the HTR-PM side reflector. *Nuclear Engineering and Design*, 271:465-471, 2014.
- G. J. Auwerda, J. L. Kloosterman, D. Lathouwers, T. H. J. J. van der Hagen. Turbulence modelling for porous media in pebble bed reactors applied to SANA experiments and HTR-PM. Submitted to *Nuclear Engineering and Design*.

Curriculum Vitae

Personal Details

Name: Gert Jan Auwerda
Date of Birth: 22-09-1981
Place of Birth: Delft
E-mail: gjauwerda@yahoo.com
Nationality: Dutch

Employment and Education

2013–present	Senior policy advisor at the directorate Nuclear Installations and Safety of the Dutch Ministry of Economic Affairs
2009–2013	PhD researcher at Delft University of Technology Thesis title: Core Physics of Pebble Bed High Temperature Nuclear Reactors.
2010–2011	6 months internship at INET, Tsinghua University, Beijing, China Research on heat transfer in pebble bed reactors.
2007–2009	Master degree in Applied Physics at Delft University of Technology Thesis title: Investigation of Neutronics and Heat Transfer in a Gas Core Reactor. Graduated cum laude.
2009	3 months internship at NRG, Petten Investigating MCNP weight window generation using adjoint deterministic calculations.
2001–2007	Bachelor degree in Applied Physics at Delf University of Technology Thesis title: Computational Modeling of a Molten Salt Reactor.
1999–2001	Propedeuse in Computational Sciences at Delf University of Technology
1993–1999	Gymnasium Haganum , Den Haag High school, graduated with a grade average of 8.5.

Skills

Languages	Dutch (native speaker), English (fluent), German (average)
Computer skills:	Programming experience in FORTRAN, C++, Python
Additional training	<ul style="list-style-type: none">– PRINCE2 Foundation– Frédéric Joliot / Otto Hahn summer school on small and modular nuclear reactors, Aix-en-Provence (award for best student)– Nuclear reactor graphite course, University of Manchester– Radiological Health Physics level 3– Scientific writing in English

Other Activities

2001-2010	Various committees at korfbal club Fortuna First member, then bursar, then chairman of the event committee, organising around 15 events per year, ranging from children's events for up to 200 children and dance events for up to 250 people. Member of the internet committee, maintaining the website of the club.
–	Hobby's Korfbal (player, referee, trainer/coach), running (ran the 2009 Amsterdam marathon), reading, D&D (pen-and-paper roleplaying game)